La mer 63 : 57–94, 2025, https://doi.org/10.32211/lamer.63.3-4_57
Société franco-japonaise d'Océanographie, Tokyo

ASUKA: Observing the Kuroshio south of Japan for estimating volume transport

Shiro IMAWAKI[1)]*

Abstract: The Affiliated Surveys of the Kuroshio off Cape Ashizuri (ASUKA) Group conducted intensive observation of the Kuroshio off Shikoku over a two-year period (1993–1995), by current-meter moorings and frequently repeated hydrographic surveys, with the primary objective of estimating volume transport. This review paper describes the observational program and summarizes the major findings obtained from the ASUKA dataset and its combination with satellite altimetry data. A very strong vertical velocity shear was observed in the upper Kuroshio during the nearshore path, whereas a very weak shear was observed in the upper coastal countercurrent during the offshore path. Geostrophic balance was confirmed to hold well in intermediate and deep layers, as indicated by excellent agreement in vertical difference between geostrophic and measured velocities. From eight full-depth geostrophic velocity sections referred to velocities measured at mid-depths, the average volume transport of the Kuroshio was estimated at 60 Sv (1 Sv = 10^6 m^3 s^{-1}) and that of the throughflow Kuroshio, excluding the contribution of a local offshore anticyclonic eddy, was estimated at 44 Sv. A strong linear relationship was found between net transport integrated from the coast and sea-surface dynamic topography difference from the coast. Using this relationship, satellite altimetry data enabled us to derive proxy time series of transport for the past three decades, yielding means of 61 Sv for the Kuroshio and 35 Sv for the throughflow Kuroshio. The mean transport of the throughflow Kuroshio during large meander periods was nearly identical to that during non-large meander periods. Beneath the Kuroshio, a pair of stable deep westward and eastward flows, intensifying toward the bottom, was observed over the Nankai Trough.

Keywords : ASUKA, Kuroshio, moored current-meter, satellite altimetry, volume transport

1. Introduction

The moderate climate of the Earth is maintained through meridional heat transport by both the oceans and the atmosphere (e.g., BRYDEN and HALL, 1980; TALLEY, 1984; MACDONALD and WUNSCH, 1996). In the North Atlantic, the deep meridional overturning circulation plays a fundamental role in net heat transport (e.g., MACDONALD and BARINGER, 2013). Conversely, in the North Pacific, net meridional heat transport is primarily caused by upper-layer circulation, making the wind-driven horizontal circulation important (e.g., BRYDEN et al., 1991; MACDONALD

1) Professor Emeritus of Kyushu University, Yokohama, 224–0014, Japan
* Corresponding author:
E-mail: imawaki@g04.itscom.net

and BARINGER, 2013). Accordingly, the western-boundary current of the wind-driven subtropical gyre of the North Pacific, i.e., the Kuroshio, plays a vital role by transporting warm water northward, thereby compensating for the southward transport of cooler water in the ocean interior.

Until the early 1990s, velocity of the Kuroshio had not been measured accurately due to technical difficulties of velocity measurements within a strong current. Most information about velocity and volume transport relied on geostrophic calculations based on the assumption of no motion at a chosen deep reference level. The resulting volume transport is referred to as geostrophic transport (GT). When geostrophic velocity and transport are referred to measured or inferred velocities at the reference level, they are termed absolute geostrophic velocity (AGV) and absolute geostrophic transport (AGT), respectively.

The following are pioneering studies on current measurements of the Kuroshio near Japan. WORTHINGTON and KAWAI (1972) conducted direct current measurements in the deep layer in 1965 by tracking neutrally-buoyant floats and estimated AGTs of the Kuroshio for the first time. They reported AGTs of 84 Sv (1 Sv = 10^6 m^3 s^{-1}) south of Shikoku and 88 Sv southeast of Cape Inubo. TAFT (1978) deployed current-meters (CMs) near the bottom for the first time in 1971 and estimated AGTs of 70 Sv east of Kyushu, 57 Sv south of Shikoku, and 77 Sv south of Honshu. TAKEMATSU et al. (1986) used moored CMs to measure surface-layer velocities of the Kuroshio south of Kyushu from 1979 to 1983. Their results showed that the Kuroshio was confined to the upper 600 m layer, on average, at this location, suggesting that a reference level of no motion in geostrophic calculations should be selected with caution. KANEKO et al. (1992) measured velocity across the Kuroshio south of Shikoku and Honshu down to 400 m depth using an acoustic Doppler current profiler (ADCP) towed from a ship (towed-ADCP). Their observation revealed a subsurface velocity core of the Kuroshio and a subsurface countercurrent.

Volume transport of the Kuroshio has been estimated from hydrographic surveys conducted south of Japan (e.g., SUGIMOTO et al., 2010; NAGANO et al., 2013; LONG et al., 2018) and in the Tokara Strait (e.g., GUO et al., 2012; WEI et al., 2013; LIU et al., 2019). For hydrographic sections that form a closed volume, velocities at reference levels can be inferred using the inverse method developed by WUNSCH (1978), which has been applied to the Kuroshio region to estimate AGTs (e.g., NAKANO et al., 1994; KANEKO et al., 2001; ZHU et al., 2006; NAGANO et al., 2010; GUO et al., 2013). A detailed review of Kuroshio-related studies was given by ANDO et al. (2021).

The large international program, the World Ocean Circulation Experiment (WOCE), began an eight-year observational campaign in 1990. Its primary objective was to observe the three-dimensional structure of the global ocean to provide a basis for improving ocean models, and by extension, to improve the reliability of climate models (GRASSL, 2001). The Kuroshio south of Japan was identified as an important observational target, and its associated current measurement array was designated PCM5 (SIEDLER et al., 2001). The array was intended to be combined with a trans-Pacific hydrographic survey along 30° N (WOCE Hydrographic Program P2) to estimate the net meridional heat transport at mid-latitudes in the North Pacific.

The altimetry satellite TOPEX/Poseidon began measuring sea-surface height in September 1992, with the objective of improving understanding of global ocean circulation (FU et al., 1994). Satellite remote-sensing was a key contributor to the success of WOCE (SIEDLER et al., 2001). Altimetric measurements have since been

continued along the same subsatellite track by its successor Jason-1 and others (e.g., ESCUDIER et al., 2017).

The PCM5 observation by means of CM moorings and frequently repeated hydrographic surveys were conducted from 1993 to 1995 by the Affiliated Surveys of the Kuroshio off Cape Ashizuri (ASUKA) Group, being hereafter referred to as the ASUKA intensive observation (Fig. 1). The primary objective of this observation was to estimate the AGT of the Kuroshio as accurately as possible (IMAWAKI et al., 1997). Its observation line was aligned with subsatellite track number 112 of TOPEX/Poseidon, which passes over Cape Ashizuri (see Fig. 1 in UCHIDA and IMAWAKI, 2008), thereby facilitating the integration of *in situ* and altimetry data. As a result, the ASUKA intensive observation was the largest-scale measurement program of the Kuroshio south of Japan. Also the ASUKA program was considered to be the most comprehensive effort of western-boundary current observation during the WOCE period, providing a multiyear transport record through a combination of *in situ* current measurements, geostrophy, and satellite altimetry (CLARKE et al., 2001). During the intensive observation period, the Kuroshio took the non-large meander path as classified by KAWABE (1995), as indicated by IMAWAKI et al. (2023), which is hereafter abbreviated as IM23.

As shown in the inset of Fig. 1, the Kuroshio enters the Shikoku Basin from the East China Sea through the Tokara Strait and merges with the Ryukyu Current to the east of the Strait. In the Shikoku Basin, the Kuroshio usually flows along the southern coast of Japan, accompanied by the local anticyclonic stationary eddy on its offshore side (HASUNUMA and YOSHIDA, 1978), which is known as the Warm Eddy off Shikoku. The transport of the eastward-flowing, nearshore-side half of the Warm Eddy is necessarily included in transport of the Kuroshio as the whole eastward flow, which is hereafter referred to as the Kuroshio. The westward-flowing, offshore-side half is referred to as the Kuroshio recirculation and must be accounted for when estimating the net transport of the Kuroshio as throughflow, which is hereafter referred to as the throughflow Kuroshio. The throughflow transport is defined as the transport of the Kuroshio minus the transport of the Kuroshio recirculation.

Major findings from the ASUKA program have been published in various journals. This review provides a comprehensive summary of those results as well as a detailed description of the ASUKA field observation. The structure of rest of the paper is as follows. Section 2 describes the ASUKA intensive observation and satellite altimetry data used. Section 3 presents the primary outputs of the intensive observation, including descriptions of the flow field and estimates of volume transport. Section 4 shows observations and studies following the intensive phase. Section 5 introduces the time series of volume transport derived from the combined ASUKA and altimetry data. Sections 6 and 7 present the discussion and summary, respectively.

2. Intensive observation and altimetry data

Figure 1 shows the ASUKA observation line, consisting of hydrographic stations and mooring stations in the Kuroshio and Kuroshio recirculation regions off Shikoku, Japan. The line is oriented approximately perpendicular to the typical path of the Kuroshio off Cape Ashizuri, where the current path is most stable within the Shikoku Basin (TAFT, 1972). In the Kuroshio region (north of 30° N), the spacing of coordinated common hydrographic stations was either 20 or 31 km, while mooring stations were spaced at intervals ranging from 20 to 92 km. On the continen-

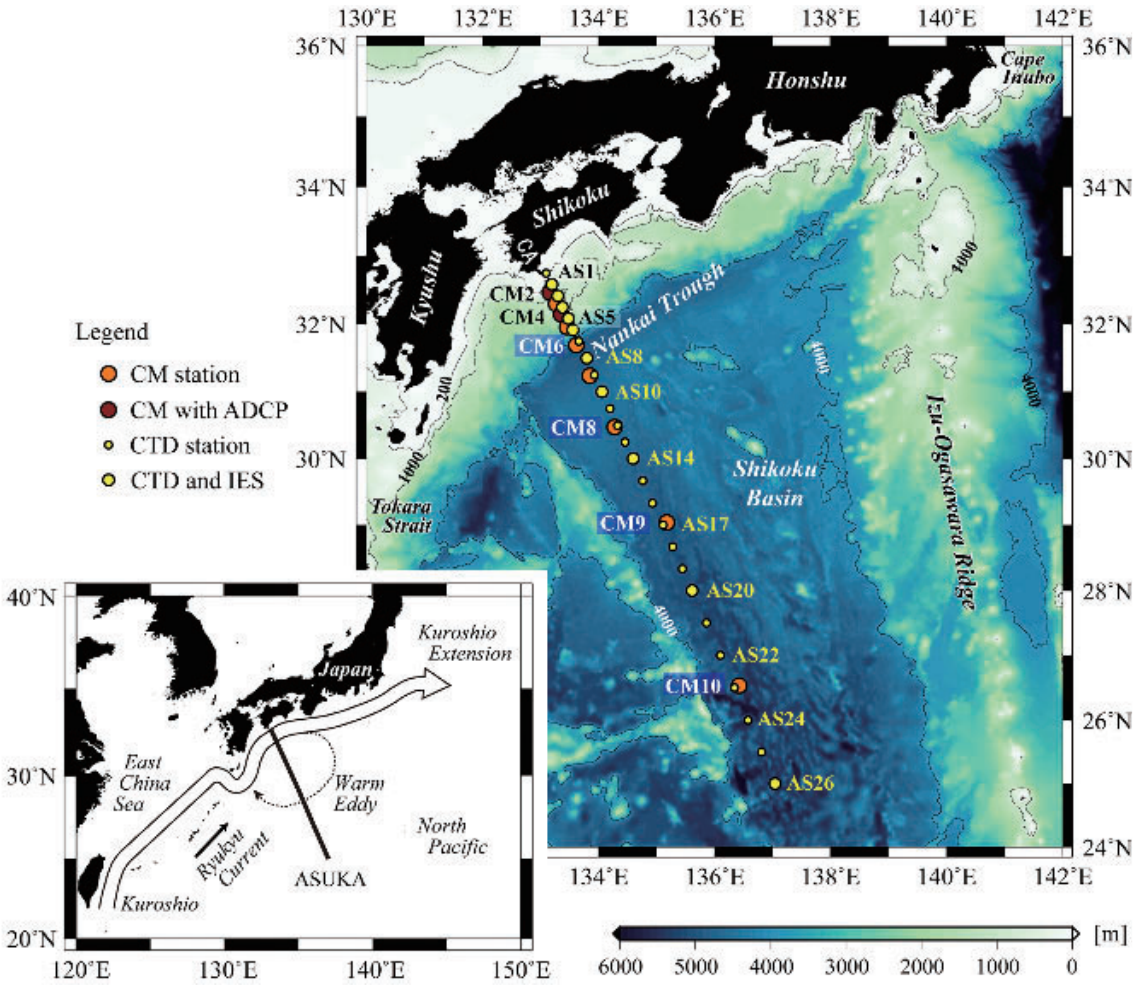

Fig. 1 The ASUKA (Affiliated Surveys of the Kuroshio off Cape Ashizuri) observation line (155° True), crossing the Kuroshio off Shikoku, Japan. Coordinated common hydrographic stations (AS1–AS26; yellow dots and circles) and mooring stations (CM2–CM10; orange and maroon circles) are shown on a map of bottom topography based on AMANTE and EAKINS (2009). Two maroon circles (CM2 and CM4) show mooring stations equipped with an upward-looking ADCP (acoustic Doppler current profiler). Ten yellow circles show IES (inverted echo sounder) stations. The location of Cape Ashizuri is shown by CA in Shikoku. The small-scale inset shows the ASUKA line relative to the schematic flow pattern of the Kuroshio and the Warm Eddy off Shikoku. Adapted from IMAWAKI et al. (2023)

tal slope, mooring stations were positioned halfway between hydrographic stations. To prevent entanglement between conductivity-temperature-depth recorder (CTD) cables and mooring lines, mooring stations were offset by about 7 km upstream of hydrographic stations. To include the Kuroshio recirculation in transport estimates, the observation line was extended southward to 25° N.

Figure 2 shows the vertical distribution of moored instruments. Aanderaa CMs (primarily model RCM-5) were deployed at nominal depths

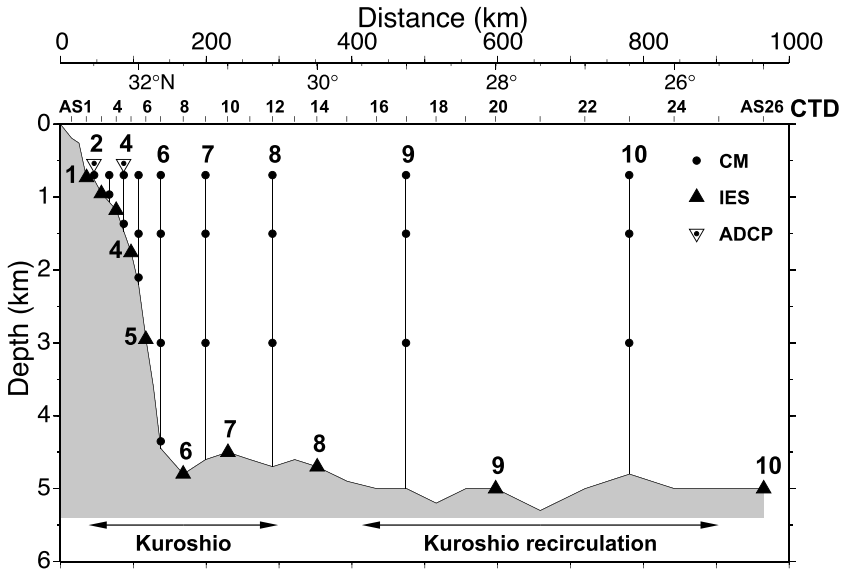

Fig. 2 Locations and nominal depths of deployed instruments, including CMs (current-meters), upward-looking ADCPs and IESs. Tick marks at the top denote locations of coordinated common hydrographic stations (CTD; AS1–AS26). The shaded area represents ocean bottom. From IMAWAKI et al. (1997).

of 700, 1500, and 3000 m, and near the bottom. The CMs measured temperature as well as current speed and direction. Two CMs were deployed at the 700 m level, as this depth was considered the most important for providing velocities at the reference level. CMs were also deployed on the continental slope to detect near-bottom flows. Upward-looking ADCPs (moored-ADCPs) were installed at the tops of mooring lines at Stations CM2 and CM4 to capture the strong current of the upper-layer Kuroshio, which could not be measured by standard moored CMs. Inverted echo sounders (IESs) were deployed on the bottom such that each CM station was positioned halfway between adjacent IES stations, to infer upper-layer fields of temperature and AGV continuously, thereby supplementing the sporadic hydrographic surveys.

The ASUKA intensive observation was initiated in October 1993 with the deployment of nine moorings equipped with 33 CMs (UMATANI et al., 2001; KASHIMA et al., 2003) and two moored-ADCPs (TAKEUCHI et al., 2002), and ten IESs (BOOK et al., 2002a; 2002b). Mooring lines were deployed by the buoy-first, anchor-last method. In September 1994, the nine moorings were recovered and redeployed with the same configurations. The final recovery of all moorings and IESs was conducted in November 1995, marking the end of the intensive observation. All of the instruments were successfully recovered, with the exception of four CMs from the second-year deployment at Station CM8 and the IES at Station IES5.

Actual instrument depths differed from their designed ones, mostly because moorings were deployed at depths different from planned ones unavoidably, especially at stations on the continental slope, and partly because mooring lines were titled in the strong current. To monitor in-

strument depths, pressure was measured by CMs at the nominal depth of 700 m. For example, their mean depths at Stations CM2 through CM7 were estimated at 530–690 m.

During the intensive observation period, the ASUKA Group conducted hydrographic surveys along the observation line using CTDs, expendable CTDs, and expendable bathy-thermographs (XBTs) as frequently as possible (UCHIDA et al., 2008). In total, 42 hydrographic sections were obtained for the upper 1000 m in the Kuroshio region. Eight of them were full-depth CTD sections (IM23). In addition, velocity measurements using a towed-ADCP were carried out 12 times along the ASUKA line (ZHU et al., 2001).

This ASUKA intensive observation was conducted by a collaborative group of a large number of scientists from Japan and the United States of America (IMAWAKI et al., 2001; BOOK et al., 2002a). This large-scale observation was not organized under a single project but was made possible through the coordinated efforts of many scientists from universities, research institutes, and agencies. The scale and success of the observation likely reflect the common deep interest of many Japanese physical oceanographers in the Kuroshio.

Altimetric sea-level anomalies along the TOPEX/Poseidon subsatellite track were used to derive proxy time series of Kuroshio volume transport (IMAWAKI et al., 2001; UCHIDA, 2025). Gridded sea-surface dynamic topography (SSDT) data derived from satellite altimetry were used to examine horizontal flow patterns of the Kuroshio and its recirculation (IM23; IMAWAKI et al., 2025). These altimetry data were produced by the SSALTO Multimission Ground Segment/Data Unification and Altimeter Combination System (AVISO, 2016), and provided by the Archiving, Validation, and Interpretation of Satellite Oceanographic Data (France) and the Copernicus Marine Service Information (European Union). Additionally, sea-level data from the tide gauge at Cape Ashizuri (see Fig. 1 for location), maintained by the Japan Meteorological Agency, were used as a reference for the altimetric sea-level profile along the ASUKA line (IMAWAKI et al., 2001; UCHIDA, 2025).

3. Results from intensive observation

Representative examples of vertical sections of potential temperature, salinity, and AGV in the Kuroshio and Kuroshio recirculation regions are shown in Fig. 3. The velocity component perpendicular to the ASUKA line, oriented toward 65° True, is hereafter referred to simply as velocity. Mean vertical sections of potential temperature and salinity, based on 154 sections collected from 1992 to 2008, were provided by UCHIDA et al. (2008). These sections reveal following features. The 10° C isotherm, which indicates the center of the main thermocline, deepens from approximately 300 m near the coast to 650 m offshore (at 30–31° N). The main body of the Kuroshio is located near the coast, as indicated by the pronounced inclination of the main thermocline and AGV values exceeding 10 cm s^{-1}. The core of the North Pacific Intermediate Water, which is characterized by a vertical salinity minimum, deepens from approximately 500 m near the coast to 800 m offshore (at 31° N). The core of the North Pacific Subtropical Mode Water, which is characterized by a vertical salinity maximum, is located at around 150 m on the offshore side of the Kuroshio. The instantaneous AGV section (Fig. 3 (c)) shows complex eastward and westward flows associated with active mesoscale eddies in the Kuroshio recirculation region.

The validity of geostrophic balance in the Kuroshio and Kuroshio recirculation regions was examined using repeated hydrography data and moored CM data at nominal depths of 700, 1500,

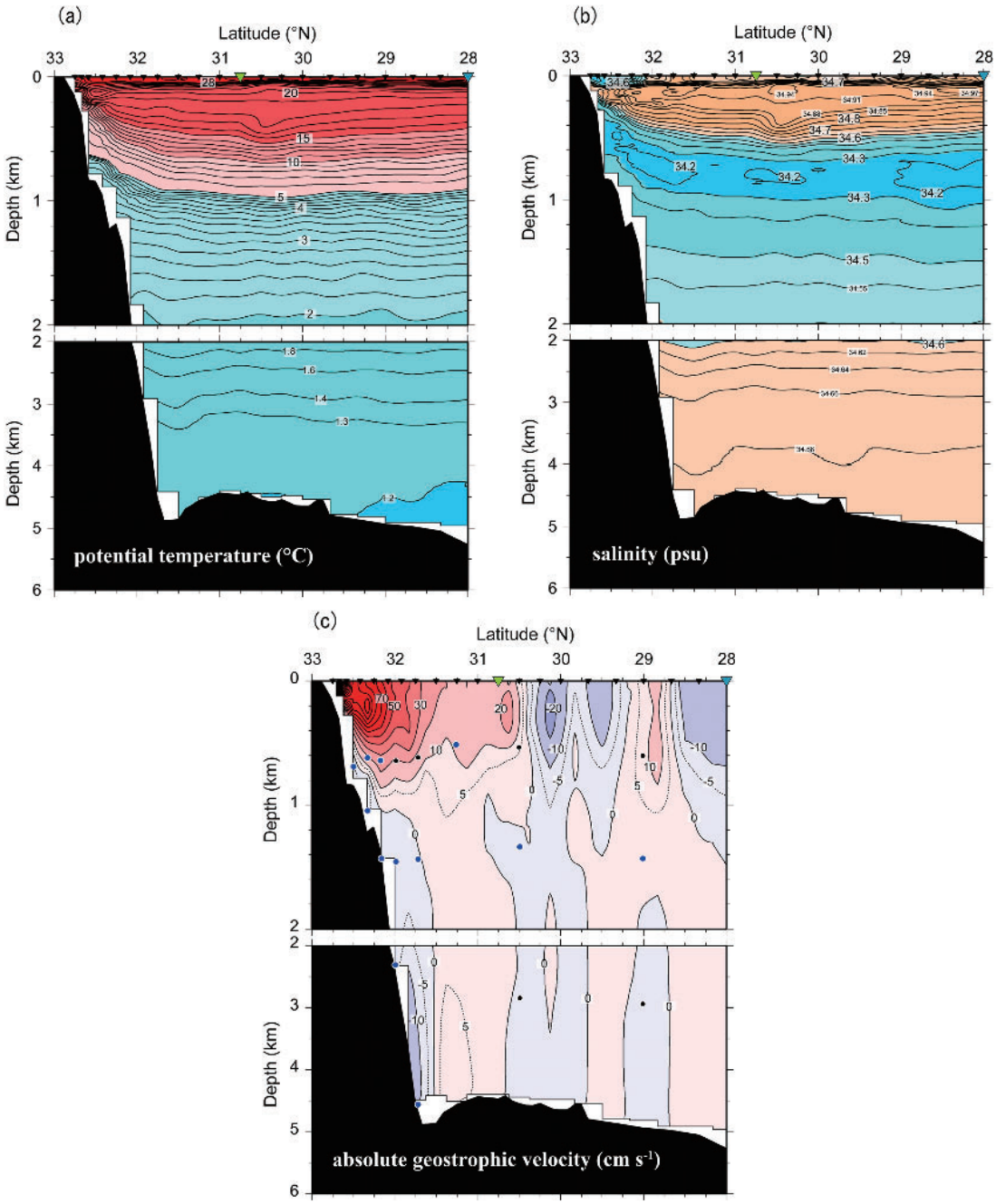

Fig. 3 Vertical sections along the ASUKA line in September 1994 of (a) potential temperature, (b) salinity, and (c) AGV (absolute geostrophic velocity; component toward 65° True); southern parts (25–28° N) are not shown. Triangles at the top denote locations of hydrographic stations; the yellowish green triangle marks the inferred offshore edge of the Kuroshio, and the light blue triangle marks the inferred southern end of the Kuroshio recirculation. In (c), dots denote locations of moored CMs; larger blue ones indicate CMs providing velocities at reference levels or on the continental slope. Courtesy of Hiroshi UCHIDA.

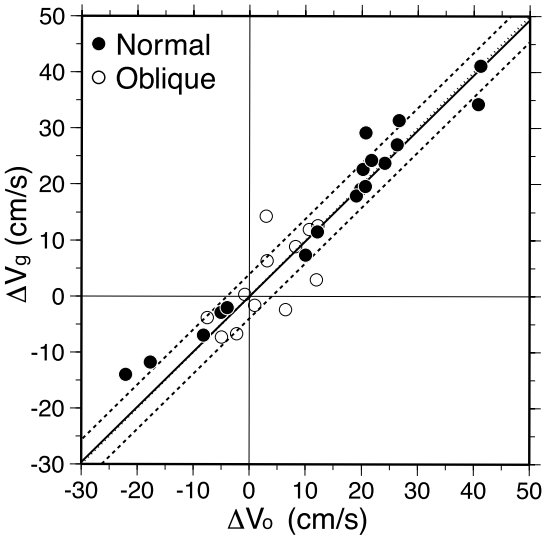

Fig. 4 Scatter plot of vertical differences of estimated geostrophic velocity (ΔVg) versus measured velocity (ΔVo) between nominal depths of 700 and 1500 m. Cases were classified as "normal" when the current direction at 700 m depth was approximately perpendicular to the ASUKA line, and as "oblique" when it was approximately parallel; the sorting criterion was 45°. The solid line denotes the regression line through the origin for 18 normal cases; dashed lines denote the root-mean-square difference from the regression line. The almost hidden dotted line denotes the one-to-one relation. Adapted from KASHIMA et al. (2003).

and 3000 m (KASHIMA et al., 2003). For these depth intervals, vertical differences of geostrophic velocity were compared with corresponding differences of measured velocity. Figure 4 shows the results for the intermediate layer (between nominal depths of 700 and 1500 m), where vertical differences ranged from −20 to 40 cm s^{-1}. The agreement was excellent for 18 comparisons of flows approximately perpendicular to the ASUKA line, with an almost one-to-one correspondence between the two values; the slope of regression line was 0.99, the correlation coefficient (CC) was 0.98, and the root-mean-square difference from the regression line was 2.8 cm s^{-1}, which was close to the estimated measurement error of 2.1 cm s^{-1}. For the deep layer (between nominal depths of 1500 and 3000 m), ten comparisons yielded corresponding values of 0.82, 0.93, 1.2 cm s^{-1}, and 2.0 cm s^{-1}. These results indicated that geostrophic balance holds very well in both the intermediate and deep layers. The best agreement was obtained when measured velocities were averaged over several days. In contrast, geostrophic balance may break down in the upper-layer near the coast, particularly when strong vertical velocity shear is induced abruptly. This condition is shown in the next subsection.

The accuracy of SSDT from the altimetry satellite TOPEX/Poseidon was examined using AGV data during 1993–1994 (IMAWAKI and UCHIDA, 1995). In physical oceanography, only anomalies from an unknown mean SSDT are useful in satellite altimetry data. This unknown mean was estimated by minimizing the difference between altimetric SSDT and *in situ* SSDT obtained simultaneously. The *in situ* SSDT was derived by horizontally integrating the sea-surface AGV, referred to the nearshore-most station (AS1), under the assumption of geostrophy. The AGV was referred to velocity measured at the 700 m level. Ten estimates of the unknown mean SSDT were averaged to obtain the final estimate. The resulting total SSDT profiles along the ASUKA line north of 30° N showed good agreement with the *in situ* SSDT profiles, having an average root-mean-square difference of 4.6 cm.

3.1 Flow field of the Kuroshio

The following features of the flow field of the Kuroshio were identified using four different types of datasets: current vectors at nominal depths of 700, 1500, and 3000 m measured by moored CMs at nine stations (UMATANI et al.,

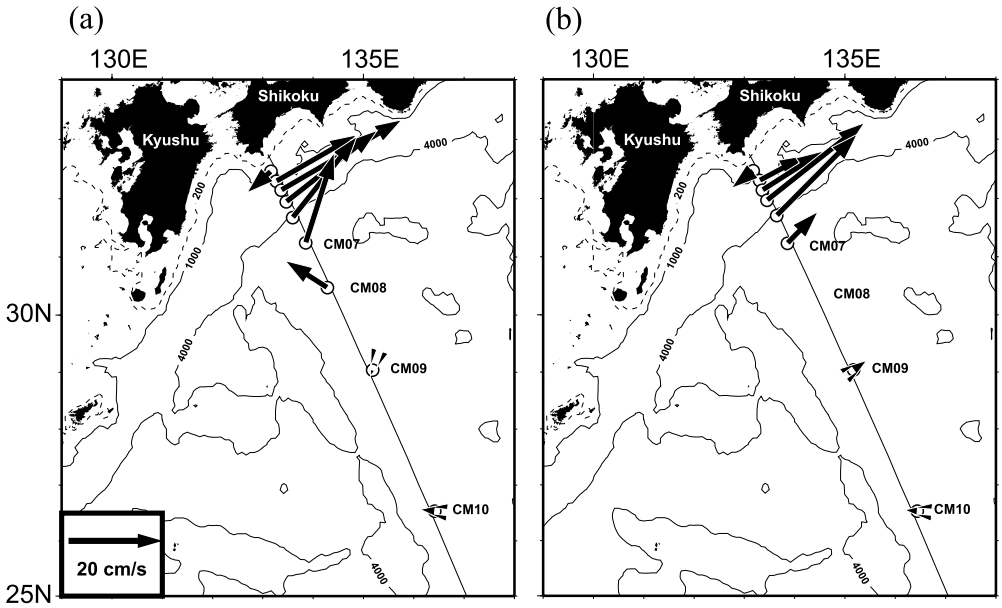

Fig. 5 Horizontal distributions of one-year mean current vectors measured at the nominal depth of 700 m. (a) First deployment (1993–1994), and (b) second deployment (1994–1995). From UMATANI et al. (2001).

2001); velocities from approximately 300 to 500 m depth measured by moored-ADCPs at two stations (TAKEUCHI et al., 2002); 12 velocity sections along the ASUKA line, from the sea-surface to 400 m depth, measured by the towed-ADCP (ZHU et al., 2001); and eight full-depth AGV sections along the ASUKA line (IM23).

Horizontal distributions of one-year mean current vectors obtained from CMs at the 700 m level are shown in Fig. 5. The strongest part of the Kuroshio, hereafter referred to as the Kuroshio axis, was located at Station CM4 during the first deployment and at Station CM5 during the second deployment, both around 32° N, with speed of 30 and 28 cm s^{-1}, respectively. Current vectors near the Kuroshio axis were oriented nearly perpendicular to the ASUKA line, confirming that the line was, on average, aligned normal to the Kuroshio flow. A tendency toward convergence was observed on the offshore side of the Kuroshio at this depth. Vertical sections of annual-mean velocity derived from moored CMs indicated that the 10 cm s^{-1} contour associated with the Kuroshio extended down to 1000 m depth.

Time series of daily current vectors at the 700 m level at all stations are shown in Fig. 6 (a). These vectors exhibited marked fluctuations, which were nearly in phase at Stations CM3 through CM6. Daily current vectors at the 1500 m level were similar to those at the 700 m level, but weaker. At the 3000 m level, currents were generally very weak and showed no apparent correlation with those at the 700 m level, except at Station CM6, as discussed in Subsection 3.3.

During the intensive observation period, the Kuroshio took two distinct paths (i.e., a near-shore path and an offshore path), both of which are classified as the non-large meander path. Current vectors at 650 m depth were estimated

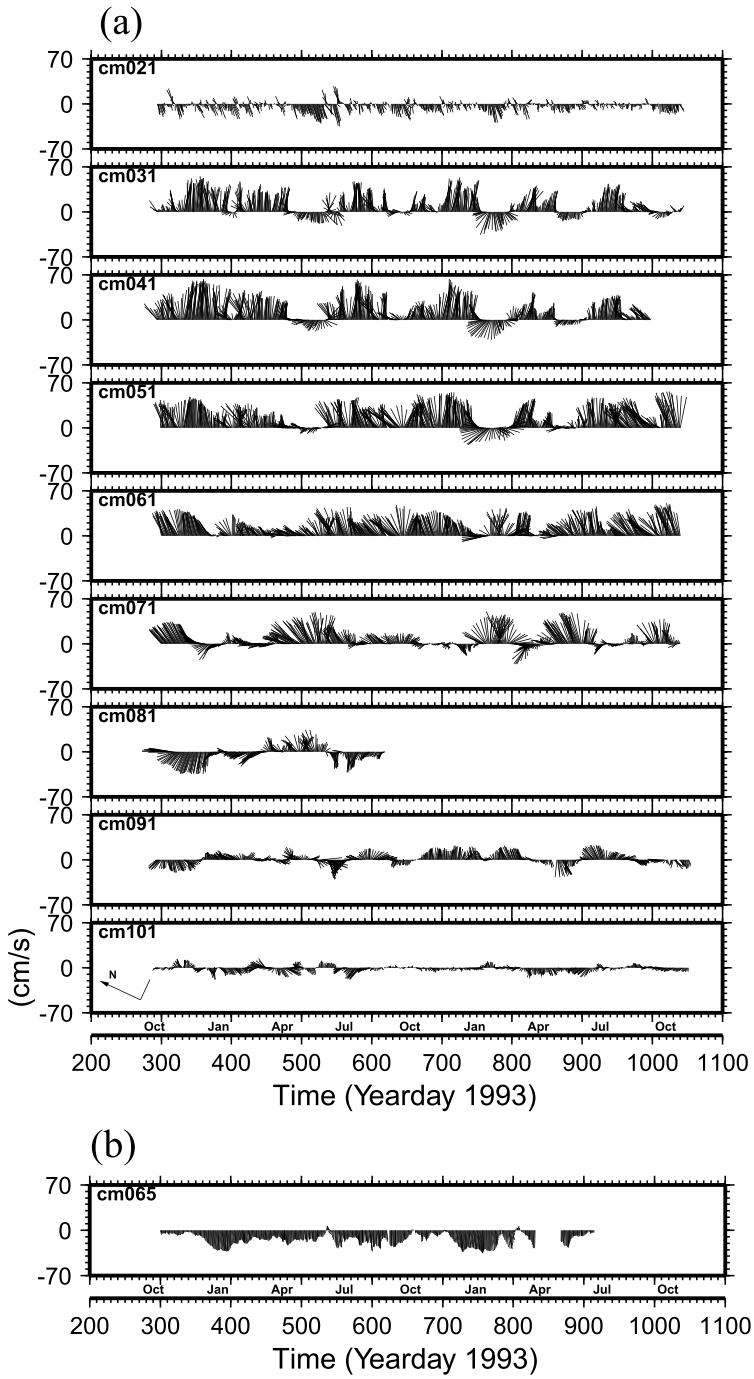

Fig. 6 Stick diagrams of daily current vectors measured during 1993–1995. The upward direction corresponds to 65° True, i.e., perpendicular to the ASUKA line. (a) Vectors at the nominal depth of 700 m at all the nine stations. (b) Vectors at 120 m above the bottom (4680 m depth) at Station CM6. From UMATANI et al. (2001).

by interpolating current vectors measured at nominal depths of 700 and 1500 m, where possible. A time–latitude plot of current speed at the 650 m depth showed that the Kuroshio took the offshore path on three occasions during the two-year period: May–June 1994, February–March 1995, and May–June 1995.

During the nearshore path, horizontally maximum velocities of the surface-layer (averaged over 0–250 m depth) observed by the towed-ADCP ranged from 80 to 150 cm s^{-1}. The Kuroshio axis was located at approximately 32° 20'N on average, as shown in Fig. 3 (a) of ZHU et al. (2001). Vertically maximum velocities near the Kuroshio axis were observed at subsurface (100–200 m depth). The moored-ADCP at Station CM2 (32° 28'N) near the coast recorded very strong velocities at 300 m depth intermittently, reaching 130–150 cm s^{-1} (Fig. 6 of TAKEUCHI et al., 2002). These strong flows were accompanied by an extremely strong vertical velocity shear between 300 and 400 m depth, reaching 1.5×10^{-2} s^{-1}. This is likely the strongest vertical velocity sheer ever directly measured in the Kuroshio. At the 650 m depth, daily velocities were up to 60 cm s^{-1}, and the Kuroshio axis was located at around 32° 05'N on average (Fig. 6 (b) of UMATANI et al., 2001). Both in the surface-layer and at the 650 m depth, the horizontal velocity shear was markedly stronger on the nearshore side than on the offshore side.

During the offshore path, horizontally maximum velocities of the surface-layer observed by towed-ADCP were approximately 100 cm s^{-1}, and the Kuroshio axis was located at 31° 20'N on average (Fig. 3 (a) of ZHU et al., 2001). At the 650 m depth, daily velocities were up to 50 cm s^{-1}, and the Kuroshio axis was located at approximately 31° 15'N (Fig. 6 (b) of UMATANI et al., 2001). At this depth, horizontal velocity shear was stronger on the nearshore side than on the offshore side, whereas in the surface-layer the velocity field was nearly symmetric with respect to the Kuroshio axis. The offshore path was characterized by remarkable countercurrents near the coast, which were the nearshore-side half of coastal cyclonic eddies associated with small meanders of the Kuroshio that originated southeast of Kyushu and propagated northeastward along the coast. The countercurrents, as observed by the two moored-ADCPs, were nearly barotropic and exhibited a very weak vertical velocity shear of 0.04×10^{-2} s^{-1} on average between 300 and 500 m depth (Fig. 8 of TAKEUCHI et al., 2002). The currents extended from the sea-surface to at least 700 m (Fig. 6 (a)), having a typical width of approximately 50 km and a mean velocity of approximately 20 cm s^{-1} (Fig. 2 of ZHU et al., 2001). Based on these values, their transport was roughly estimated at 3 Sv. These features of coastal countercurrents were also shown by time–depth diagrams of proxy AGV at Stations CM2, CM3, and CM4, derived from IES and moored CM data (KAKINOKI et al., 2008a).

In the Kuroshio recirculation region (Stations CM8 and CM9), fluctuations of daily current vectors at the 700 m level were considerably larger than their means (Fig. 6 (a)), implying that the recirculation was overwhelmed by active, propagating mesoscale eddies.

Velocities measured by the towed-ADCP (Fig. 2 of ZHU et al., 2001) are compared with those measured by moored-ADCPs (Figs. 4 and 6 of TAKEUCHI et al., 2002). A total of 18 comparisons are made: 12 at 300 m depth at Station CM2 and six at 380–390 m depth at Station CM4. The compared velocities range from − 30 to 110 cm s^{-1}. In all but one case, the difference between the measurement types is less than 20 cm s^{-1}; the exception is a 30 cm s^{-1} difference at 300 m depth at Station CM2, when the flow field changed rapidly. As a whole, they agree well

with each other, with a very high CC of 0.96, although towed-ADCP velocities are slightly lower than moored-ADCP velocities, with a mean difference of 7 cm s^{-1}.

Eight full-depth AGV sections were obtained from hydrographic surveys, referred to velocities measured at the 700 m level over the continental slope and at the 1500 m level in the offshore region, as shown in Fig. 3 (c). All AGV sections are shown in Fig. S1 in the supplementary material of IM23. These sections indicated that the main body of the Kuroshio (defined as regions with AGV $>$ 10 cm s^{-1}) was mostly confined to the upper 1000 m. Maximum velocities were observed in the upper 200 m north of 32° N, ranging from 60 to 150 cm s^{-1}. The Kuroshio recirculation was relatively weak and frequently dominated by propagating mesoscale eddies.

From the AGV sections, the offshore edge of the Kuroshio was inferred on the basis of the sign of AGT in the upper 1000 m between pairs of hydrographic stations. The inferred offshore edges corresponded closely with local maxima in SSDT along the ASUKA line (Fig. S2 in the supplementary material of IM23). On average, the offshore edge was located at 30° 50'N. In contrast, the southern end of the Kuroshio recirculation was not able to be determined using a similar method due to the influence of mesoscale eddies (Fig. S2 of IM23). Instead, it was inferred somewhat subjectively, with the aid of SSDT maps. The inferred southern end was located at 29° 20'N on average.

The estimated AGVs (Fig. S1 of IM23) are compared with velocities in the upper-layer (approximately 300–500 m depth) measured by moored-ADCPs (Fig. 6 of Takeuchi et al., 2002). The compared velocities range from 0 to 140 cm s^{-1}. At Station CM4 and below 400 m depth at Station CM2, the estimated velocities agree well with measured velocities within ± 10 cm s^{-1}, except for several cases at Station CM4, where discrepancies reach 20–30 cm s^{-1}. A markedly different situation is found in the layer shallower than 400 m depth at Station CM2, located closer to the coast. Here, measured velocities are generally higher than estimated values by approximately 20 cm s^{-1}. In particular, for the September 1994 section (Fig. 3 (c)), the difference reaches 80 cm s^{-1} at 300 m depth, associated with sharp velocity increase from 10 cm s^{-1} at 400 m depth to 140 cm s^{-1} at 300 m depth, corresponding to a strong vertical velocity shear of 1.3 $\times 10^{-2}$ s^{-1}, as measured by the moored-ADCP. These differences are likely due in part to the time required for both the density field and geostrophic velocity to adjust to abrupt changes in strong vertical velocity shear. Additionally, they may result from methodological differences; the AGVs represent averages over the distance between two hydrographic stations separated by 20 km, whereas the moored-ADCP velocities are point values at the middle of those stations. The estimated AGVs are generally consistent with upper-layer velocities measured by the towed-ADCP, although a direct comparison is not possible due to differences in observation dates.

The vertical section of the Eulerian-mean AGV (Fig. 7) was constructed from the eight AGV sections, providing a two-year mean, full-depth AGV section of the Kuroshio, for the first time, based on directly measured properties. This mean section represents the Kuroshio primarily during its nearshore path, except for one section at the beginning of the first offshore path period (May 1994), which exhibited only a weak countercurrent below 200 m depth near the coast. The main body of the Kuroshio was confined to the upper 1000 m, and the entire Kuroshio was virtually confined to the upper 1500 m. This mean flow is hereafter referred to as the

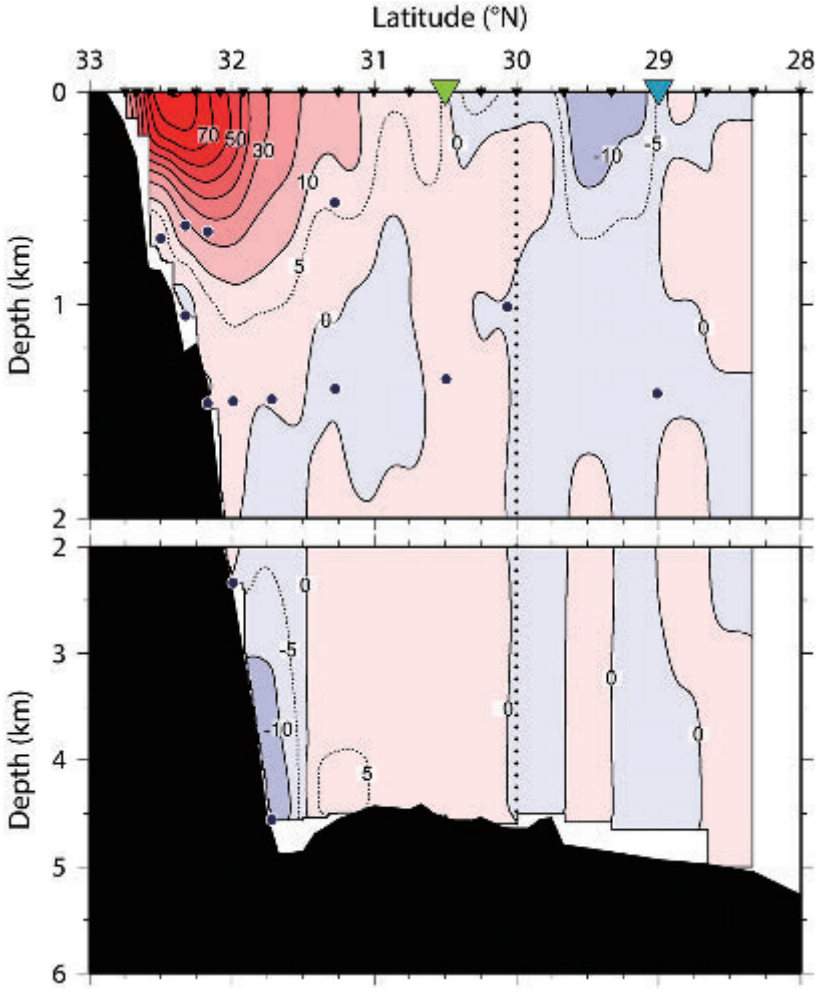

Fig. 7 Vertical section of the Eulerian-mean AGV (in cm s^{-1}) along the ASUKA line during 1994–1995. North of the dotted line at 30° N, eight AGV sections were averaged; south of this line, four sections were averaged. Triangles at the top denote locations of coordinated common hydrographic stations; the yellowish green triangle marks the inferred offshore edge of the mean Kuroshio, and the light blue triangle marks the inferred southern end of the mean Kuroshio recirculation. Dots denote mean locations of moored CMs providing velocities at reference levels or on the continental slope. From IMAWAKI et al. (2023).

mean Kuroshio. The maximum velocity (> 80 cm s^{-1}) was located at the sea-surface near the coast. Both vertical and horizontal velocity shears were stronger on the nearshore side than on the offshore side. The Kuroshio axis exhibited an offshore shift with increasing depth. These two features (i.e., velocity shear and offshore shift) are generally characteristic of mid-latitude western-boundary currents along the coast, as observed in the Kuroshio (e.g., KAWABE, 1985;

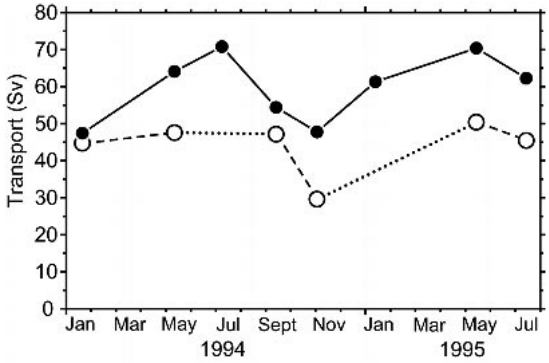

Fig. 8 Temporal series of total AGTs (absolute geostrophic transports; in Sv) of the Kuroshio (solid circles) and the throughflow Kuroshio (open circles) across the ASUKA section during 1994–1995. Adapted from IMAWAKI et al. (2023).

KANEKO et al., 1992; JOHNS et al., 2001), the Florida Current/Gulf Stream in the North Atlantic (e.g., HALKIN and ROSSBY, 1985; LEAMAN et al., 1989; JOHNS et al., 1995), and the Agulhas Current in the Indian Ocean (e.g., BRYDEN et al., 2005; BEAL et al., 2006; 2015).

BOOK et al. (2002a) derived a Eulerian-mean proxy AGV section along the ASUKA line for a five-month period (November 1993–April 1994) using IES and moored CM data, by applying the gravest empirical mode (GEM) method. The resulting flow field was essentially similar to the above-mentioned mean field in the upper 2000 m; the maximum velocity (> 90 cm s^{-1}) was located at the sea-surface near the coast, and the main body of the Kuroshio was mostly confined to the upper 1000 m. However, the deep flow structure near the continental slope, such as the deep westward flow described in Subsection 3.3, was not able to be described by their GEM method. They identified three smaller-scale meanders during the two-year observation period, in addition to three above-mentioned meanders, suggesting a four-month periodicity of Kuroshio meanders off Shikoku. This periodicity was further investigated by KASHIMA et al. (2009), who interpreted them as modulated periodic meanders having 110- or 150-day periods during 1993–2001. These variations were attributed to arrival of mesoscale eddies propagating westward from the ocean interior along 27–32° N latitudes.

3.2 Transport of the Kuroshio

Transport of the Kuroshio and the throughflow Kuroshio across the ASUKA section was estimated using multiple approaches (Table 1). From the eight full-depth AGV sections, the following transport values were estimated by IM23. The total AGT of the Kuroshio was estimated by integrating the positive AGV from the coast to the offshore edge of the Kuroshio, and from the sea-surface down to a maximum of 2000 dbar. This upper limit was imposed because contamination with deep eastward flows different from the Kuroshio, such as the eastward flow over the Nankai Trough (see the next subsection), should be minimized, and also because the Kuroshio was virtually confined to the upper 2000 m, as shown below. The total AGTs derived from the eight AGV sections provided a temporal series of Kuroshio transport estimates at relatively short intervals over a two-year period (solid circles in Fig. 8). These estimates varied substantially from 47 to 71 Sv, likely reflecting fluctuations induced by propagating mesoscale eddies as well as fluctuations of the throughflow Kuroshio and Warm Eddy off Shikoku. The mean AGT was estimated at 60 ± 9 Sv (mean ± standard deviation).

On the other hand, the total AGT of the mean Kuroshio (Fig. 7) was estimated at 47 Sv, corresponding to only 79% of the mean AGT of the instantaneous Kuroshio. This discrepancy arises because, in some cases, the instantaneous Kuroshio extended beyond the offshore edge of the

Table 1. Mean volume transports (mean ± standard deviation; in Sv) of the Kuroshio and the throughflow Kuroshio across the ASUKA (Affiliated Surveys of the Kuroshio off Cape Ashizuri) section estimated by various methods. See Section 1 for definitions and the listed sections/subsections for methodological details.

Data used	Kuroshio	throughflow Kuroshio	Duration (year)	Note	Reference	Section in the text
Total Transport						
CTD & CM	60±9	44±7	2 (1994–1995)	AGTs based on eight full-depth sections	IMAWAKI et al. (2023)	3.2
IES & CM	65±20	–	2 (1993–1995)	Proxy AGTs, using GEM method	BOOK et al. (2002a)	3.2
Altimetry	61±16	35±8	31 (1993–2024)	Proxy GTs, using an empirical relationship	UCHIDA (2025) & IMAWAKI et al. (2025)	5
Transport in the upper 1000 m						
CTD & CM	56±8	–	2 (1994–1995)	AGTs based on eight full-depth sections	IMAWAKI et al. (2023)	3.2
CTD/XBT & CM	54±13	–	2 (1993–1995)	AGTs based on 25 sections	IMAWAKI et al. (2001)	3.2
IES	45±10	–	5 (1994–1997, 2001)	Proxy GTs referred to 1000 dbar, using GEM method	KAKINOKI et al. (2008b)	4
Altimetry	57±11	42±9	7 (1992–1999)	Proxy AGTs, using an empirical relationship	IMAWAKI et al. (2001)	5

AGT: absolute geostrophic transport; CM: current-meter; CTD: conductivity-temperature-depth recorder; GEM: gravest empirical mode; GT: geostrophic transport; IES: inverted echo sounder; XBT: expendable bathy-thermograph

mean Kuroshio, while in other cases, the instantaneous Kuroshio recirculation intruded into the region of the mean Kuroshio.

Vertical profiles of AGT per unit depth for the Kuroshio showed that the transport was predominantly located in the upper 1000 m (Fig. 4 of IM23). AGTs within this upper 1000 m varied from 44 to 68 Sv, with a mean of 56 ± 8 Sv. These values represented 90–97% of the total AGT, with a mean of 93 ± 3%. For the mean Kuroshio, transport was even more concentrated in the upper 1000 m, which accounted for 97% of the total transport. The profiles also showed that AGTs between 1500 and 2000 m depth were negligibly small, confirming that the transport was virtually confined to the upper 2000 m. The trivially small transport in the deep layer is likely attributable to the bottom topography around the Kuroshio. The Tokara Strait is shallower than 690 m (NAKAMURA, 2017), and the portion of the Izu-Ogasawara Ridge over which the Kuroshio usually flows is shallower than approximately 1500 m (OTSUKA, 1985), although the Ryukyu Current region is relatively deep.

The AGT of the Kuroshio recirculation (positive denotes westward) was estimated for the upper 2000 m using a similar approach, with the exception that net AGT between hydrographic stations was integrated, instead of positive AGV. This modification was necessary because of the complex velocity field due to overlapping mesoscale eddies. Estimated AGTs of the recirculation varied from 3 to 20 Sv, with a mean of 14 ± 7 Sv. The AGTs of the throughflow Kuroshio were then estimated by subtracting the AGTs of the Kuroshio recirculation from the AGTs of the Kuroshio. Estimated AGTs varied from 30 to 50 Sv, with a mean of 44 ± 7 Sv (open circles in Fig. 8).

For comparison, ordinary GTs of the Kuroshio, referred to 2000 dbar, were similarly estimated from the full-depth sections. The deviations from the corresponding AGTs were relatively small, with a mean of 2 ± 4 Sv. Positive deviations occurred when the upper boundary of the deep westward flow over the Nankai Trough (see the next subsection) was shallower than 2000 m. These results suggested that GT referred to and calculated above 2000 dbar can be used for monitoring transport in cases where velocities at the reference level are not available (IM23).

BOOK et al. (2002a) derived a proxy time series of daily AGT of the Kuroshio from IES and moored CM data for the two-year observation period, by applying the GEM method and integrating velocity over the contiguous region of eastward AGV encompassing the Kuroshio. The resulting proxy AGTs ranged from 25 to 139 Sv, with a mean of 65 ± 20 Sv, which is slightly larger than the mean AGT of the Kuroshio (60 Sv) estimated from the eight full-depth CTD sections by IM23 (Table 1).

IMAWAKI et al. (2001) estimated the AGT of the Kuroshio in the upper 1000 m for 25 selected high-quality hydrographic sections from 1993 to 1995, referred to velocities measured at the 700 m level. Their analysis utilized plentiful XBT data in addition to CTD data. Although the XBTs provided only temperature profiles down to approximately 800 m depth, geostrophic velocities down to 1000 m depth were calculated using very tight temperature-salinity relationships and skillful extrapolation of steric height (UCHIDA and IMAWAKI, 2008). Note that most of Kuroshio transport (93% on average) is located in the upper 1000 m, as shown above. The AGT was estimated as the net transport between the coast and offshore edge of the Kuroshio.

Estimated AGTs ranged from 27 to 85 Sv, with a mean of 54 ± 13 Sv, which is slightly smaller than the mean AGT (56 Sv) in the upper 1000 m estimated from the eight full-depth

sections discussed above. A scatter plot of AGTs in the upper 1000 m versus SSDT differences across the Kuroshio (Fig. 9 (a)) revealed a strong linear relationship, with a CC of 0.90 and small standard deviation of 5.6 Sv about the regression line (IMAWAKI et al., 2001). This strong correlation can be explained by examining vertical profiles of transport per unit depth (Fig. 9 (b)). Although the original profiles exhibited considerable variability, normalization by the sea-surface transport yielded nearly identical shapes across different observations. This result indicated that the total transport was approximately proportional to the sea-surface transport, which is proportional to the SSDT difference across the Kuroshio, under the assumption of geostrophy. This linear relationship had previously been identified for the Kuroshio south of Japan (NITANI, 1975) and the Florida Current (e.g., MAUL et al., 1985), as discussed in more detail in the Appendix. This empirical relationship provided a practical method for long-term monitoring of volume transport using satellite altimetry data. The resulting time series of Kuroshio transport is shown in Section 5.

One of the main aims of the WOCE was to estimate oceanic heat transport (SIEDLER et al., 2001). To evaluate heat transport at mid-latitudes in the North Pacific, AGV and hydrographic data from the Kuroshio region, obtained during the ASUKA intensive observation, were combined with data from the WOCE Hydrographic Program P2 section along 30° N (BRYDEN and IMAWAKI, 2001). This trans-Pacific hydrographic section was carried out in 1993–1994 by three Japanese vessels: the survey vessel *Shoyo*, the fisheries research vessel *Kaiyo-maru*, and the training vessel *Bosei-maru* (e.g., YOU et al., 2003). The westernmost part of the P2 section, occupied in January 1994, was connected to the full-depth Kuroshio section occupied nearly

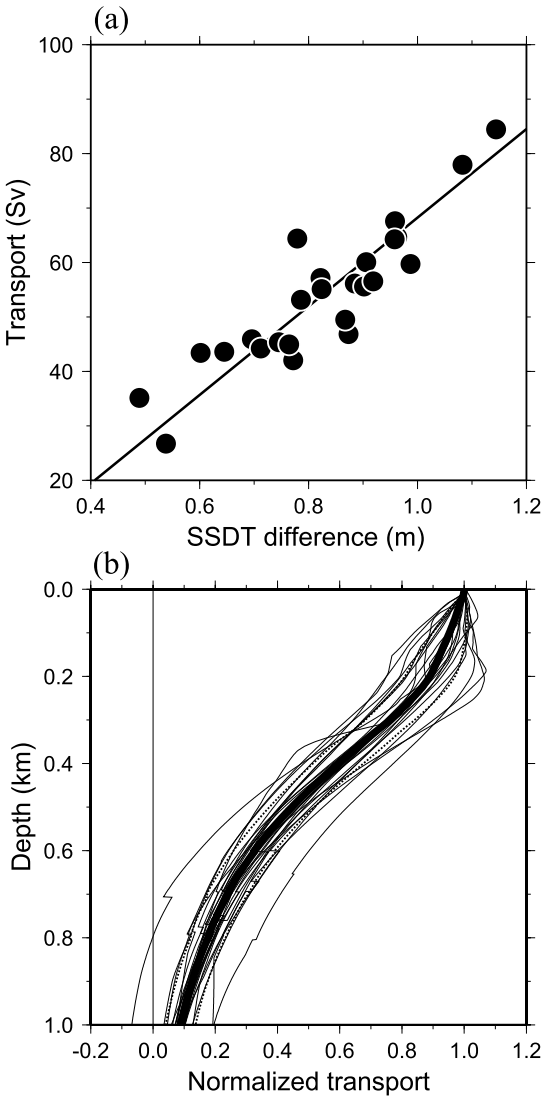

Fig. 9 AGT of the Kuroshio in the upper 1000 m during 1993–1995. (a) Scatter plot of AGTs (in Sv) versus SSDT (sea-surface dynamic topography) differences (in m) across the Kuroshio. The solid line denotes the regression line. (b) Vertical profiles of AGT per unit depth, normalized by the sea-surface AGT. The mean profile (thick line) and its standard deviation (dotted lines) are shown as well as 25 instantaneous profiles (thin lines). From IMAWAKI et al. (2001).

simultaneously, instead of the mean Kuroshio section. This decision was made because a very strong cyclonic mesoscale eddy was located precisely at the junction point, and hence its influence on the two sections should cancel out as much as possible. The estimated net northward heat transport across 30° N was 0.62×10^{15} W, corresponding to approximately 40% of the global oceanic northward heat transport ($1.6 \pm 0.4 \times 10^{15}$ W) at 24° N, as estimated by MACDONALD and BARINGER (2013). Connecting a one-time transoceanic section with a western-boundary current section remains a complex methodological challenge.

3.3 Flows under the Kuroshio

The time series of daily current vectors at the 700 m level at Station CM2 (Fig. 6 (a)) exhibited an anomalous pattern, distinctly different from the typical Kuroshio flow (UMATANI et al., 2001). Specifically, the vectors were directed primarily to the southwest, with occasional northeast, and fluctuated in an almost unidirectional manner. The two-year mean velocity vector was oriented west-southwest, with a magnitude of 7 cm s^{-1} (Fig. 5). This flow was clearly influenced by the bottom topography, because the CM was moored only 130 m above the bottom at a depth of 820 m and the observed flow direction corresponded closely with contours of the bottom topography. Note that this flow was located beneath the strong upper-layer currents of the Kuroshio. Flow speed increased when the Kuroshio took the offshore path and thus coastal countercurrents were present in the upper-layer (Fig. 6 (a)). The two-year mean velocities measured by CMs near the bottom at Stations CM3 and CM4 were -7 and -11 cm s^{-1}, respectively (KAKINOKI et al., 2008a). This steady, topographically controlled countercurrent extended along the continental slope down to a depth of 2000 m beneath the Kuroshio (Fig. 2 of UMATANI et al., 2001).

The record from the CM near the bottom at Station CM6 (Fig. 6 (b)), moored at the base of the continental slope, also exhibited atypical behavior (UMATANI et al., 2001), with the flow pattern differing markedly from that of the Kuroshio at 700 m depth at the same station (see Fig. 6 (a)). The current was directed consistently toward the west-southwest, parallel to contours of the bottom topography, and fluctuated only in speed. The maximum speed was 30 cm s^{-1}, and the speed of a 1.6-year mean vector was 15 cm s^{-1}. At 3000 m depth at the same station, the flow pattern was similar but weaker; the speed of a one-year mean vector was 8 cm s^{-1}. In contrast, the flow at 1500 m depth was weak and did not resemble the near-bottom flow. In summary, this bottom-intensifying flow weakened with decreasing depth and dissipated between 1500 and 3000 m depth.

This west-southwestward flow was clearly identified in the full-depth AGV sections (IM23) and in the mean AGV section (Fig. 7), where westward flow was observed along the lower continental slope, from approximately 2000 m depth to the bottom at about 4500 m depth, between 32° and 31° 30'N. Its velocity exceeded 10 cm s^{-1} and intensified with depth. On the offshore side, a distinct eastward flow was observed from approximately 2000 m depth down to the bottom between 31° 30' and 31° N. The flow also intensified with depth. This pair of deep westward and eastward flows was suggested to constitute a localized, anticlockwise, abyssal circulation dynamically trapped by the Nankai Trough (see Fig. 1 for location). Part of the westward flow was consistent with the basin-wide abyssal circulation in the Shikoku Basin previously suggested by FUKASAWA et al. (1987; 1995). The CC of transport between the west-

ward and eastward flows was −0.50, which was fairly high given that the westward flow appeared to contribute to the basin-wide circulation other than the localized circulation over the Trough. The AGT of the main portion of the deep westward flow over the Trough was estimated at −10 ± 3 Sv, on average, and that of the eastward flow at 8 ± 4 Sv (IM23). These deep flows were likely independent of the Kuroshio locally, as indicated by low CCs of transport between these flows and the Kuroshio.

4. After the intensive observation

Two IESs at Stations IES1 (32° 35'N) and IES7 (31° N) were maintained continuously following the ASUKA intensive observation. Proxy GT (referred to and calculated above 1000 dbar) between these two stations was estimated using the GEM method (KAKINOKI et al., 2008b). The proxy GTs derived from IES data showed excellent agreement with *in situ* GTs between the same stations. Station IES7 was located near the average offshore edge of the Kuroshio (30° 50'N), and thus estimated transports roughly represented Kuroshio transport. The estimated GTs ranged from 18 to 77 Sv, with a five-year mean of 45 ± 10 Sv. This value is approximately 20% smaller than the mean AGT of the Kuroshio in the upper 1000 m (54–56 Sv) during the intensive observation period (Table 1). The discrepancy is primarily attributable to the relatively shallow reference level of 1000 dbar used in the proxy GT calculation, which results in a loss of 18% of AGT on average (Fig. 9 (b)).

Hydrographic surveys along the ASUKA line continued through 2010, conducted by the Japan Meteorological Agency, several universities, the Fisheries Agency, the former Maritime Safety Agency, and the Japan Agency for Marine-Earth Science and Technology. The Japan Meteorological Agency, in particular, carried out surveys three to six times each year during the period 1993–2009. In addition, the northern part was occupied by the research vessel *Melville* in 2004 as a revisit of the WOCE Hydrographic Program P2. As a result, a total of 163 hydrographic sections were obtained, yielding an excellent mean section of geostrophic velocity as shown in the next section. The metadata for surveys conducted through May 2008 are summarized by UCHIDA et al. (2008).

Using the hydrographic data collected along the ASUKA line, subsequent studies were carried out as follows, although most are not considered as part of the ASUKA program. ZHU et al. (2006) compared the AGT of the Kuroshio south of Japan with those of the Kuroshio in the East China Sea and the Ryukyu Current. GUO et al. (2013) investigated nutrient transport by the Kuroshio from the East China Sea to the region south of Japan. QIU and CHEN (2021) described a cyclonic trigger meander and the Warm Eddy off Shikoku as key processes contributing to the occurrence of the large meander. NAGANO et al. (2010) compared AGTs of the Kuroshio and the throughflow Kuroshio between large meander and non-large meander states. In addition to these hydrographic surveys, six pressure-recording IESs (PIESs) were deployed along the ASUKA line during 2004–2006 to investigate bottom pressure change associated with the large meander (NAGANO et al., 2018). These PIES data were also used to derive a proxy time series of GT for the throughflow Kuroshio by combining satellite altimetry data (NAGANO et al., 2013). Furthermore, UCHIDA and IMAWAKI (2008) examined the sea-level trend south of Japan from 1992 to 2006 using these hydrographic data in combination with satellite altimetry data.

5. Time series of transport

Using the linear relationship between the

AGT of the Kuroshio and the SSDT difference across the Kuroshio, as described in Subsection 3.2, a proxy time series of Kuroshio transport was derived from TOPEX/Poseidon altimetry data as follows (IMAWAKI et al., 2001). The unknown mean SSDT for the period 1993–1995 was estimated by subtracting the altimetric anomaly from the *in situ* SSDT obtained simultaneously. The *in situ* SSDT was calculated by integrating sea-surface AGVs, referred to the tide gauge data. The AGVs were referred to velocities measured at the 700 m level.

Using the altimetrically derived total SSDT together with the previously established linear relationship, a proxy time series of AGT for the Kuroshio in the upper 1000 m was derived for seven years (1992–1999) at ten-day intervals. The altimetrically derived transports showed excellent agreement with *in situ* AGT estimates of the Kuroshio. The seven-year mean AGT of the Kuroshio was estimated at 57 ± 11 Sv, slightly larger than the two-year mean *in situ* AGT (54–56 Sv) in the upper 1000 m during the intensive observation period (Table 1). A proxy time series of AGT for the Kuroshio recirculation was also derived using a similar method, but the southern end of the recirculation was fixed at 26° N, which was close to its climatological-mean position (HASUNUMA and YOSHIDA, 1978). By subtracting the AGT of the Kuroshio recirculation from the AGT of the Kuroshio, the AGT of the throughflow Kuroshio was estimated at 42 ± 9 Sv, on average. This value was slightly smaller than the two-year mean *in situ* AGT of 44 Sv (Table 1).

As an extension of IMAWAKI et al. (2001), three-decade-long proxy time series of GT for the Kuroshio and the throughflow Kuroshio were derived as follows. Vertical sections of mean potential temperature and salinity were obtained from 145 hydrographic surveys along the ASUKA line for 1992–2006 (UCHIDA and IMAWAKI, 2008). Based on these mean sections, a geostrophic velocity section referred to 1800 dbar was calculated (UCHIDA, 2025). Here, the reference level of 1800 dbar was selected to utilize hydrographic sections slightly shallower than the 2000 dbar recommended by IM23. Subsequently, net GTs above 1800 dbar were estimated between the nearshore-most hydrographic station (AS1) and other stations, and compared with SSDT differences between the corresponding stations. As shown in Fig. 10, the comparison for stations in the offshore-side Kuroshio and Kuroshio recirculation regions revealed an extremely strong linear relationship, with a CC of 0.99 (UCHIDA, 2025). This beautiful association resulted from eliminating effect of mesoscale eddies almost perfectly by averaging a great number of hydrographic sections. While vertical profiles of transport in Fig. 9 show that the vertically integrated transport is proportional to the sea-surface transport for the whole Kuroshio, the regression line in Fig. 10 furthermore indicates that the integrated transport is proportional to the sea-surface transport for each pair of hydrographic stations with a constant ratio, even for negative transport. It suggests that the offshore-side Kuroshio and its recirculation have a common vertical velocity structure with opposite directions, which is natural because those two make up the Warm Eddy off Shikoku.

Using this linear relationship and altimetrically derived total SSDT (Fig. 11 (b)) estimated by the same method described above, time series of stream function for net GTs integrated from the coast to offshore locations along the ASUKA line were generated. The time series spanned the most recent three decades with ten-day intervals (UCHIDA, 2025).

From these time series, a proxy time series of GT for the Kuroshio (red dots and line in Fig. 11

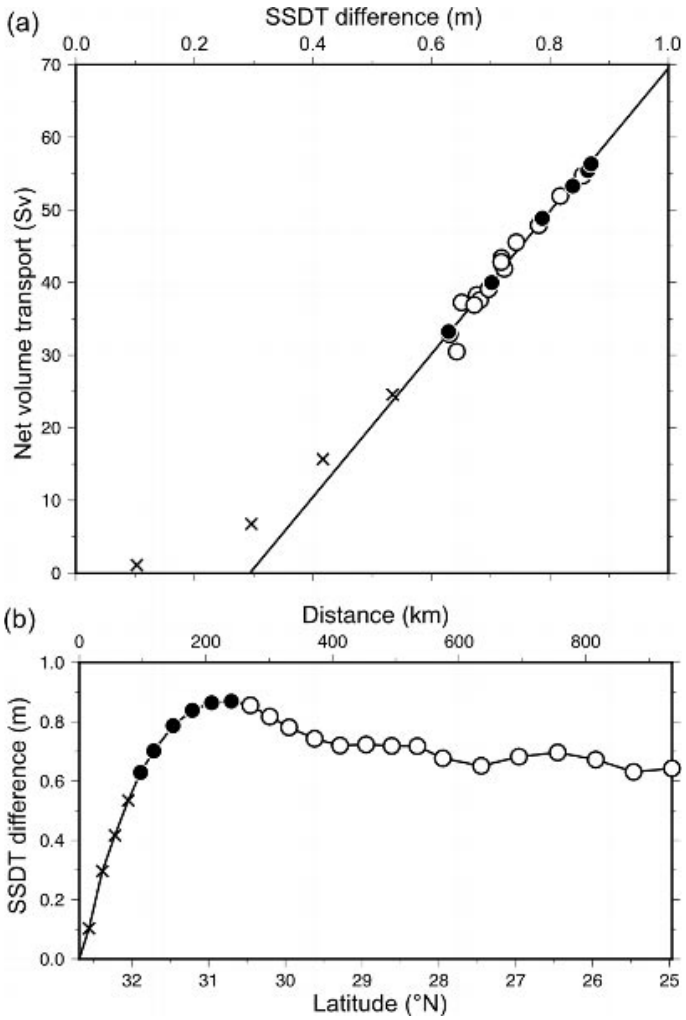

Fig. 10 Net volume transport and SSDT difference along the ASUKA line, estimated from the mean geostrophic velocity section (referred to 1800 dbar) averaged over the period 1992–2006. (a) Scatter plot of net volume transports (in Sv) versus SSDT differences (in m), both between the nearshore-most hydrographic station (AS1) and other stations along the ASUKA line. Solid and open circles show values at stations in the offshore-side Kuroshio region (AS6–AS11) and in the Kuroshio recirculation and further offshore regions, respectively. Crosses show values at four stations in the nearshore-side Kuroshio region (AS2–AS5). The solid line denotes the regression line fitted to data points shown by the solid and open circles, applicable only to the offshore regions; the four nearshore stations were excluded because water depth was shallow and hence the relationship was different. The correlation coefficient was 0.99. (b) Profile of the SSDT difference along the ASUKA line. Adapted from Uchida (2025).

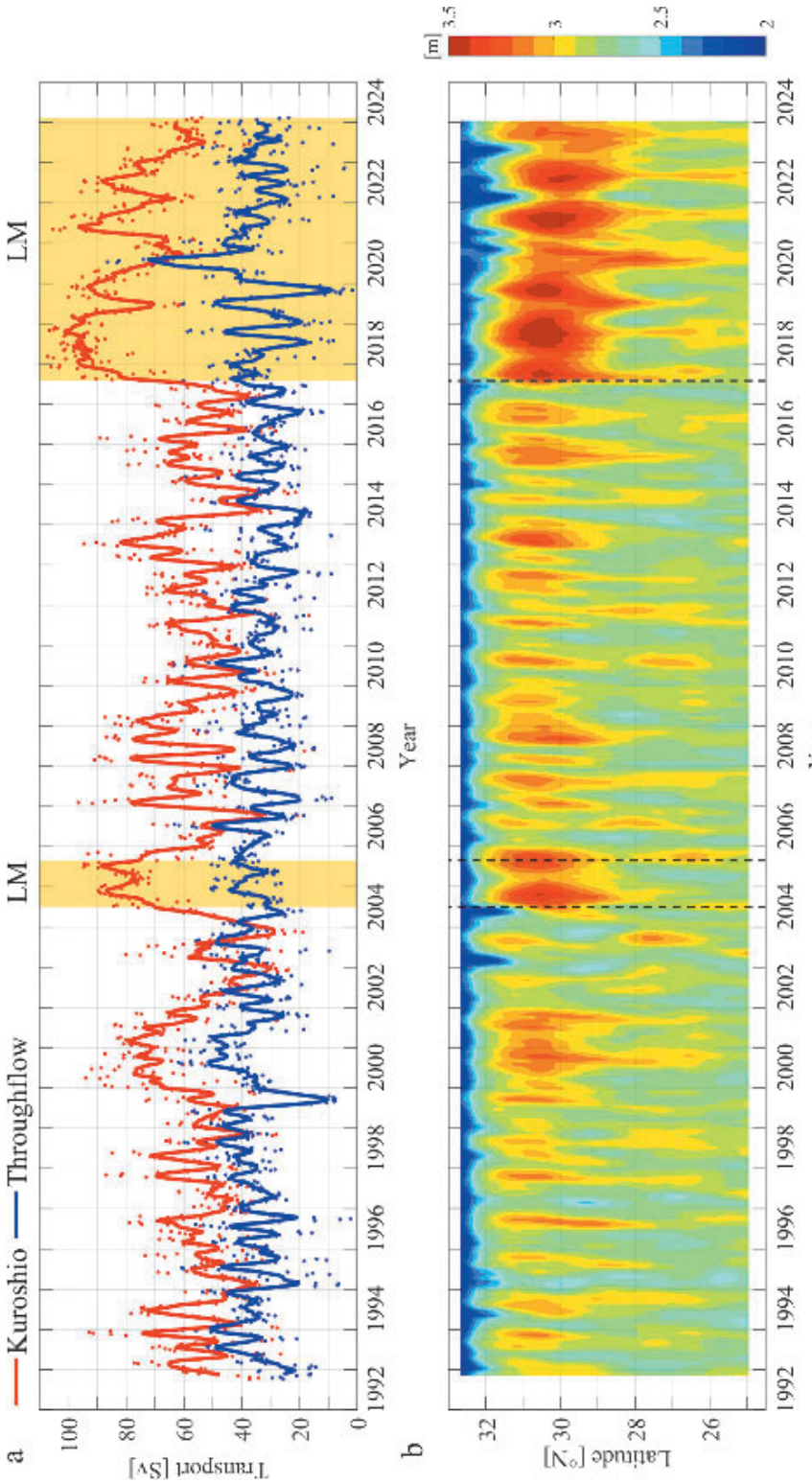

Fig. 11 Proxy time series of GT across the ASUKA section and SSDT along the ASUKA line, during 1992–2024, estimated from combined satellite altimetry and hydrography data. In (a), red and blue dots represent transport (in Sv) for the Kuroshio and the throughflow Kuroshio, respectively (see text for definitions), every ten days . Red and blue lines denote their 90-day running means. Ocher-shaded intervals mark large meander periods. (b) Latitude–time plot of SSDT (in m), after applying a 90-day running-mean filter. Vertical dashed lines denote the start and end of the large meander periods. From Imawaki et al. (2025).

(a)) was derived (IMAWAKI et al., 2025). The estimated GTs corresponded well with *in situ* AGTs during the intensive observation period. The mean GT during 1992–1999 was estimated at 54 Sv, which was slightly smaller than the mean altimetrically derived AGT (57 Sv) in the upper 1000 m for the same period (Table 1). The 31-year mean transport of the Kuroshio (for 1993–2023) was estimated at 61 ± 16 Sv. Fluctuations of Kuroshio transport were primarily associated with the Warm Eddy off Shikoku and did not significantly reflect fluctuations of the western-boundary transport expected to compensate for interior Sverdrup transport over a flat bottom (WBST), which was estimated by integrating wind-stress curl over the North Pacific subtropical gyre.

A proxy time series of GT for the throughflow Kuroshio (blue dots and line in Fig. 11 (a)) was also derived using a similar method (IMAWAKI et al., 2025). In this case, the southern end of the Kuroshio recirculation was fixed at 27° 30'N, which was close to its mean position inferred from the average SSDT profile along the ASUKA line for 1993–2023. However, agreement with *in situ* AGT estimates during the intensive observation period was limited. The discrepancy was likely due to both contamination from mesoscale eddies and incomplete coverage of the Kuroshio recirculation in some sections in IM23. The mean altimetrically derived GT of the throughflow Kuroshio for 1992–1999 was estimated at 36 Sv, which was smaller than the mean altimetrically derived AGT (42 Sv) in the upper 1000 m for the same period (Table 1). The 31-year mean of annual-mean transport of the throughflow Kuroshio was estimated at 35 ± 5 Sv. This is considerably smaller than the corresponding mean of WBST of 45 ± 4 Sv. On an interannual scale, fluctuations of throughflow transport were found to correspond with those of WBST, with a lag of approximately five years. Interestingly, the mean throughflow transport during large meander periods was nearly identical to that during non-large meander periods.

6. Discussion

The ASUKA intensive observation provided, for the first time, temporal series of full-depth AGV sections and total AGTs of the Kuroshio off Shikoku at two- to four-month intervals over a two-year period, based on a dense CM mooring array and repeated hydrographic surveys. The estimated AGTs were similar to the AGT in 1971 of 57 Sv referred to moored CM data (TAFT, 1978), but smaller than that in 1965 of 84 Sv referred to neutrally-buoyant float data (WORTHINGTON and KAWAI, 1972).

The Kuroshio east of Taiwan, marking the entrance to the East China Sea, was observed during the WOCE (1994–1996) using a moored-instrument array (designated the WOCE PCM1 array), which included CMs, ADCPs, and CTDs. The 20-month mean volume transport of the Kuroshio was estimated at 22 ± 3 Sv (JOHNS et al., 2001; LEE et al., 2001). Subsequently, the transport of the Kuroshio through the Tokara Strait was estimated at 26 ± 3 Sv on average for the period 2003–2012, based on ferry-mounted ADCP data (LIU et al., 2019). These findings indicate that the transport of the Kuroshio through the East China Sea is approximately half of the transport of the throughflow Kuroshio off Shikoku estimated from the ASUKA data. The difference between these two transport estimates is primarily attributed to the contribution of the Ryukyu Current (Fig. 1), which flows northeastward along the Ryukyu Islands and merges with the Kuroshio exiting the East China Sea (east of the Tokara Strait), as described by ICHIKAWA et al. (2004), ZHU et al. (2006), ANDRES et al. (2008), THOPPIL et al. (2016), and ZHAO et

al. (2020).

As part of the WOCE program, the Kuroshio southeast of near Cape Inubo (east of the Izu-Ogasawara Ridge) was observed in 1993 during a hydrographic survey along the 149° E meridian (designated the WOCE Hydrographic Program P10). The total AGT of the Kuroshio was estimated at 143 Sv, referred to one-time lowered-ADCP data (WIJFFELS et al., 1998). This exceptionally large transport was mostly due to a strong local recirculation south of the Kuroshio (CHEN et al., 2007). The transport of the throughflow Kuroshio was estimated at approximately 50 Sv by QIU (2002), which was comparable to some larger-end estimates obtained during the ASUKA intensive observation period.

The mean annual variation of Kuroshio transport, estimated from IES data for the period 1994–1997, showed an almost sinusoidal seasonal cycle with a maximum in September and a minimum in March, and a relatively small amplitude of 8 Sv (KAKINOKI et al., 2008b). In contrast, the mean annual cycles of transport for both the Kuroshio and the throughflow Kuroshio, estimated from the three-decade-long time series, exhibited two maxima and two minima, with peaks in July and ranges of 8–9 Sv (IMAWAKI et al., 2025); it should be noted that the estimated annual cycles are to some extent contaminated by possible seasonality of the used empirical relationship between transport and SSDT difference. Conversely, the WBST showed a simple seasonal cycle, with a maximum in December/January and a minimum in September/October, and a much larger amplitude of 47 Sv (IMAWAKI et al., 2025).

The attenuation of the annual cycle of observed transport relative to WBST was attributed to the influence of the Izu-Ogasawara Ridge, which acts as a barrier to the westward-propagating seasonal barotropic signals from the ocean interior, converting them into baroclinic signals (e.g., ISOBE and IMAWAKI, 2001). Regarding the observed delay of the western-boundary transport, a summer maximum transport was reproduced in an idealized two-layer planetary geostrophic model incorporating variable bottom topography and forced by sea-surface heat flux as well as wind-stress (SAKAMOTO, 2005). The summer maximum was also shown in the upper-layer transport induced by seasonal wind variation over the Kuroshio in the East China Sea (ZHANG et al., 2021), suggesting that local processes may contribute considerably to the seasonal cycle. Further studies are needed to fully understand the seasonal variability of Kuroshio and throughflow Kuroshio transport.

Transport of the throughflow Kuroshio is typically estimated indirectly by subtracting the transport of the Kuroshio recirculation from the transport of the Kuroshio. Direct estimation is possible if the throughflow Kuroshio and the Warm Eddy off Shikoku can be clearly separated. To distinguish these two components, the use of potential vorticity of the North Pacific Subtropical Mode Water (KANEKO et al., 2001) and water-type analysis based on spiciness (FLAMENT, 2002; NAGANO et al., 2009; 2010) has been suggested. Note that these approaches require densely spaced hydrographic stations in the Kuroshio region and a well-defined boundary, because the boundary is located in the middle of large transport. An alternative method for direct estimation is construction of net transport from the coastline, as reported by IMAWAKI et al. (2025).

The Gulf Stream between the Florida Strait and Cape Hatteras is the counterpart to the Kuroshio south of Japan (WORTHINGTON and KAWAI, 1972). HEIDERICH and TODD (2020) summarized volume transport of the Gulf Stream in the upper 1000 m, primarily based on autonomous underwater glider data obtained during 2004–2020.

The mean transport in the central portion of that region was estimated at 38–44 Sv, which is smaller than the Kuroshio transport (54–56 Sv) in the upper 1000 m during the ASUKA intensive observation period. The vertical profile and magnitude of transport per unit depth are broadly similar to those of the Kuroshio (Fig. 4 of IM23). In both flows, transport decreases monotonically from the sea-surface to 800 m depth. One noted difference is a slight increase in Gulf Stream transport between 800 to 1000 m depth. General features of the western-boundary currents in the five major oceans were briefly reviewed by IMAWAKI et al. (2013).

Numerous studies have examined the relationship between volume transport and the SSDT difference across major ocean currents worldwide, as outlined in detail in the Appendix. Most of these studies have demonstrated that the linear relationship holds, making it possible to derive proxy time series of transport from satellite altimetry data. For example, the linear relationship has been identified for the Kuroshio at the Tokara Strait (LIU et al., 2021), in the East China Sea (ANDRES et al., 2008), and east of Taiwan (YANG et al., 2001), as well as south of Japan (NITANI, 1975; IMAWAKI et al., 2001). Similar relationships have also been observed in other mid-latitude western-boundary currents, including the Oyashio in the northwestern North Pacific (ITO et al., 2004), the Gulf Stream southeast of Cape Cod (BREARLEY, 2010), the Brazil Current in the South Atlantic (GOES et al., 2019), and the Agulhas Current (BEAL and ELIPOT, 2016).

In contrast to most western-boundary currents, the East Australian Current in the South Pacific is characterized by relatively active mesoscale variability, and the linear relationship has not been confirmed (e.g., RIDGWAY et al., 2008; ZILBERMAN et al., 2018). For the Antarctic Circumpolar Current across the 140° E meridian, RINTOUL et al. (2002) reported a very tight relationship between net GT integrated from the southern end to a given latitude and the SSDT at that latitude. In contrast, for that Current in the Drake Passage, variability of narrow frontal jets required the use of a look-up table for the vertical profile of velocity as a function of latitude and sea-surface velocity, to derive a time series of transport (KOENIG et al., 2014). In the case of the Indonesian Throughflow, flows were different above and below 150 m depth, and a time-lagged partial regression model was required to estimate transport (SPRINTALL and RÉVELARD, 2014).

With respect to the deep westward flow over the Nankai Trough, a southwestward flow on the lower continental slope was first identified in 1965, with an estimated transport of −6 Sv (WORTHINGTON and KAWAI, 1972). A similar southwestward flow having a transport of −4 Sv was observed on the slope in 1971 (TAFT, 1978). FUKASAWA et al. (1987) reported a very steady west-southwestward flow, exactly aligned with contours of the local bottom topography, based on moored CM data obtained over the slope in 1984–1985. The ASUKA data further confirmed the presence of a west-southwestward flow over the slope, with a speed of 1.6-year vectorial-mean of 15 cm s^{-1} (UMATANI et al., 2001) and an associated mean transport of −10 Sv (IM23). These deep west-southwestward flows likely form part of the basin-wide anticlockwise abyssal circulation in the Shikoku Basin, originally suggested by FUKASAWA et al. (1987; 1995).

The ASUKA data also revealed an eastward flow on the offshore side of this west-southwestward flow, similarly intensifying toward the bottom. This pair of opposing abyssal flows was interpreted as a manifestation of a local anticlockwise abyssal circulation trapped dy-

namically by the Nankai Trough (IM23). A similar pair of deep counterflows had been observed over the Izu-Ogasawara Trench, consisting of a southward flow on the western slope and northward flow on the eastern slope (FUJIO et al., 2000).

7. Summary

The ASUKA Group conducted intensive observation of the Kuroshio and its recirculation off Shikoku in 1993–1995, primarily to estimate volume transport of the Kuroshio and the throughflow Kuroshio. During this period, the Kuroshio took the non-large meander path. The observation was performed by moored and towed instruments, as well as frequently repeated hydrographic surveys. The observation line was oriented almost perpendicular to the typical path of the Kuroshio off Cape Ashizuri and aligned with the subsatellite track of the TOPEX/Poseidon altimeter. Over the two-year observation period, nine moorings equipped with 33 CMs and two ADCPs, and ten IESs were deployed. A total of 42 hydrographic sections were obtained for the upper 1000 m in the Kuroshio region, including eight full-depth CTD sections. In addition, towed-ADCP measurements were conducted on 12 occasions. The following is a summary of the major findings obtained from the ASUKA dataset and its combination with satellite altimetry data.

The Kuroshio took either a nearshore or offshore path during the observation period. During the nearshore path, a very strong vertical velocity shear, reaching 1.5×10^{-2} s^{-1}, was observed in the upper-layer of the Kuroshio near the coast. In contrast, during the offshore path, a very weak velocity shear of 0.04×10^{-2} s^{-1} was observed in the upper-layer of the coastal countercurrent.

Geostrophic balance was confirmed to hold very well in both the intermediate layer (700–1500 m depth) and the deep layer (1500–3000 m depth), based on direct comparisons of vertical difference between geostrophic velocity and measured velocity. The strongest statistical agreement was obtained when measured velocities were averaged over several days.

Eight full-depth sections of AGV, referred to velocities measured at mid-depths, were obtained from CM moorings and hydrographic surveys. The total AGT of the Kuroshio was estimated by integrating eastward AGV from the coast to its offshore edge, and from the seasurface to 2000 dbar at deepest. These AGT estimates, obtained at relatively short intervals over the two years, varied from 47 to 71 Sv, with a mean of 60 Sv. Vertical profiles of AGT per unit depth revealed that the majority of transport was concentrated in the upper 1000 m. There AGTs varied from 44 to 68 Sv, with a mean of 56 Sv, corresponding to 93% of the mean total AGT.

The Eulerian-mean AGV section was derived from the series of eight full-depth AGV sections. This represented the first two-year mean, full-depth AGV section of the Kuroshio based on directly measured properties. The main body of the mean Kuroshio was confined to the upper 1000 m, and the entire flow was virtually confined to the upper 1500 m. Both vertical and horizontal velocity shear were stronger on the nearshore side than on the offshore side. The Kuroshio axis at a given depth shifted offshore with increasing depth. The AGT of the Eulerian-mean Kuroshio was estimated at 47 Sv, corresponding to 79% of the mean AGT of the instantaneous Kuroshio.

AGTs of the Kuroshio recirculation were estimated using a similar method. They varied from 3 to 20 Sv, with a mean of 14 Sv. AGTs of the throughflow Kuroshio were estimated by subtracting the recirculation transports from the

Kuroshio transports. They varied from 30 to 50 Sv, with a mean of 44 Sv.

For comparison, conventional GTs of the Kuroshio, referred to and calculated above 2000 dbar, were also estimated from the full-depth CTD sections. Deviations from the corresponding AGTs were relatively small. Therefore, GT referred to and calculated above 2000 dbar was recommended for monitoring transport of the Kuroshio when velocities at reference levels are not available.

AGTs of the Kuroshio in the upper 1000 m were strongly correlated with SSDT differences across the Kuroshio. This linear empirical relationship provided a practical basis for long-term monitoring of volume transport using satellite altimetry data. Indeed, using this relationship and TOPEX/Poseidon altimetry data, a proxy time series of AGT for the Kuroshio was derived for the period 1992–1999. Further, an extremely strong linear relationship was identified between net GTs integrated from the coast to hydrographic stations in the offshore-side Kuroshio and Kuroshio recirculation regions, and SSDT differences over the same horizontal ranges. Based on this linear regression and altimetric SSDT data, a proxy time series of GT for the Kuroshio was derived for three decades (1992–2024) at ten-day intervals. The mean transport was estimated at 61 Sv. Fluctuations of Kuroshio transport were primarily caused by the Warm Eddy off Shikoku and did not significantly reflect fluctuations of WBST.

A similar approach was used to derive a proxy time series of GT for the throughflow Kuroshio for the three decades. The mean transport was estimated at 35 Sv, which was considerably smaller than the climatological-mean WBST (45 Sv). On interannual timescales, throughflow transport closely reflected WBST variability, with a lag of approximately five years. The mean throughflow transport was nearly identical during large meander and non-large meander periods.

Numerous studies have examined the relationship between volume transport and SSDT difference for major ocean currents worldwide. For most mid-latitude western-boundary currents, the linear relationship holds and can be used to derive a proxy time series of volume transport from satellite altimetry data.

Beneath the Kuroshio, a pair of stable westward and eastward flows, both intensifying toward the bottom, was observed over the Nankai Trough. This pair of opposing flows suggested the presence of a localized, anticlockwise, abyssal circulation dynamically trapped by the Trough. A portion of the westward flow also appeared to contribute to the basin-wide abyssal circulation in the Shikoku Basin. The AGT of the principal westward flow was estimated at −10 Sv, on average, and that of the eastward flow at 8 Sv.

Appendix: Relationships between volume transport and SSDT

The following are selected studies examining the relationship between volume transport and SSDT for various currents worldwide, excluding the Kuroshio off Shikoku. In most cases, the identified relationships were used to derive proxy time series of volume transport from satellite altimetry data. These studies are summarized in Table A1.

In the Oyashio region of the northwestern North Pacific, a strong linear relationship was observed with a CC of 0.93, based on 12 comparisons between GTs (referred to 3000 dbar) and SSDT differences across the same horizontal ranges. The GTs were derived from CTD sections southeast of Hokkaido, aligned with a TOPEX/Poseidon subsatellite track, while the SSDT differences were estimated from satellite

Table A1. Summary of observed linear relationships between volume transports and SSDT (sea-surface dynamic topography) differences across ocean currents, and their application to proxy time series of transport (positive denotes northward or eastward). See the Appendix for details.

Current	Linear relationship				Proxy time series			Reference
	Transport dealt with	Data for estimating SSDT difference	Number or length of comparison	Correlation coefficent	Data used	Length (year)	Mean transport (Sv)	
Oyashio off Hokkaido	GT (0–3000 m) from CTD	Satellite altimetry	12 cases	0.93	Satellite altimetry	9	–9.5	ITO et al. (2004)
Kuroshio off Enshu-nada	GT (0–1000 m) from reversing bottles	Surface GT from reversing bottles	22 years	0.77	—	—	—	NITANI (1975)
Kuroshio off Shikoku (1)	AGT (0–1000 m) from CTD/XBT & CM	Surface AGV from CTD/XBT & CM	25 cases	0.90	Satellite altimetry	7	57	IMAWAKI et al. (2001)
Kuroshio off Shikoku (2)	Temporal-mean net GT (0–1800 m) between the coast and CTD station	Temporal-mean surface geostrophic velocity	14 years	0.99	Satellite altimetry	31	61	UCHIDA (2025) & IMAWAKI et al. (2025)
Kuroshio at Tokara Strait	Transport from ferryboat-mounted ADCP	Tide gauge	9 years	0.77 (north) 0.65 (south)	Tide gauge	15	23	LIU et al. (2021)
Kuroshio in East China Sea	Proxy AGT from CPIES	Satellite altimetry	13 months	0.88	Satellite altimetry	12	19	ANDRES et al. (2008)
Ryukyu Current off Okinawa	Proxy GT from PIES	Satellite altimetry & tide gauge	9 months	0.91	Satellite altimetry & tide gauge	9	4.5	ZHU et al. (2004)
Kuroshio off Taiwan (1)	Transport from CM, moored-ADCP & CTD	Tide gauge	20 months	0.91	—	—	—	YANG et al. (2001)
Kuroshio off Taiwan (2)	Transport from CM, moored-ADCP & CTD	Satellite altimetry	20 months	0.83	Satellite altimetry	20	21	YAN & SUN (2015)

Table A1. (*continued*)

Flow in South China Sea	Proxy GT from PIES	Satellite altimetry	22 months	0.90	Satellite altimetry	22	–1.6	ZHU et al. (2015)
Atlantic inflow through Faroe-Shetland Channel	Vertically averaged velocity from moored-ADCP	Surface velocity from moored-ADCP	13 years	0.98	Satellite altimetry	19	Not estimated	BERX et al. (2013)
Gulf Stream off Cape Cod	AGT (0–1000 m) from CTD/ lowered-ADCP	Surface AGV from CTD/ lowered-ADCP	9 cases	0.96	Satellite altimetry	7	88	BREARLEY (2010)
Yucatan Channel flow	Transport from moored-ADCP & CM	Satellite altimetry	5 years	0.63	Satellite altimetry	20	Not shown	ATHIÉ et al., 2015
Florida Current (1)	Transport from submarine cable & CM	Pressure gauges	29 cases	0.97	—	—	—	MAUL et al. (1985)
Florida Current (2)	Transport from submarine cable	Satellite altimetry	7 years	0.79	Satellite altimetry	28	31	VOLKOV et al. (2020)
Brazil Current	GT (0-500 m) from XBT	Satellite altimetry	13 years	0.64	Satellite altimetry	13	–4.1	GOES et al. (2019)
Agulhas Current	Transport from CM, moored-ADCP & CPIES	Satellite altimetry	3 years	0.71–0.90	Satellite altimetry	22	Not shown	BEAL et al. (2016)

ADCP: acoustic Doppler current profiler; AGV: absolute geostrophic velocity; CPIES: current- and pressure-recording IES; PIES: pressure-recording IES

altimetry data (ITO et al., 2004). They derived a nine-year-long proxy time series. KURODA et al. (2017) derived linear regressions between GTs estimated from CTD sections southeast of Hokkaido and SSDT differences estimated from gridded altimetry data. They examined horizontal structure of transport in detail.

For the Kuroshio off Enshu-nada (south of Honshu), a linear relationship was identified between GT (referred to 1000 dbar) and sea-surface GT, both estimated from hydrographic surveys using reversing bottles and a mechanical bathythermograph, together with velocity measurements using a geomagnetic electrokinetograph (NITANI, 1975). For the Kuroshio passing through the Tokara Strait, linear relationships between volume transport estimated from ferry-mounted ADCP data and SSDT difference derived from tide gauge records were confirmed separately for the northern and southern parts of the Strait (LIU et al., 2021). They produced a 15-year-long proxy time series. For the Kuroshio in the East China Sea, ANDRES et al. (2008) confirmed a linear relationship between proxy AGT estimated from a current- and pressure-recording IES (CPIES) array, and SSDT difference estimated from altimetry data at two locations along a TOPEX/Poseidon subsatellite track. Their study yielded a 12-year-long proxy time series.

For the Ryukyu Current southeast of Okinawa, a linear relationship was confirmed between proxy GT (referred to 2000 dbar) derived from a PIES array and SSDT difference estimated from altimetry data at a point of subsatellite track and tide gauge data (ZHU et al., 2004). A nine-year-long proxy time series of GT was derived.

For the Kuroshio east of Taiwan, three studies were carried out by using Kuroshio transport data obtained by JOHNS et al. (2001) and LEE et al. (2001), as described in Section 6. A linear relationship was observed between the Kuroshio transport and SSDT difference across the East Taiwan Channel; to estimate the SSDT difference, tide gauge data at three stations located west of the Channel were examined (YANG et al., 2001). YAN and SUN (2015) identified a pair of end-points on subsatellite tracks (for estimating SSDT difference) that provided the best correlation between the transport and altimetric SSDT difference. They derived a 20-year-long proxy time series. SHEN et al. (2014) proposed a frequency-dependent transfer function from SSDT difference to transport, as an alternative more realistic than a simple linear relationship, incorporating altimetry data, a numerical model, and the Kuroshio transport data.

For the flow at the western boundary of the northern South China Sea, a linear relationship was confirmed between proxy GT estimated from a PIES array along the Jason-1/2 subsatellite track, and SSDT difference estimated from altimetry data (ZHU et al., 2015). They yielded a 22-year-long proxy time series.

For the Indonesian Throughflow, where flows differed above and below 150 m depth, SPRINTALL and RÉVELARD (2014) developed a linear, time-lagged partial regression model between transports estimated from both moored-ADCPs and CMs, and SSDT anomalies in various regions estimated from gridded altimetry data, for three years. They derived an 18-year-long proxy time series.

The East Australian Current in the South Pacific exhibited high variability due to relatively strong mesoscale eddy activity, and a simple linear relationship was not confirmed. RIDGWAY et al. (2008) constructed a 13-year-long time series of net GT between Sydney and Wellington using a combination of XBT, CTD, and altimetry data. They suggested that new, relatively inexpensive

technologies, such as deepwater gliders, would be required for future AGT estimates, because large-scale field programs were unlikely to be undertaken. ZILBERMAN et al. (2018) proposed a more sophisticated method for estimating time series of AGT, by combining repeated high-density XBT transects, Argo float data (temperature, salinity, and trajectory), altimetry data, and historical hydrography data.

For the Atlantic inflow through the Faroe-Shetland Channel in the northern North Atlantic, very strong linear relationships were identified, with an average CC of 0.98 for eight sites, between vertically averaged velocity and sea-surface velocity, both estimated from a moored-ADCP array positioned along a TOPEX/Poseidon subsatellite track during 1998–2011 (BERX et al., 2013). They derived a 19-year-long proxy time series from altimetry data.

For the Gulf Stream southeast of the Cape Cod, BREARLEY (2010) observed a strong CC of 0.96 for nine comparisons between AGT in the upper 1000 m and SSDT difference. Both quantities were estimated from CTD sections with lowered-ADCP along a Jason-1 subsatellite track during 2003–2008. They derived a seven-year-long proxy time series from altimetry data.

In the case of the Florida Current, a strong linear relationship (CC of 0.97) was found for 29 comparisons between transport estimated from both an electromagnetic cable and moored CMs, and sea-level difference across the current estimated from pressure gauge data (MAUL et al., 1985). VOLKOV et al. (2020) confirmed this linear relationship using transport estimated from a decommissioned submarine cable and SSDT difference estimated from altimetry data at two segments of a subsatellite track. They derived a 28-year-long proxy time series.

For the Yucatan Channel flow from the Caribbean Sea to the Gulf of Mexico, a linear relationship was confirmed between transport estimated from both moored-ADCP and CM array data for five years, and SSDT difference estimated from gridded altimetry data at two locations (ATHIÉ et al., 2015). They constructed a 20-year-long proxy time series.

In numerical models for the Atlantic Ocean, HIRSCHI et al. (2009) found a significant correlation between meridional volume transport in the upper 1100 m and zonal SSDT difference, provided that transport in the western-boundary current region and that in the eastern part of the basin were considered separately.

For the Brazil Current at 22° S in the South Atlantic, GOES et al. (2019) confirmed a linear relationship between GT estimated from repeated high-density XBT transects and SSDT difference estimated from gridded altimetry data. They derived a 13-year-long proxy time series.

For the Benguela Current in the eastern South Atlantic, west of South Africa, GARZOLI et al. (1997) found a significant correlation between SSDT anomalies estimated from along-track altimetry data and proxy sea-surface dynamic height derived from IES data, from which GT in the upper 1000 m can be estimated by using an empirically determined constant. They derived a three-year-long proxy time series.

For the Agulhas Current, VAN SEBILLE et al. (2010) confirmed a linear relationship between transport and SSDT difference, using a regional numerical model, prior to large-scale observational efforts. Subsequently, BEAL et al. (2015) deployed a moored-instrument array, heavily equipped with CMs, ADCPs, and CPIESs, along a Jason-1/2 subsatellite track during 2010–2013, to obtain time series of volume transport. Based on those field data, BEAL and ELIPOT (2016) developed linear regression models between transport per unit distance and sea-surface slope. They constructed a 22-year-long proxy time ser-

ies from altimetry data.

For the Antarctic Circumpolar Current at 140° E, RINTOUL et al. (2002) found an exceptionally strong one-to-one relationship between GT (referred to 2500 dbar) integrated northward from the southern end to a given latitude, and SSDT at that latitude. Both quantities were estimated from six repeated CTD sections conducted during the 1990s. They derived a six-year-long proxy time series from gridded altimetry data. For that Current in the Drake Passage, where temporal and spatial variability of narrow fronts were important, KOENIG et al. (2014) constructed a look-up table for vertical velocity profiles as functions of latitude and sea-surface velocity, based on data from a three-year moored-CM array positioned along a Jason-1 subsatellite track. They derived a 20-year-long proxy time series of full-depth volume transport from altimetry data.

Acknowledgements

As a coordinator of the ASUKA (Affiliated Surveys of the Kuroshio off Cape Ashizuri) Group, the author expresses his profound gratitude to all the scientists, technicians, captains and crew members, supporting staff, and students who contributed to the ASUKA observation in their various ways. Without their efforts, the ASUKA observation would not have been successful. Especially, the author is indebted to core members Hiroshi ICHIKAWA, Masao FUKASAWA, Hiroshi UCHIDA, and Shin-ichiro UMATANI for their contributions to making the plan, implementing it, and producing the results. He also thanks two anonymous reviewers for their valuable comments based on very careful reading of the manuscript. The ASUKA intensive observation was financially supported by the former Ministry of Education, Science, Sports and Culture (Japan), the Office of Naval Research (United States of America), and other funding sources. This study is a contribution to the WOCE (World Ocean Circulation Experiment). Metadata for the current-meter data obtained during the ASUKA intensive observation, including stick diagrams of daily current vectors, are available at: https://www.riam.kyushu-u.ac.jp/oed/asuka/cm/index. html, and data themselves are available at: https://www.cmrecords.net/cmdac/stranger/pcm5/pcm5. html. The hydrographic data obtained by the ASUKA Group are available at: https://www.riam.kyushu-u.ac.jp/oed/asuka/ahdc/index.html. The data for proxy time series of geostrophic transport for the Kuroshio and the throughflow Kuroshio across the ASUKA section for 1992–2024 are provided in Online Resource 2 of IMAWAKI et al. (2025).

References

AMANTE, C. and B.W. EAKINS (2009): ETOPO1 1 Arc-Minute Global Relief Model: Procedures, Data Sources and Analysis, NOAA Technical Memorandum NESDIS NGDC-24. National Geophysical Data Center, NOAA. https://doi.org/10.7289/V5C8276M

ANDO, K., X. LIN, C. VILLANOY et al. (2021): Half-century of scientific advancements since the Cooperative Study of the Kuroshio and Adjacent Regions (CSK) programme — Need for a new Kuroshio research. Prog. Oceanogr., **193**, 102513. https://doi.org/10.1016/j.pocean.2021.102513

ANDRES, M., J.-H. PARK, M. WIMBUSH, X.-H. ZHU, K.-I. CHANG and H. ICHIKAWA (2008): Study of the Kuroshio/Ryukyu Current system based on satellite-altimeter and *in situ* measurements. J. Oceanogr., **64**, 937-950. https://doi.org/10.1007/s10872-008-0077-2

ATHIÉ, G., J. SHEINBAUM, R. LEBEN, J. OCHOA, M.R. SHANNON and J. CANDELA (2015): Interannual variability in the Yucatan Channel flow. Geophys. Res. Lett., **42**, 1496-1503. https://doi.org/10.1002/2014GL062674

AVISO (2016): SSALTO/DUACS User Handbook:

MSLA and (M) ADT Near-Real Time and Delayed Time Products. http://www.aviso.altimetry.fr/fileadmin/documents/data/tools/hdbk_duacs.pdf

Beal, L.M., T.K. Chereskin, Y.D. Lenn and S. Elipot (2006): The sources and mixing characteristics of the Agulhas Current. J. Phys. Oceanogr., **36**, 2060-2074. https://doi.org/10.1175/JPO2964.1

Beal, L.M. and S. Elipot (2016): Broadening not strengthening of the Agulhas Current since the early 1990s. Nature, **540**, 570-573. https://doi.org/10.1038/nature19853

Beal, L.M., S. Elipot, A. Houk and G.M. Leber (2015): Capturing the transport variability of a western boundary jet: Results from the Agulhas Current Time-Series Experiment (ACT). J. Phys. Oceanogr., **45**, 1302-1324. https://doi.org/10.1175/JPO-D-14-0119.1

Berx, B., B. Hansen, S. Østerhus, K.M. Larsen, T. Sherwin and K. Jochumsen (2013): Combining in situ measurements and altimetry to estimate volume, heat and salt transport variability through the Faroe-Shetland Channel. Ocean Science, **9**, 639-654. https://doi.org/10.5194/os-9-639-2013

Book, J.W., M. Wimbush, S. Imawaki, H. Ichikawa, H. Uchida and H. Kinoshita (2002a): Kuroshio temporal and spatial variations south of Japan determined from inverted echo sounder measurements. J. Geophys. Res., **107**, 3121. https://doi.org/10.1029/2001JC000795

Book, J., et al. (2002b): Correction to "Kuroshio temporal and spatial variations south of Japan determined from inverted echo sounder measurements" by J. Book et al. J. Geophys. Res., **107**, 3234. https://doi.org/10.1029/2002JC001678

Brearley, J.A. (2010): Upper ocean transport variability in the subtropical North Atlantic. University of Southampton, School of Ocean and Earth Science, Doctoral Thesis, 303 pp. https://eprints.soton.ac.uk/191959/

Bryden, H.L., L.M. Beal and L.M. Duncan (2005): Structure and transport of the Agulhas Current and its temporal variability. J. Oceanogr., **61**, 479-492. https://doi.org/10.1007/s10872-005-0057-8

Bryden, H.L. and M.M. Hall (1980): Heat transport by currents across 25° N latitude in the Atlantic Ocean. Science, **207**, 884-886. https://doi.org/10.1126/science.207.4433.884

Bryden, H.L. and S. Imawaki (2001): Ocean heat transport. *In* Ocean Circulation and Climate: Observing and Modelling the Global Ocean. Siedler, G., J. Church and J. Gould (eds.), Academic Press, San Diego, International Geophysics Series, Volume 77, p. 455-474.

Bryden, H.L., D.H. Roemmich and J.A. Church (1991): Ocean heat transport across 24° N in the Pacific. Deep-Sea Res., **38**, 297-324. https://doi.org/10.1016/0198-0149(91)90070-V

Chen, S., B. Qiu and P. Hacker (2007): Profiling float measurements of the recirculation gyre south of the Kuroshio Extension in May to November 2004. J. Geophys. Res., **112**, C05023. https://doi.org/10.1029/2006JC004005

Clarke, A., J. Church and J. Gould (2001): Ocean processes and climate phenomena. *In* Ocean Circulation and Climate: Observing and Modelling the Global Ocean. Siedler, G., J. Church and J. Gould (eds.), Academic Press, San Diego, International Geophysics Series, Volume 77, p. 11-30.

Escudier, P., A. Couhert, F. Mercier et al. (2017): Satellite radar altimetry: Principle, accuracy, and precision. *In* Satellite Altimetry over Oceans and Land Surfaces. Stammer, D. and A. Cazenave (eds.), CRC Press, London, p. 1-69.

Flament, P. (2002): A state variable for characterizing water masses and their diffusive stability: Spiciness. Prog. Oceanogr., **54**, 493-501. https://doi.org/10.1016/S0079-6611(02)00065-4

Fu, L.-L., E.J. Christensen, C.A. Yamarone Jr., M. Lefebvre, Y. Menard, M. Dorrer and P. Escudier (1994): TOPEX/POSEIDON mission overview. J. Geophys. Res., **99**, 24,369-24,381. https://doi.org/10.1029/94JC01761

Fujio, S., D. Yanagimoto and K. Taira (2000): Deep current structure above the Izu-Ogasawara Trench. J. Geophys. Res., **105**, 6377-6386. https://doi.org/10.1029/1999JC900324

Fukasawa, M., T. Teramoto and K. Taira (1987):

Abyssal current along the northern periphery of Shikoku Basin. J. Oceanogr. Soc. Japan, **42**, 459-472. https://doi.org/10.1007/BF02110196

Fukasawa, M., T. Teramoto and K. Taira (1995): Hydrographic structure in association with deep boundary current in the north of the Shikoku Basin. J. Oceanogr., **51**, 187-205. https://doi.org/10.1007/BF02236524

Garzoli, S.L., G.J. Goñi, A.J. Mariano and D.B. Olson (1997): Monitoring the upper southeastern Atlantic transports using altimeter data. J. Mar. Res., **55**, 453-481. https://elischolar.library.yale.edu/journal_of_marine_research/2231

Goes, M., M. Cirano, M. M. Mata and S. Majumder (2019): Long-term monitoring of the Brazil Current transport at 22° S from XBT and altimetry data: Seasonal, interannual, and extreme variability. J. Geophys. Res. Oceans, **124**, 3645-3663. https://doi.org/10.1029/2018JC014809

Grassl, H. (2001): Climate and oceans. *In* Ocean Circulation and Climate: Observing and Modelling the Global Ocean. Siedler, G., J. Church and J. Gould (eds.), Academic Press, San Diego, International Geophysics Series, Volume 77, p. 3-9.

Guo, X.Y., X.-H. Zhu, Y. Long and D.J. Huang (2013): Spatial variations in the Kuroshio nutrient transport from the East China Sea to south of Japan. Biogeosciences, **10**, 6403-6417. https://doi.org/10.5194/bg-10-6403-2013

Guo, X., X.-H. Zhu, Q.-S. Wu and D. Huang (2012): The Kuroshio nutrient stream and its temporal variation in the East China Sea. J. Geophys. Res., **117**, C01026. https://doi.org/10.1029/2011JC007292

Halkin, D. and T. Rossby (1985): The structure and transport of the Gulf Stream at 73° W. J. Phys. Oceanogr., **15**, 1439-1452. https://doi.org/10.1175/1520-0485(1985)015<1439:TSATOT>2.0.CO;2

Hasunuma, K. and K. Yoshida (1978): Splitting of the subtropical gyre in the western North Pacific. J. Oceanogr. Soc. Japan, **34**, 160-172. https://doi.org/10.1007/BF02108654

Heiderich, J. and R.E. Todd (2020): Along-stream evolution of Gulf Stream volume transport. J. Phys. Oceanogr., **50**, 2251-2270. https://doi.org/10.1175/JPO-D-19-0303.1

Hirschi, J.J-M., P.D. Killworth, J.R. Blundell and D. Cromwell (2009): Sea surface height signals as indicators for oceanic meridional mass transports. J. Phys. Oceanogr., **39**, 581-601. https://doi.org/10.1175/2008JPO3923.1

Ichikawa, H., H. Nakamura, A. Nishina and M. Higashi (2004): Variability of northeastward current southeast of northern Ryukyu Islands. J. Oceanogr., **60**, 351-363. https://doi.org/10.1023/B:JOCE.0000038341.27622.73

Imawaki, S., A.S. Bower, L. Beal and B. Qiu (2013): Western boundary currents. *In* Ocean Circulation and Climate: A 21st Century Perspective. Siedler, G., S. M. Griffies, J. Gould and J. A. Church (eds.), Academic Press, London, International Geophysics Series, Volume 103, p. 305-338.

Imawaki, S. and H. Uchida (1995): Detecting sea level profiles across the Kuroshio by a satellite altimeter. Annuals of the Disaster Prevention Research Institute, Kyoto University, **38B-2**, 655-662 (in Japanese with English abstract). http://hdl.handle.net/2433/72595

Imawaki, S., H. Uchida, H. Ichikawa, M. Fukasawa, S. Umatani and ASUKA Group (1997): Time series of the Kuroshio transport derived from field observations and altimetry data. Intl. WOCE Newsletter, **25**, 15-18.

Imawaki, S., H. Uchida, H. Ichikawa, M. Fukasawa, S. Umatani and the ASUKA Group (2001): Satellite altimeter monitoring the Kuroshio transport south of Japan. Geophys. Res. Lett., **28**, 17-20. https://doi.org/10.1029/2000GL011796

Imawaki, S., H. Uchida, H. Ichikawa, M. Fukasawa, S. Umatani and H. Yoritaka (2023): Volume transport of the Kuroshio south of Japan estimated from repeated full-depth hydrographic surveys and current measurements. J. Oceanogr., **79**, 157-183. https://doi.org/10.1007/s10872-022-00672-3

Imawaki, S., H. Uchida, Y.-X. Qiao and H. Nakamura (2025): Kuroshio volume transport over the past 3 decades estimated from combined satellite altimetry and hydrography data. J. Oceanogr.,

81, 351-359. https://doi.org/10.1007/s10872-025-00756-w

Isobe, A. and S. Imawaki (2001): Annual variation of the Kuroshio transport in a two-layer numerical model with a ridge. J. Phys. Oceanogr., **32**, 994-1009. https://doi.org/10.1175/1520-0485(2002)032<0994:AVOTKT>2.0.CO;2

Ito, S., K. Uehara, T. Miyao, H. Miyake, I. Yasuda, T. Watanabe and Y. Shimizu (2004): Characteristics of SSH anomaly based on TOPEX/POSEIDON altimetry and *in situ* measured velocity and transport of Oyashio on OICE. J. Oceanogr., **60**, 425-437. https://doi.org/10.1023/B:JOCE.0000038059.54334.6b

Johns, W.E., T.N. Lee, D. Zhang, R. Zantopp, C.-T. Liu and Y. Yang (2001): The Kuroshio east of Taiwan: Moored transport observations from the WOCE PCM-1 array. J. Phys. Oceanogr., **31**, 1031-1053. https://doi.org/10.1175/1520-0485(2001)031<1031:TKEOTM>2.0.CO;2

Johns, W.E., T.J. Shay, J.M. Bane and D.R. Watts (1995): Gulf Stream structure, transport, and recirculation near 68° W. J. Geophys. Res., **100**, 817-838. https://doi.org/10.1029/94JC02497

Kakinoki, K., S. Imawaki, K. Ichikawa, S. Umatani and M. Kashima (2008a): Variations of velocity and transport associated with coastal cyclonic eddies off Shikoku, Japan estimated from moored current meter and IES data. Reports of Research Institute for Applied Mechanics, Kyushu University, No.**135**, 53-59 (in Japanese with English abstract). https://doi.org/10.15017/14184

Kakinoki, K., S. Imawaki, H. Uchida, H. Nakamura, K. Ichikawa, S. Umatani, A. Nishina, H. Ichikawa and M. Wimbush (2008b): Variations of Kuroshio geostrophic transport south of Japan estimated from long-term IES observations. J. Oceanogr., **64**, 373-384. https://doi.org/10.1007/s10872-008-0030-4

Kaneko, A., S. Mizuno, W. Koterayama and R.L. Gordon (1992): Cross-stream velocity structures and their downstream variation of the Kuroshio around Japan. Deep-Sea Res., **39**, 1583-1594. https://doi.org/10.1016/0198-0149(92)90049-Y

Kaneko, I., Y. Takatsuki and H. Kamiya (2001): Circulation of intermediate and deep waters in the Philippine Sea. J. Oceanogr., **57**, 397-420. https://doi.org/10.1023/A:1021565031846

Kashima, M., S. Imawaki, S. Umatani, H. Uchida, Y. Hashibe, H. Ichikawa and M. Fukasawa (2003): Geostrophy in the intermediate and deep layers of the Kuroshio and its recirculation regions south of Japan. J. Oceanogr., **59**, 291-301. https://doi.org/10.1023/A:1025559709293

Kashima, M., S. Ito, K. Ichikawa, S. Imawaki, S. Umatani, H. Uchida and T. Setou (2009): Quasiperiodic small meanders of the Kuroshio off Cape Ashizuri and their inter-annual modulation caused by quasiperiodic arrivals of mesoscale eddies. J. Oceanogr., **65**, 73- 80. https://doi.org/10.1007/s10872-009-0007-y

Kawabe, M. (1985): Sea level variations at the Izu Islands and typical stable paths of the Kuroshio. J. Oceanogr. Soc. Japan, **41**, 307-326. https://doi.org/10.1007/BF02109238

Kawabe, M. (1995): Variations of current path, velocity, and volume transport of the Kuroshio in relation with the large meander. J. Phys. Oceanogr., **25**, 3103-3117. https://doi.org/10.1175/1520-0485(1995)025<3103:VOCPVA>2.0.CO;2

Koenig, Z., C. Provost, R. Ferrari, N. Sennéchael and M.-H. Rio (2014): Volume transport of the Antarctic Circumpolar Current: Production and validation of a 20 year long time series obtained from in situ and satellite observations. J. Geophys. Res. Oceans, **119**, 5407-5433. https://doi.org/10.1002/2014JC009966

Kuroda, H., T. Wagawa, S. Kakehi, Y. Shimizu, A. Kusaka, T. Okunishi, D. Hasegawa and S. Ito (2017): Long-term mean and seasonal variation of altimetry-derived Oyashio transport across the A-line off the southeastern coast of Hokkaido, Japan. Deep-Sea Res. I, **121**, 95-109. https://doi.org/10.1016/j.dsr.2016.12.006

Leaman, K.D., E. Johns and T. Rossby (1989): The average distribution of volume transport and potential vorticity with temperature at three sections across the Gulf Stream. J. Phys. Oceanogr., **19**, 36-51. https://doi.org/10.1175/1520-0485(198

9)019<0036:TADOVT>2.0.CO;2

Lee, T.N., W.E. Johns, C.T. Liu, D. Zhang, R. Zantopp and Y. Yang (2001): Mean transport and seasonal cycle of the Kuroshio east of Taiwan with comparison to the Florida Current. J. Geophys. Res., **106**, 22,143-22,158. https://doi.org/10.1029/2000JC000535

Liu, Z.-J., H. Nakamura, X.-H. Zhu, A. Nishina, X. Guo and M. Dong (2019): Tempo-spatial variations of the Kuroshio current in the Tokara Strait based on long-term ferryboat ADCP data. J. Geophys. Res., **124**, 6030-6049. https://doi.org/10.1029/2018JC014771

Liu, Z.-J., X.-H. Zhu, H. Nakamura, A. Nishina, M. Wang and H. Zheng (2021): Comprehensive observational features for the Kuroshio transport decreasing trend during a recent global warming hiatus. Geophys. Res. Lett., **48**, e2021GL094169. https://doi.org/10.1029/2021GL094169

Long, Y., X.-H. Zhu, X. Guo and H. Huang (2018): Temporal variation of Kuroshio nutrient stream south of Japan. J. Geophys. Res., **123**, 7896-7913. https://doi.org/10.1029/2017JC013635

Macdonald, A.M. and M.O. Baringer (2013): Ocean heat transport. *In* Ocean Circulation and Climate: A 21st Century Perspective. Siedler, G., S.M. Griffies, J. Gould and J.A. Church (eds.), Academic Press, London, International Geophysics Series, Volume 103, p. 759-785.

Macdonald, A.M. and C. Wunsch (1996): An estimate of global ocean circulation and heat fluxes. Nature, **382**, 436-439. https://doi.org/10.1038/382436a0

Maul, G.A., F. Chew, M. Bushnell and D.A. Mayer (1985): Sea level variation as an indicator of Florida Current volume transport: Comparisons with direct measurements. Science, **227**, 304-307. https://doi.org/10.1126/science.227.4684.304

Nagano, A., T. Hasegawa, H. Matsumoto and K. Ariyoshi (2018): Bottom pressure change associated with the 2004-2005 large meander of the Kuroshio south of Japan. Ocean Dynamics, **68**, 847-865. https://doi.org/10.1007/s10236-018-1169-1

Nagano, A., K. Ichikawa, H. Ichikawa, M. Konda and K. Murakami (2009): Synoptic flow structures in the confluence region of the Kuroshio and the Ryukyu Current. J. Geophys. Res., **114**, C06007. https://doi.org/10.1029/2008JC005213

Nagano, A., K. Ichikawa, H. Ichikawa, M. Konda and K. Murakami (2013): Volume transports proceeding to the Kuroshio Extension region and recirculating in the Shikoku Basin. J. Oceanogr., **69**, 285-293. https://doi.org/10.1007/s10872-013-0173-9

Nagano, A., K. Ichikawa, H. Ichikawa, H. Tomita, H. Tokinaga and M. Konda (2010): Stable volume and heat transports of the North Pacific subtropical gyre revealed by identifying the Kuroshio in synoptic hydrography south of Japan. J. Geophys. Res., **115**, C09002. https://doi.org/10.1029/2009JC005747

Nakamura, H. (2017): Kuroshio path and volume transport variations from Luzon Island to the eastern coast of Kyushu. Oceanography in Japan, **26**, 113-147 (in Japanese with English abstract). https://kaiyo-gakkai.jp/jos/uminokenkyu/vol26/26-4/26-4-nakamura.pdf

Nakano, T., I. Kaneko and Y. Takatsuki (1994): The Kuroshio structure and transport estimated by the inverse method. J. Phys. Oceanogr., **24**, 609-618. https://doi.org/10.1175/1520-0485(1994)024<0609:TKSATE>2.0.CO;2

Nitani, H. (1975): Variation of the Kuroshio south of Japan. J. Oceanogr. Soc. Japan, **31**, 154-173. https://doi.org/10.1007/BF02107107

Otsuka, K. (1985): Characteristics of the Kuroshio in the vicinity of the Izu Ridge. J. Oceanogr. Soc. Japan, **41**, 441-451. https://doi.org/10.1007/BF02109038

Qiu, B. (2002): The Kuroshio Extension system: Its large-scale variability and role in the midlatitude ocean-atmosphere interaction. J. Oceanogr., **58**, 57-75. https://doi.org/10.1023/A:1015824717293

Qiu, B. and S. Chen (2021): Revisit of the occurrence of the Kuroshio large meander south of Japan. J. Phys. Oceanogr., **51**, 3679-3694. https://doi.org/10.1175/JPO-D-21-0167.1

Ridgway, K.R., R.C. Coleman, R.J. Bailey and P. Sutton (2008): Decadal variability of East Austral-

ian Current transport inferred from repeated high-density XBT transects, a CTD survey and satellite altimetry. J. Geophys. Res., **113**, C08039. https://doi.org/10.1029/2007JC004664

RINTOUL, S.R., S. SOKOLOV and J. CHURCH (2002): A 6 year record of baroclinic transport variability of the Antarctic Circumpolar Current at 140° E derived from expendable bathythermograph and altimeter measurements. J. Geophys. Res., **107** (C10), 3155. https://doi.org/10.1029/2001JC000787

SAKAMOTO, T. (2005): Effect of air-sea heat exchange on seasonal transport variation of the Kuroshio. J. Mar. Res., **63**, 579-600. https://elischolar.library.yale.edu/cgi/viewcontent.cgi?article=1091&context=journal_of_marine_research

SHEN, M.-L., Y.-H. TSENG, S. JAN, C.-C. YOUNG and M.-D. CHIOU (2014): Long-term variability of the Kuroshio transport east of Taiwan and the climate it conveys. Prog. Oceanogr., **121**, 60-73. https://doi.org/10.1016/j.pocean.2013.10.009

SIEDLER, G., J. CHURCH and J. GOULD (eds.) (2001): Ocean Circulation and Climate: Observing and Modelling the Global Ocean. Academic Press, San Diego, International Geophysics Series, Volume 77, 715 pp.

SPRINTALL, J. and A. RÉVELARD (2014): The Indonesian throughflow response to Indo-Pacific climate variability. J. Geophys. Res., **119**, 1161-1175. https://doi.org/10.1002/2013JC009533

SUGIMOTO, S., K. HANAWA, K. NARIKIYO, M. FUJIMORI and T. SUGA (2010): Temporal variations of the net Kuroshio transport and its relation to atmospheric variations. J. Oceanogr., **66**, 611-619. https://doi.org/10.1007/s10872-010-0050-8

TAFT, B.A. (1972): Characteristics of the flow of the Kuroshio south of Japan. *In* Kuroshio: Its Physical Aspects. STOMMEL, H. and K. YOSHIDA (eds.), Univ. Tokyo Press, p. 165-216.

TAFT, B.A. (1978): Structure of Kuroshio south of Japan. J. Mar. Res., **36**, 77-117. https://elischolar.library.yale.edu/journal_of_marine_research/1424

TAKEMATSU, M., K. KAWATATE, W. KOTERAYAMA, T. SUHARA and H. MITSUYASU (1986): Moored instrument observations in the Kuroshio south of Kyushu. J. Oceanogr. Soc. Japan, **42**, 201-211. https://doi.org/10.1007/BF02109354

TAKEUCHI, M., S. IMAWAKI, S. UMATANI, K. YAMADA, H. UCHIDA and M. FUKASAWA (2002): Velocity structures of the Kuroshio and coastal cyclonic eddies off Shikoku, Japan observed by moored ADCPs. Reports of Research Institute for Applied Mechanics, Kyushu University, No.**123**, 29-38 (in Japanese with English abstract). https://doi.org/10.15017/6769081

TALLEY, L.D. (1984): Meridional heat transport in the Pacific Ocean. J. Phys. Oceanogr., **14**, 231-241. https://doi.org/10.1175/1520-0485(1984)014<0231:MHTITP>2.0.CO;2

THOPPIL, P.G., E.J. METZGER, H.E. HURLBURT, O.M. SMEDSTAD and H. ICHIKAWA (2016): The current system east of the Ryukyu Islands as revealed by a global ocean reanalysis. Prog. Oceanogr., **141**, 239-258. https://doi.org/10.1016/j.pocean.2015.12.013

UCHIDA, H. (2025): The Kuroshio transport time series estimated from satellite altimeter data. JAMSTEC. https://doi.org/10.17596/0004021

UCHIDA, H. and S. IMAWAKI (2008): Estimation of the sea level trend south of Japan by combining satellite altimeter data with in situ hydrographic data. J. Geophys. Res., **113**, C09035. https://doi.org/10.1029/2008JC004796

UCHIDA, H., S. IMAWAKI, H. ICHIKAWA and the ASUKA GROUP (2008): ASUKA Hydrographic Data Collection. Reports of Research Institute for Applied Mechanics, Kyushu University, No.**135**, 21-31. https://doi.org/10.15017/14180

UMATANI, S., M. KASHIMA, S. IMAWAKI, H. ICHIKAWA and M. FUKASAWA (2001): Structures and variability of the Kuroshio off Shikoku, Japan revealed by direct current measurements. Reports of Research Institute for Applied Mechanics, Kyushu University, No.**121**, 87-94 (in Japanese with English abstract). https://doi.org/10.15017/6768408

VAN SEBILLE, E., L.M. BEAL and A. BIASTOCH (2010): Sea surface slope as a proxy for Agulhas Current strength. Geophys. Res. Lett., **37**, L09610.

https://doi.org/10.1029/2010GL042847

Volkov, D.L., R. Domingues, C.S. Meinen, R. Garcia, M. Baringer, G. Goni and R.H. Smith (2020): Inferring Florida Current volume transport from satellite altimetry. J. Geophys. Res., **125**, e2020JC016763. https://doi.org/10.1029/2020JC016763

Wei, Y., D. Huang and X.-H. Zhu (2013): Interannual to decadal variability of the Kuroshio Current in the East China Sea from 1955 to 2010 as indicated by in-situ hydrographic data. J. Oceanogr., **69**, 571-589. https://doi.org/10.1007/s10872-013-0193-5

Wijffels, S.E., M.M. Hall, T. Joyce, D.J. Torres, P. Hacker and E. Firing (1998): Multiple deep gyres of the western North Pacific: A WOCE section along 149° E. J. Geophys. Res., **103**, 12,985-13,009. https://doi.org/10.1029/98JC01016

Worthington, L.V. and H. Kawai (1972): Comparison between deep sections across the Kuroshio and the Florida Current and Gulf Stream. *In* Kuroshio: Its Physical Aspects. Stommel, H. and K. Yoshida (eds.), Univ. Tokyo Press, p. 371-385.

Wunsch, C. (1978): The North Atlantic general circulation west of 50° W determined by inverse methods. Rev. Geophys., **16**, 583-620. https://doi.org/10.1029/RG016i004p00583

Yan, X. and C. Sun (2015): An altimetric transport index for Kuroshio inflow northeast of Taiwan Island. Science China Earth Sciences, **58**, 697-706. https://doi.org/10.1007/s11430-014-5024-z

Yang, Y., C.-T. Liu, T.N. Lee, W. Johns, H.-W. Li and M. Koga (2001): Sea surface slope as an estimator of the Kuroshio volume transport east of Taiwan. Geophys. Res. Lett., **28**, 2461-2464. https://doi.org/10.1029/2000GL011709

You, Y., N. Suginohara, M. Fukasawa, H. Yoritaka, K. Mizuno, Y. Kashino and D. Hartoyo (2003): Transport of North Pacific Intermediate Water across Japanese WOCE sections. J. Geophys. Res., **108**, 3196. https://doi.org/10.1029/2002JC001662

Zhang, Z.-L., H. Nakamura and X.-H. Zhu (2021): Seasonal velocity variations over the entire Kuroshio path part II: Dynamical interpretation for the current speed variation. J. Oceanogr., **77**, 745-761. https://doi.org/10.1007/s10872-021-00603-8

Zhao, R., H. Nakamura, X.-H. Zhu, J.-H. Park, A. Nishina, C. Zhang, H. Na, C. Jeon, Z.-N. Zhu and H.S. Min (2020): Tempo-spatial variations of the Ryukyu Current southeast of Miyakojima Island determined from mooring observations. Science Rep., **10**, 6656. https://doi.org/10.1038/s41598-020-63836-5

Zhu, X.-H., H. Ichikawa, K. Ichikawa and K. Takeuchi (2004): Volume transport variability southeast of Okinawa Island estimated from satellite altimeter data. J. Oceanogr., **60**, 953-962. https://doi.org/10.1007/s10872-005-0004-8

Zhu, X.-H., A. Kaneko, T. Saito and N. Gohda (2001): Kuroshio stream path variation and its associated velocity structures south of Shikoku, Japan. Geophys. Res. Lett., **28**, 4615-4618. https://doi.org/10.1029/2001GL013730

Zhu, X.-H., J.-H. Park and I. Kaneko (2006): Velocity structures and transports of the Kuroshio and the Ryukyu Current during fall of 2000 estimated by an inverse technique. J. Oceanogr., **62**, 587-596. https://doi.org/10.1007/s10872-006-0078-y

Zhu, X.-H., R. Zhao, X. Guo, Y. Long, Y.-L. Ma and X. Fan (2015): A long-term volume transport time series estimated by combining in situ observation and satellite altimeter data in the northern South China Sea. J. Oceanogr., **71**, 663-673. https://doi.org/10.1007/s10872-015-0305-5

Zilberman, N.V., D.H. Roemmich, S.T. Gille and J. Gilson (2018): Estimating the velocity and transport of western boundary current systems: A case study of the East Australian Current near Brisbane. J. Atmos. Oceanic Technol., **35**, 1313-1329. https://doi.org/10.1175/JTECH-D-17-0153.1

Received: March 14, 2025
Accepted: June 27, 2025

La mer 63 : 95–121, 2025, https://doi.org/10.32211/lamer.63.3-4_95
Société franco-japonaise d'Océanographie, Tokyo

Spatiotemporal variability and ENSO modulation of subsurface anticyclonic eddies (Puddies) in the Peru-Chile eastern boundary upwelling system

Gandy Maria ROSALES QUINTANA[1)], Takeyoshi NAGAI[2)], and Luis Alfredo ICOCHEA SALAS[3)]

Abstract: In eastern boundary upwelling systems (EBUSs), eddies are crucial for offshore transport of biogeochemical tracers and their vertical exchanges. We investigate the spatial and temporal variability of subsurface-intensified anticyclonic eddies (Puddies) in the Peruvian EBUS using high-resolution reanalysis and observations. Results show that subsurface intensified anticyclonic eddies dominate the subsurface layer, accounting for 54% of the total number of subsurface eddies. They exhibit a marked seasonal cycle, peaking in austral autumn closely aligned with eddy kinetic energy and Peru-Chile Undercurrent (PCUC) variability. The number of subsurface intensified anticyclonic eddies increases during El Niño events (1997–1998, 2015–2016), and moderately warm years (2008, 2012 and 2014), coinciding with a deepening of the $\sigma_\theta = 26$–isopycnal near the coast, as the equatorial warm pool propagates poleward as the coastal trapped waves. This propagating deepening of the isopycnal intensifies the PCUC and fosters greater subsurface eddy generation. Several methods were used to estimate the phase speed of the propagation. For the reanalysis data, the poleward phase speeds of the first baroclinic mode internal Kelvin wave obtained by solving the vertical modal equation range from 0.8 to 1.7 m s^{-1} with higher values in higher latitude, that are consistent very well with the direct estimation of the propagation speeds using the first order polynomial fit to the peaks of isopycnal displacement. Using the coherence spectral analysis, the mean propagation speed of 40–85–m bandpassed σ_θ observation data between Chicama and Callao was estimated to be 0.87 m s^{-1}, consistent with those estimated using reanalysis. These findings underscore how large-scale climate variability, through coastal-trapped-Kelvin waves propagation and subsequent PCUC intensification, significantly modulates the subsurface eddy activity in the Peruvian EBUS.

Keywords : Subsurface anticyclonic eddies, Puddies, Peru-Chile Undercurrent, ENSO.

1) Graduate School of Marine Science and Technology, Tokyo University of Marine Science and Technology, Tel: +81–80–8372–2291, email: gandy.rosales@gmail.com
2) Department of Ocean Sciences, Tokyo University of Marine Science and Technology, Tel: +81–3–5463–0460 , email: tnagai@kaiyodai.ac.jp
3) La Molina National Agrarian University, Faculty of Fisheries. Tel: + 51–999–979–988, email: licochea@lamolina.edu.pe
* Corresponding author:
Gandy Maria ROSALES QUINTANA
(gandy.rosales@gmail.com)

1. Introduction

The Peru-Chile Undercurrent (PCUC) is a subsurface poleward flowing current that runs along the coasts of Peru and Chile. Previous studies reported that the PCUC is sourced primarily by the southern branch of the Equatorial Undercurrent (EUC) (Lukas and Firing, 1984; Toggweiler et al., 1991; Rosales Quintana et al., 2021). The influence of the EUC is intensified especially when warm events or El Niños occur (Rosales Quintana et al., 2021). Under neutral El Niño southern oscillation (ENSO) conditions, the EUC's contribution to the PCUC is minimal. Instead, the primary and secondary Equatorial Countercurrents at around 8°S and 10°S appear to play a more substantial role (Montes et al., 2010).

Several studies pointed out that the PCUC, when flowing over abrupt topographic features, initiates the formation of subsurface eddies (Contreras et al., 2019; Thomsen et al., 2016). When the PCUC generates potential vorticity (PV) with a sign opposite to the background values at the sloping bottom boundary, submesoscale instabilities, such as centrifugal and symmetric instabilities, can be triggered, leading to intense microscale turbulence. This turbulent mixing adjusts PV to a neutral value, often resulting in subsurface eddies characterized by lenses of near-zero PV water that detaches from the slope as anticyclones. These subsurface anticyclones and cyclones tend to be highly coherent and initially form at small submesoscale, commonly referred to as submesoscale coherent vortices (SCVs) (Molemaker et al., 2015; Thomsen et al., 2016). SCVs, often being nutrient-rich and dominated by anticyclones in the subsurface layers, frequently coalesce into larger mesoscale subsurface eddies (Molemaker et al., 2015). Identified in several eastern boundary upwelling systems (EBUS), these subsurface anticyclonic eddies are commonly named after the undercurrents that generate them, such as Cuddies (California Undercurrent Eddies) and Puddies (Peru-Chile Undercurrent Eddies). Furthermore, surface eddies within EBUS are known to play a role in transporting nutrients offshore and dark subsurface layers, leading to a reduction in primary production (Gruber et al., 2011). They have been found to significantly influence the heat budget, likely providing feedback to the tropical Pacific climate system by influencing sea surface temperatures, thus affecting large-scale winds over timescale consistent with ENSO (Toniazzo, 2010; Colas et al., 2012; Takahashi and Dewitte, 2016). A study by Conejero et al. (2020) demonstrated that the interannual variability in the kinetic energy of surface eddy is mainly associated with strong Eastern Pacific El Niño events, which intensify mesoscale activity off Peru, while Central Pacific El Niños showed minimal influence. Although subsurface eddies have widely been recognized within EBUS, their main characteristics and interannual variation, especially under extreme events such as El Niño still have received much less attention compared to their surface counterparts (Chaigneau et al., 2008; Chelton et al., 2011; Espinoza-Morriberón et al., 2019).

Combes et al. (2015) employed a ROMS model at 1/12° resolution to study eddies and Puddies, revealing a strong correlation between intrathermocline eddies (ITEs), or Puddies, and the ENSO equatorial signal. Their study found an inverse relationship between PCUC transport and the volume of coastal waters transported by Puddies with fewer Puddies forming during El Niño. However, this counterintuitive mechanism linking decreased Puddy formation with intensified PCUC transport during El Niño still remains elusive. In contrast, Conejero et al. (2020) reported that the subsurface EKE at 200 m depth

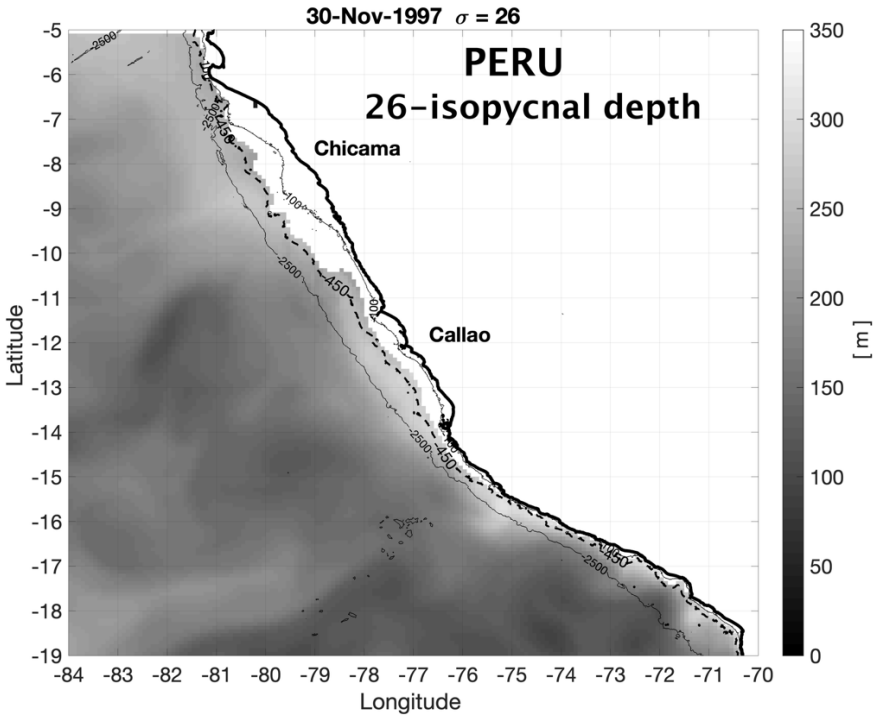

Fig. 1 Map of the Peruvian coast, showing Chicama (7.8°S - 79.7°W) and Callao (12 °S - 77.3°W) observational stations location, and the 450 m isobath along the coastline. Background shows a snapshot of σ_θ= 26 isopycnal depth for Nov 30th, 1997. Shading indicates deepening of the isopycnals from shallow (black) to deeper layers (white).

increases from northern Peru to central Chile during Eastern Pacific El Niño events (see Fig. S9 in Conejero *et al.* 2020), similar to Espinoza-Morriberón et al. (2017) that found an increase in the surface EKE off the Peruvian coast during El Niño. While heightened PCUC transport and increased subsurface EKE during El Niño imply an uptick in subsurface eddy activity, the precise nature of this subsurface eddy modulation in response to ENSO remains uncertain. In this study, we used high-resolution reanalysis data and observations to investigate subsurface eddy characteristics and behaviour.

Our objectives are to (1) elucidate the spatio-temporal variability of subsurface eddy activities in response to ENSO, and (2) explore the underlying mechanisms driving these variations.

2. Data

2.1. Observation data

We used temperature and salinity data obtained from the Peruvian Sea Institute (IMARPE) (https://repositorio.imarpe.gob.pe), covering the period from 2015 to 2020. Observations were conducted at two fixed stations along the Peruvian coastline at Chicama station (7.8°S - 79.7°W) and Callao (12°S - 77.3°W), as shown in Fig. 1. Data were recorded at 1-meter intervals from the surface down to a depth of 100 meters. Sampling occurred at least twice a month with a maximum of 15 observations per month.

2.2. Reanalysis data

We used the 1/12° resolution GLORYS12V1 reanalysis dataset from the Copernicus Marine Environment Monitoring Service (CMEMS) (https://data.marine.copernicus.eu/products). This product (product ID: cmems_mod_glo_phy_my_0.083deg_P1D-m) provides daily data from January 1993 to December 2019, including zonal (u) and meridional (v) velocity components, temperature, and salinity at depths from the surface to 5728 m, and sea surface height data (Lellouche *et al.*, 2018). The dataset is based on the Nucleus for European Modelling of the Ocean (NEMO) model version 3.1 and incorporates data assimilation from in-situ and satellite observations, making it suitable for mesoscale ocean dynamics studies.

In this study, our focus is on the southern Peruvian coastal region (within 10°S-18.5°S and 70°W-84°W). However, we also explore the northern region (north of 10°S) for computing the phase speed of the coastal trapped waves. GLORYS12V1 data set reproduces well the observational data off Peru. We compared the temperature section at Chicama and Callao (Fig. 2), from where it can be seen almost the same patterns for the isopycnals of 25.5 and 26 (solid and dotted lines respectively), and intensity. For instance, during the first trimester of 2016 at Chicama, the isopycnal of 25.5 deepened significantly in both reanalysis and observations, to later became shallower at the end of 2016. Similarly, during early 2017, observational temperature increased, reaching values close to 28℃ and 21℃ at Chicama and Callao, respectively, that was well represented by reanalysis data in both stations. To statistically validate the reliability of the reanalysis data in representing well the observation, we used the annual and seasonal Taylor diagrams comparing density profiles from Chicama and Callao stations (Fig. 2). Annual reanalysis data shows very good agreement with the IMARPE observations (r_{callao}= 0.97 , $r_{chicama}$ = 0.99), with slightly higher variance than IMARPE (normalized standard deviation = 1.25) for both stations. Seasonal comparison showed the highest correlation during austral winter season at Callao station, and summer and autumn at Chicama station.

Furthermore, we define the surface layer as the layer within the upper 50 meters, while the subsurface layer is defined as the layer within isopycnals of σ_θ = 26–26.5 kg m^{-3}, this is to capture the subsurface eddies originated from the poleward Peru Chile Undercurrent which can be identified off Peru within the isopycnals of 25.5–26.5 (Rosales-Quintana et al. 2021), and to avoid influence from the surface. The locations of the observational and reanalysis data in this study are represented in a map in Fig. 1.

3. Methodology

3.1. Eddy kinetic energy

The eddy kinetic energy was computed separately for the surface and subsurface layers using Eq. (1).

$$\mathrm{EKE} = \frac{1}{2}\left(u'^2 + v'^2\right), \quad (1)$$

where u' and v' are fluctuating zonal and meridional velocity, respectively, calculated by subtracting the mean velocities throughout the record from instantaneous velocities. To accurately map the spatial pattern of subsurface EKE that is caused only by subsurface intensified eddies, we compute the subsurface EKE only when that exceeds the surface averaged EKE (hereafter as the "subsurface-intensified EKE"). This allows us to avoid averaging surface intensified EKE caused by surface eddies that penetrate deep into the subsurface layer. On the other hand, sur-

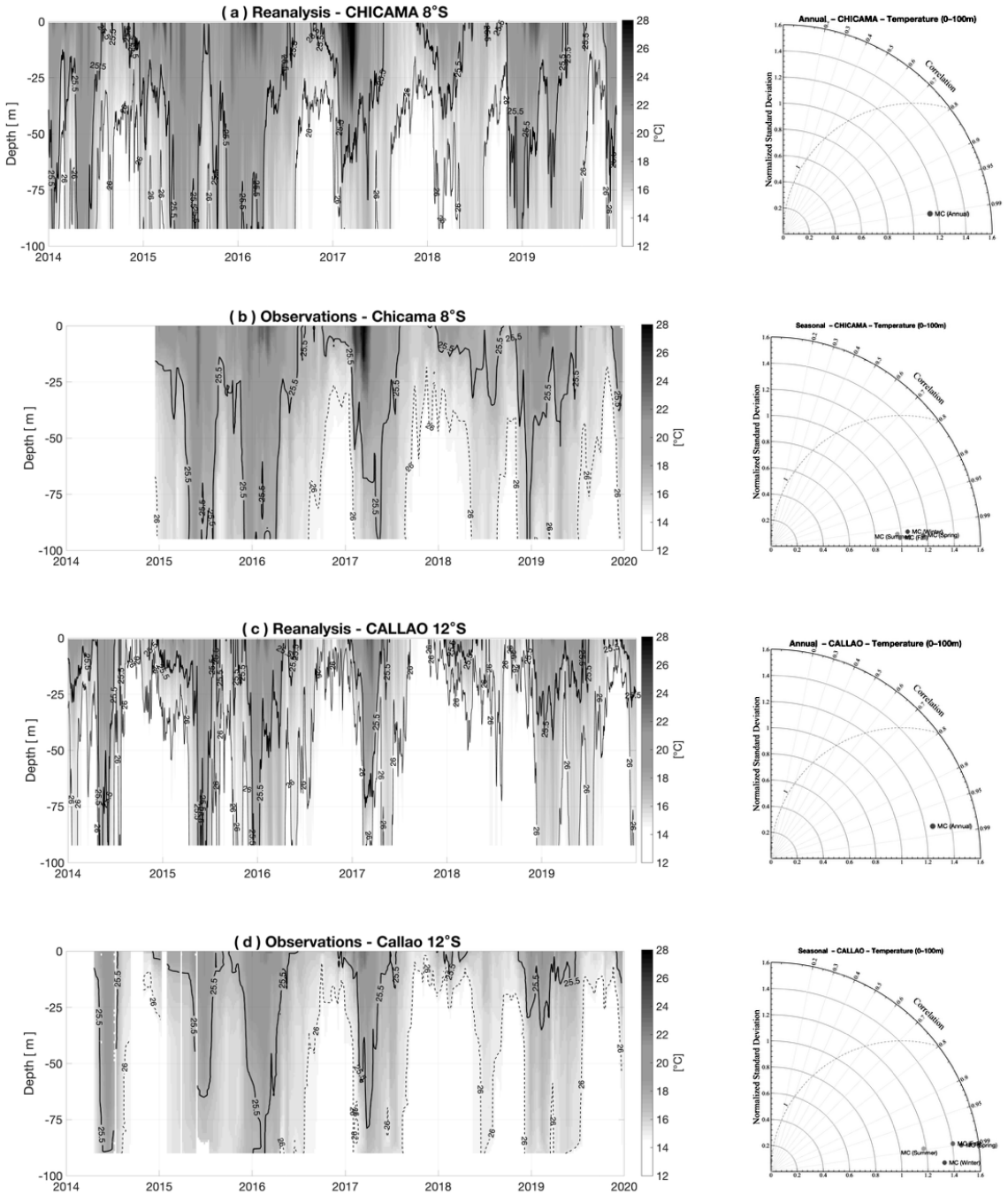

Fig. 2 Temperature section comparison for reanalysis and observations at (a,b) Chicama (8°S) and (c,d) Callao (12°S) stations from 2014 to 2019. Solid and dotted lines emphasize the isopycnals of 25.5 and 26.0 respectively. Reanalysis data is shown as daily samples, and observations with a maximum of 15 samples per month. Right column panels are the Taylor diagram for annual and seasonal comparisons between datasets.

face EKE is averaged within the top 50 m regardless of whether it is higher or lower than the subsurface layer, that is, surface EKE could also be affected by subsurface intensified eddies. To capture seasonal variations, EKE was averaged for austral summer (December to February), autumn (March to May), winter (June to August) and spring (September to November) over the period from 1993 to 2019. To investigate interannual variability, the monthly mean EKE was calculated over the same period.

3.2. Eddy identification and tracking

For eddy identification, we utilize the Okubo-Weiss (OW) parameter, defined as Eq. (2) which distinguishes rotating flows ($OW<0$) from the deformation regime ($OW>0$) (Okubo, 1970; Weiss, 1991), following a method similar to Nagai et al. (2015), previously applied for the California EBUS.

$$OW=4\left[\left(\frac{\partial u}{\partial x}\right)^2+\frac{\partial v}{\partial x}\frac{\partial u}{\partial y}\right], \quad (2)$$

where u and v are the zonal and meridional velocities, and x and y are the zonal and meridional coordinates. The eddy detection criteria involved searching for closed OW contours at -2×10^{-11} (s^{-2}). Cyclonic and anticyclonic eddies were distinguished according to the average vertical component of relative vorticity ζ within the detected eddy as in Eq. (3),

$$\zeta=\frac{\partial v}{\partial x}-\frac{\partial u}{\partial y}, \quad (3)$$

In the Southern Hemisphere, cyclonic eddies have $\zeta<0$, indicating clockwise rotation, whereas anticyclonic eddies have $\zeta>0$. Surface eddy detection used OW values averaged over the top 50 m, while subsurface eddy detection used OW values within σ_θ = 26–26.5 kg m^{-3}. Surface eddies were identified only when the absolute OW value averaged in the surface layer within an eddy is higher than that in the subsurface layer, while subsurface eddies are required to have both higher absolute OW values and relative vorticity within the subsurface density layer than that of the surface layer. The upper limit of the equivalent eddy radius, computed from the area within the eddy, is 200 km to extract mesoscale eddies. Also, to ensure that the detected features are true eddies and not filament-like structures, we employed a criterion for the aspect ratio (0.95–1.2). The eddies were then tracked by comparing the areas of the eddy shared between two consecutive time steps, retaining only those that lasted longer than 10 days. As mentioned in the Introduction, Puddies are originated from the PCUC. However, the eddy detection and tracking employed in the present study are not perfect to search the eddy origin. In some cases, detection fails due to the temporal evolutions of the eddies that prevent the continuous tracking, making it difficult to trace back the eddy origin. Furthermore, as the reanalysis is assimilated with the observation data, that do not necessarily capture the entire history of the subsurface eddies, the search for the origin of the subsurface eddy would be not feasible. On the other hand, our analyses for the subsurface layer are conducted within the density range σ_θ= 26–26.5 kg m^{-3}, which does not outcrop except very near the coast, excluding the possibility of the subsurface eddies caused by subduction processes. Accordingly, although our eddy detection and tracking have these limitations, we consider all the detected and tracked subsurface anticyclones as Puddies.

For each tracked eddy, the eddy non-linearity parameter is defined as the ratio of the swirl velocity U to the eddy propagation velocity c, U/c, which is obtained as averaged value based on our eddy tracking results for each layer (the same c = 0.034 m s^{-1} is found for each layer).

Where $U/c > 1$ suggests that the feature is nonlinear and maintains its coherent structure during their propagation (FLIERL, 1981) and capable of trapping matters inside and travelling with them.

3.3. Phase speed estimation

3.3.1. Vertical mode and speed of internal Kelvin wave for reanalysis data

To investigate the phase speed (C_p) of the internal Kelvin wave, linearized equations for along shore momentum, vertical momentum, density conservation, and continuity are combined into one equation for the vertical velocity.

$$\frac{\partial}{\partial t^2}\left(\frac{\partial^2 w}{\partial z^2}\right)+\left(\frac{\partial}{\partial t^2}+N^2\right)\frac{\partial^2 w}{\partial x^2}=0, \quad (4)$$

where $N^2=-g\left(d\bar{\rho}/dz\right)/\rho_o$ is the square of buoyancy frequency, g is the gravitational acceleration, with $\bar{\rho}$ (z) as the laterally averaged density and ρ_o as the constant density. Here, we assume flat bottom and coast as a vertical wall, no cross-shore velocity, considering the Boussinesq approximation. Assuming a following wave solution for vertical velocity w of variable separation type, $w=W(z)\sin(kx-\omega t)$, where k is along-shore wavenumer, ω is the frequency, and t is the time in Eq. (4), the vertical mode equation for the internal Kelvin wave induced vertical velocity can be obtained in the Sturm-Liouville system (Eq. (5)).

$$\frac{\partial^2 W}{\partial z^2}+\left(\frac{N^2-\omega^2}{c_p^2}\right)W=0 \quad (5)$$

Daily buoyancy frequency square N^2 along 450 m isobath as a function of depth, latitude and time is computed only during El Niño events. Then, the obtained buoyancy frequency is used to solve (Eq. (5)) for each water column numerically with arbitrary k as an input parameter and the boundary conditions for $W(z) = 0$ at the surface $z = 0$ and the bottom $z = 450$ m. The obtained eigenvalues, λ_i provide wave frequencies square ω^2, for each mode i. Therefore, wave phase speeds C_p for each mode i can be obtained by $\sqrt{\lambda_i}/k$. The eigenfunction represents a vertical structure of the vertical velocity.

3.3.2. Estimation using cross correlations for reanalysis data

To assess the meridional propagation characteristics, we estimated C_p along the 450 m isobath off the coast of Peru using the $\sigma_\theta = 26$ isopycnal depth fluctuations from 1993 to 2019. Specially, we focused on anomalous vertical displacements of the $\sigma_\theta = 26$ isopycnal during El Niño conditions across latitudes between 5°S to 19 °S, spaced approximately 2° apart. Before computing C_p, we first isolate time periods corresponding to El Niño events, then we remove the seasonal cycle and long-term trends by subtracting the monthly climatology and detrending the signal. A Butterworth bandpass filter (4^{th} order, 20–120 days passband) was applied to retain intraseasonal variability commonly associated with coastal trapped waves. After the preprocessing, we then compute a normalized cross-correlations between the filtered time series at a reference latitude (14°S) and all other selected latitudes. For each latitude pair, the lag corresponding to the maximum cross-correlation was identified and extracted. The spatial lag was computed based on the meridional distances between latitudes (assuming a spherical earth approximation). A linear regression was then performed between the lag in days (δt) and the spatial distance (δx), where the slope ($\eta = \delta t/\delta x$) represents the time delay per unit distance. The $\overline{C_p}$ was then computed as the reciprocal of this slope as, $\overline{C_p} = 1/\eta$, and converted to meter per second.

3.3.3. Estimation using the 1^{st} order polynomial fitting for reanalysis data

Since the reanalysis can provide data along the coast at every grid point, the speed of the

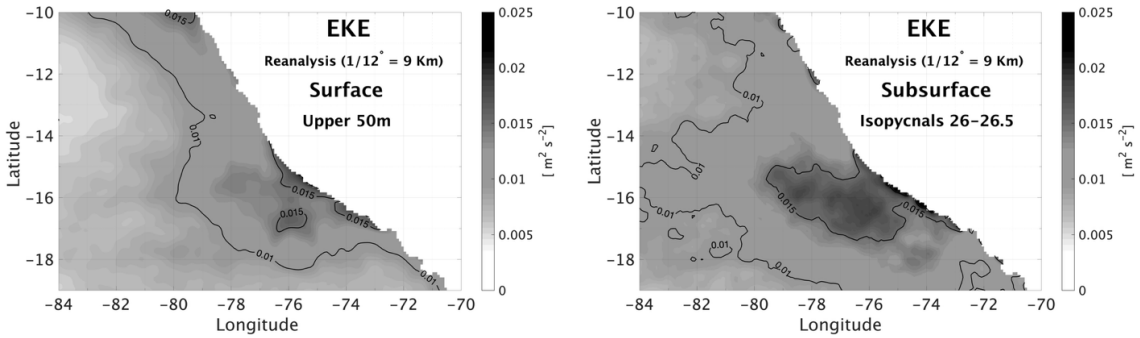

Fig. 3 Eddy kinetic energy (EKE) [$m^2\ s^{-2}$] spatial distribution averaged over the surface (0 to 50 m depth) and subsurface (σ_θ = 26–26.5 kg m^{-3}) layers for the period 1993–2019. The subsurface EKE values were included in the average only when they exceeded the surface EKE.

propagating signal can be estimated more directly than observation data at a few locations. Therefore, C_p was estimated by analysing alongshore transects of the σ_θ = 26 isopycnal depth anomalies derivate from reanalysis data during El Niño events. For each selected event, time-distance diagrams were constructed by plotting σ_θ= 26 isopycnal depth fluctuations as a function of distance along the Peruvian coastline and time, enabling the visualization of propagating internal signals. The peak detection was performed for the isopycnal depth. Peak points connected clearly that implied propagating signal, were manually extracted from the time-distance diagrams. Subsequently, a first-degree polynomial fit was applied to each segment of the selected peaks. The slope of the fitted line provided an estimate of the C_p. To capture spatial variability of C_p, the obtained C_p was bin-averaged as a function of latitude.

3.3.4. Estimation using coherence analysis for observational data set

For observational data in Chicama (7.8°S) and Callao (12°S) (IMARPE), we selected the period that has continuous approximately weekly data from 2015 through 2020 in 40–85 m depth, avoiding influences from the surface. To isolate propagating waves signals as previously applied to reanalysis data, we use a fourth-order Butterworth banpass filter to each time series, with a filter designed to retain variabilities within the period of 20–120 days to investigate coastal trapped Kelvin waves (Camayo and Campos, 2006; Dewitte et al., 2012; Belmadani et al., 2012; Poli et al., 2022). The phase lag, $\delta\theta$ was extracted in the frequency ranges where coherence square is higher than 0.15, which then used to compute time lags, δt by $-\delta\theta/(2\pi\omega)$. The phase speed C_p can be obtained by $\delta x/\delta t$, where δx is the great-circle distance between Chicama (7.8°S) and Callao (12°S).

4. Results

4.1. Eddy Kinetic Energy

Surface EKE exhibits large values within 200–300 km of the coast, with slightly elevated levels north of 12°S and very high values south of 14°S along the Peruvian coast, consistent with previous studies (Combes et al., 2015) (Fig. 3). In contrast, subsurface EKE shows a distinct spatial distribution, with higher values (≈ 0.02 $m^2\ s^{-2}$) concentrated in the southern part of the study area, and up to 0.025 $m^2\ s^{-2}$ restricted to the nearshore coastal area, between 14°S and 18

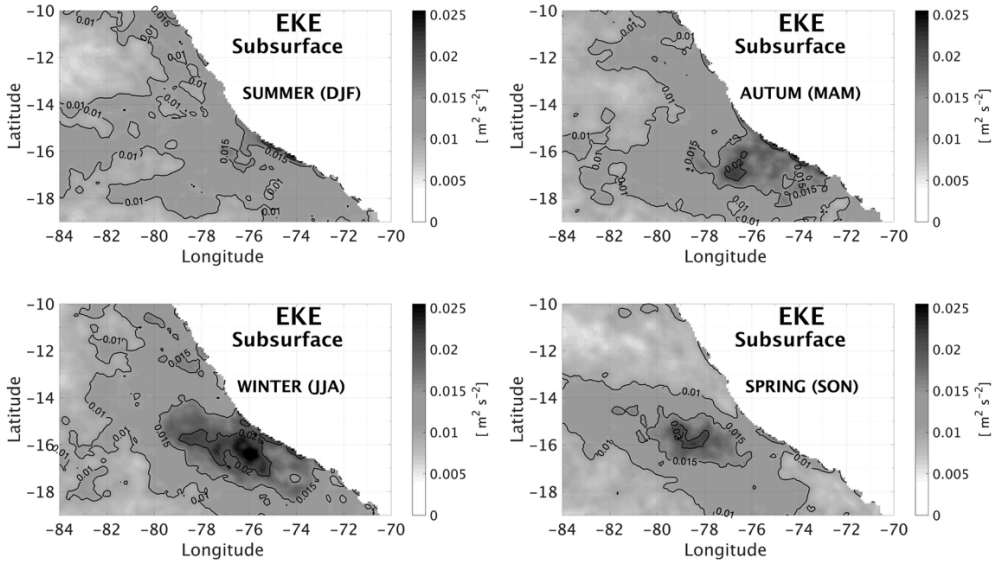

Fig. 4 Seasonal variability of the eddy kinetic energy (EKE) [$m^2\ s^{-2}$] averaged for the subsurface layer (within σ_θ = 26–26.5 kg m^{-3}) from 1993 to 2019. The subsurface EKE was averaged only when the EKE values were larger than that in the surface layer.

°S. This suggests that subsurface eddies are generated primarily in the southern region, compared to the surface eddies that can develop along the entire coastline. At the subsurface, high seasonal variability was found in the averaged EKE off the south coast of Peru. High EKE values are seen mainly during austral autumn, winter and spring with values higher than 0.02 $m^2\ s^{-2}$ that are concentrated south of 14°S (being winter the highest peak), while during austral summer, EKE showed its lowest values in the same region (Fig. 4). These changes in EKE seem to be synchronized with the seasonal variability of the PCUC, which intensifies from autumn to the beginning of winter. Flores et al. (2013) used the 15℃ isotherm depth as an indicator of the PCUC and its variability off Peru. They showed that when the PCUC intensifies, the 15℃ isotherm deepens up to 250 m during the austral autumn. In contrast, during the austral spring, the PCUC weakens, resulting in a shallower 15℃ isotherm. Such behaviour is similar to that observed in the equatorial Pacific, where the EUC strength is tightly linked to the thermocline depth variability (Kessler et al., 1995). Our eddy detection and tracking results (in section 3.2) align well with the EKE enhancement during the austral autumn and winter seasons, showing an increase in the number of detected subsurface eddies, particularly subsurface anticyclones, Puddies. This implies a strong link between the seasonal variability of the PCUC and the formations of the subsurface eddy.

4.2. Eddies detected off Peru

To better understand how the subsurface eddies modulate interannually and how they can be linked to EKE variations, we analysed 27 years of reanalysis data and used eddy detection and tracking techniques. Consistent with the findings of Combes et al. (2015), our results show that surface intensified cyclones (56%) are more

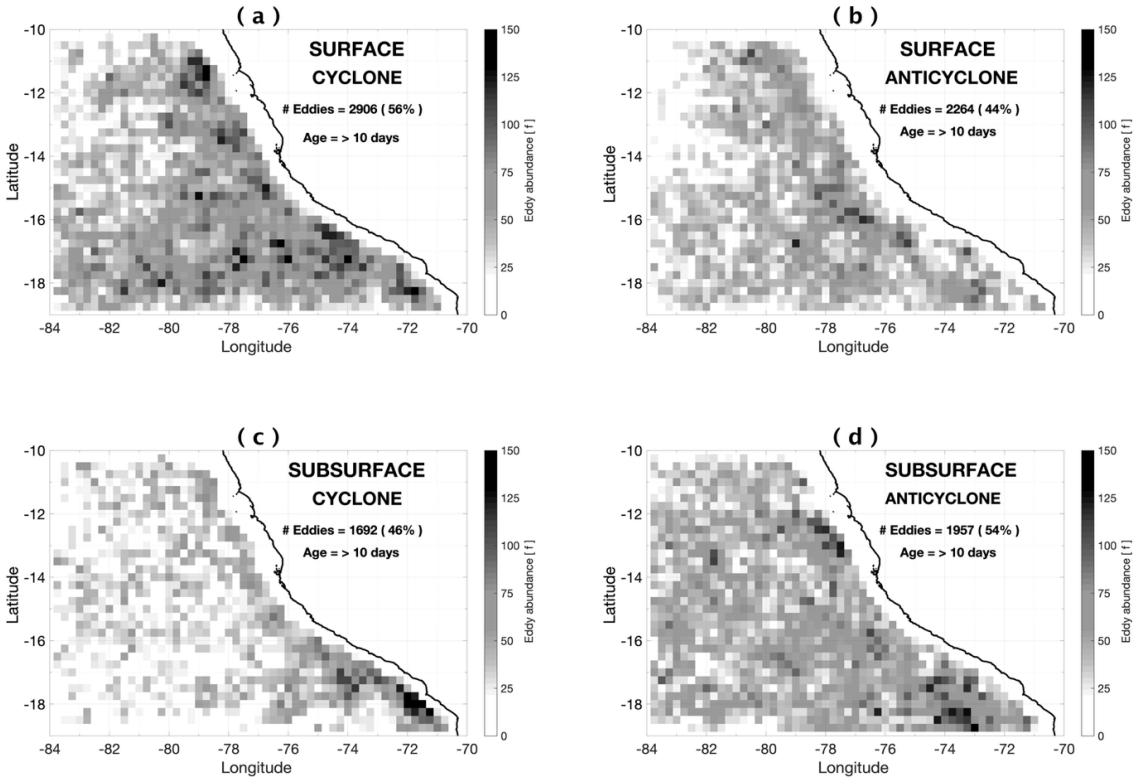

Fig. 5 Abundance of surface and subsurface detected and tracked eddies that lived longer than 10 days for (a) surface cyclones, (b) surface anticyclones, (c) subsurface cyclones and (d) subsurface anticyclones. For counting eddies, we consider the eddy that lasted longer than 10 days from the time it is born and followed it until it dies. We represent the cumulative count of daily eddy appearance for 27 years, within a grid cell of 0.25°× 0.25°. The eddies found offshore are most likely originated from the nearshore within the PCUC.

abundant than anticyclones (44%) in the surface layer. In contrast, subsurface anticyclones dominate the subsurface layer, accounting for 54% of all eddies (Fig. 5). The differences in the spatial distributions detected eddies between those in the surface layers (Fig. 5 a-b) and the subsurface layers (Fig. 5 c-d) are evident. In the surface layer, cyclones are distributed in the wide region from nearshore to the offshore up to 1,200 km from the coast especially in the southern region (16–18°S), while anticyclones are mostly concentrated within 100 -600 km from the coast. In the subsurface layer, cyclones are restricted to nearshore, predominantly south of 16° S, while anticyclonic eddies exhibited localized hotspots along the coast at 12°S - 14°S and south of 16°S. In addition to spatial distributions, subsurface-intensified eddies show distinct temporal patterns. Fig. 6 shows monthly statistics, revealing that subsurface anticyclonic eddies, Puddies, are more prevalent in austral autumn (April to May) with its highest peak in April (with around 150 Puddies), followed by a second peak during austral winter (July, with 135 Puddies, Fig. 6a). Subsurface cyclones follow a similar trend with peak occurrences in May and June. Both anticyclonic and cyclonic eddies shown a marked decline in activity during the austral

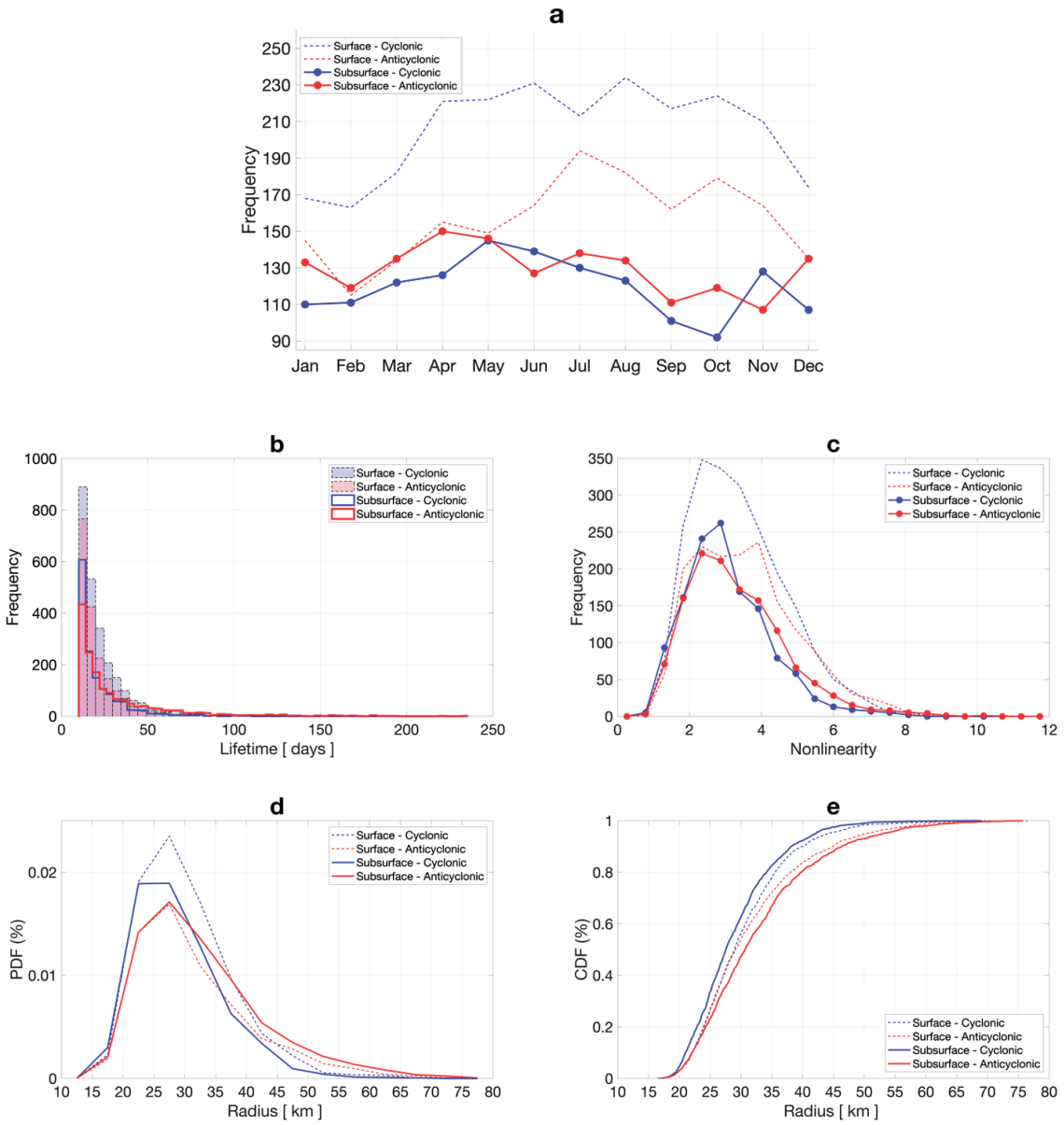

Fig. 6 Eddy statistics for detected and tracked eddies that lived longer than 10 days for (a) seasonality, (b) lifetime, (c) nonlinearity, (d) probability density function and (e) cumulative density function for radii.

spring, reaching their lowest abundance in October and November, respectively. Although the subsurface EKE shows its highest peak during winter season (Fig. 4), these subsurface eddy activities, intensified in autumn is consistent with the enhanced EKE in autumn, suggesting that subsurface eddy activities are highly consistent with the seasonal variability of PCUC (Vergara et al., 2016). Moreover, the numbers of subsurface cyclones and anticyclones increase

Table 1. Non-linearity parameter defined as the ratio of the swirl velocity U to the theoretical propagation velocity (c = 0.034 m s^{-1}) of the eddy. Where U/c>1 suggests nonlinearity, maintaining its coherent structure during their propagation.

Eddy type	U/c	Abundance %
Surface Cyclones	3.4	56
Surface Anticyclones	3.6	44
Subsurface Cyclones	3.1	46
Subsurface Anticyclones	3.3	54

during November and December, respectively. In contrast, surface-intensified eddies showed their highest abundance mostly during austral autumn to spring (April-October).

Another notable contrast between subsurface cyclones and anticyclones is that the latter tends to have longer lifespans (Fig. 6b); some subsurface anticyclonic eddies persist for up to 245 days, while cyclones have a maximum duration of 110 days. Most subsurface eddies have radii between 25 and 30 km (Fig. 6d) with anticyclones tending to be larger than cyclones; 66% of anticyclones have radii below 35 km, while it is as high as 83% for cyclones (Fig. 6e). Moreover, we found that both surface and subsurface eddies exhibited high non-linearity (Fig. 6c), allowing them to trap and transport matter. Our results showed that surface-intensified cyclones (U/c = 3.4) and anticyclones (U/c = 3.6) have on average higher non-linearity than subsurface eddies, which showed U/c = 3.1 for cyclones and U/c = 3.3 for anticyclones. The mean non-linearity for subsurface eddies ($\overline{U/c}$ = 3.2) is found to be statistically different with a 5% significance level from that for the surface one ($\overline{U/c}$ = 3.5), indicating that subsurface eddies are slightly leakier than surface eddies (See Table 1).

4.3. σ_θ= 26 isopycnal depth variability

To examine how differently El Niño events influence the subsurface eddy abundance off Peru, we utilize the σ_θ= 26 isopycnal depth variability as a proxy for changes in the upper limit of the PCUC. The σ_θ = 26 isopycnal depth tends to deepen during warm events, with greater southward penetration along the coast. ENSO events are commonly defined by the averaged sea surface temperature anomaly (SST) along the Equatorial Pacific at the Niños areas such as Niño 3.4 (5° N-5°S, 170°W-120°W) and Niño 1 + 2 (0°-10°S, 90°W-80°W). The latter region is particularly relevant for the South American coast. The two bottom panels of Fig. 7 show the SST anomaly for Niño3.4 and Niño 1 + 2 from 1993 to 2019, highlighting the El Niño events defined by the threshold of ± 0.5, following the definition of Oceanic El Niño index (ONI) and Coastal El Niño index (ICEN). A recent work by BERTRAND et al. (2020) has further categorized ENSO phases beyond the canonical El Niño 3.4 definition, considering the intensity of rainfall/dry conditions, and zonal location of the warm pool, which has been used in this study to define El Niño type.

During extreme (Ex) El Niño events, such as those of 1997–1998 and 2015–2016, SST anomalies in Niño 1 + 2 rose to about + 4℃, while Niño

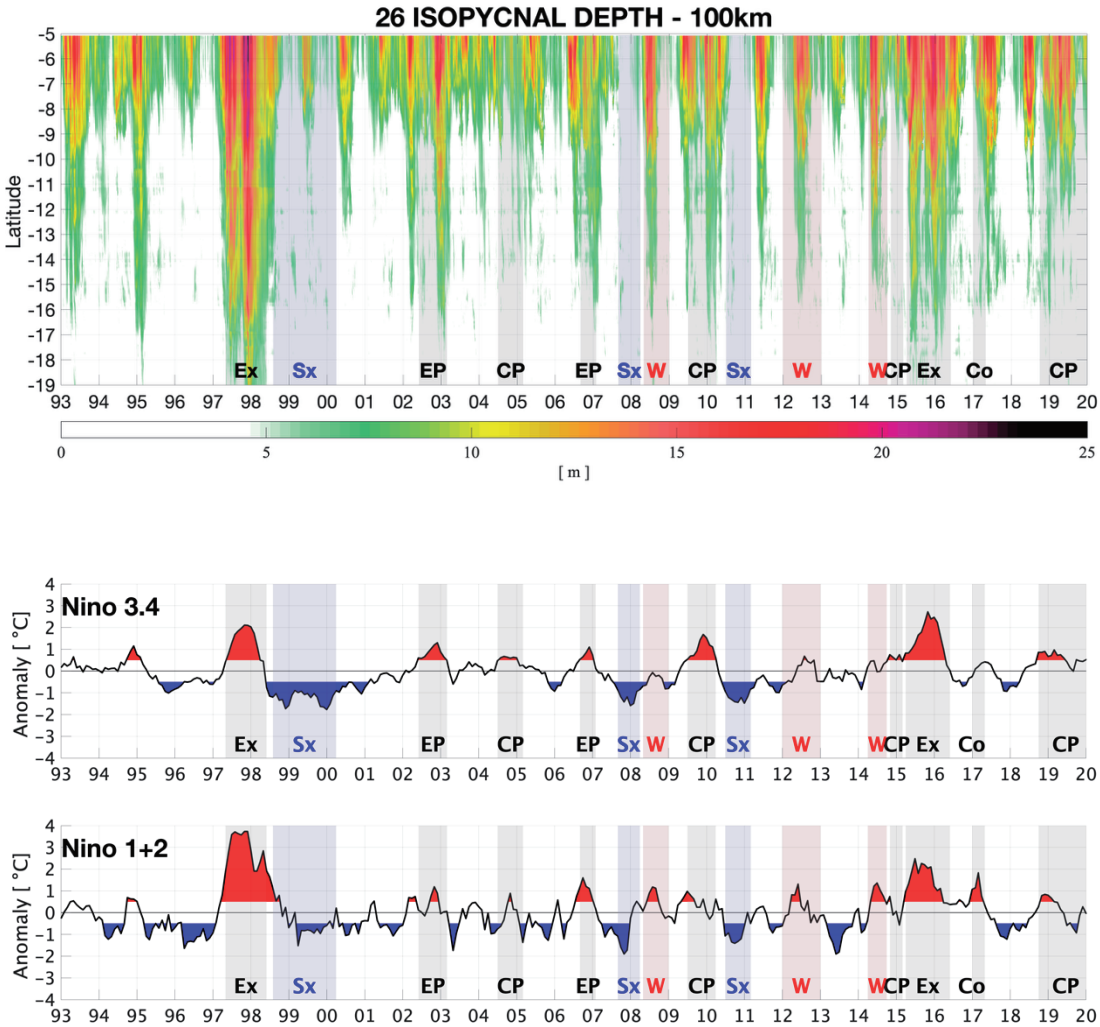

Fig. 7 Monthly averaged σ_θ= 26 isopycnal depth [m] for the 100 km distance from the coast, from reanalysis data is shown in the top panel. Shaded areas indicate ENSO phases as follow; Extreme El Niño (Ex), Eastern Pacific El Niño (EP), Central Pacific El Niño (CP), Coastal El Niño (Co), Strong La Niña (Sx), and moderately warm periods (W). Threshold of ± 0.5 is indicated with red and blue for both (middle) Nino 3.4 and (bottom) 1 + 2 indices.

3.4 anomalies reached ≈ + 2.5 ℃, corresponding to a markedly increased number of subsurface anticyclonic eddies (Puddies), as described later in section 4.5. The isopycnal depth also deepened significantly across latitudes, reaching up to 25 m of its amplitude during 1997–1998 (Fig. 7). Although both events are classified as extreme, they differed somewhat. The 1997–1998 event produced a uniform deepening of the σ_θ= 26 isopycnal from 5°S to 19°S, while the 2015–2016 event caused a more prolonged and pronounced deepening primarily in the northern latitudes (5 °S to 12°S). This distinction may be partly attributed to the anomalously warm conditions pre-

ceding the 2015–2016 event (the Central Pacific El Niño 2014–2015) and to long-term background warming (SANTOSO et al., 2017).

During two eastern Pacific (EP) El Niños (e.g. 2002–2003, 2006–2007), moderate isopycnal deepening compared to extreme events are seen, with Niño 3.4 and Niño 1 + 2 anomalies generally ranging between + 0.5℃ and + 2℃. Comparing these events, the σ_θ= 26 isopycnal depth showed more pronounced deepening during 2002–2003, with a meridional extension up to 14°S (> 10 m of isopycnal deepening), while the 2006–2007 event showed a more localized deepening concentrated in the northernmost region (reaching only up to 10°S). Central Pacific El Niños (CP), such as 2004–2005, 2009–2010 and 2014–2015, primarily affect the central equatorial Pacific and inducing weaker and more localized changes in isopycnal depth along the Peruvian coast. Previous studies pointed out that CP events are less related to the thermocline variations and that their variability might be more influenced by atmospheric forcing (KAO and YU, 2009; SANTOSO et al., 2017). On the other hand, Ex and EP events are associated with basin-wide thermocline and wind variations. The σ_θ= 26 isopycnal in Fig 7 showed a very weak deepening during CP 2004–2005 and 2014–2015 with values between 5–13 m, that is different from CP 2009–2010 with deeper variability (up to 20 m of isopycnal deepening) limited to the northernmost region. Coastal El Niño (Co) events, exemplified by the 2017 event, caused a very short in time and highly localized isopycnal deepening of ~15 m near the northern Peruvian coast (5°S to 8°S). These events, unique to the Peruvian upwelling system, are driven by regional atmospheric and oceanic processes rather than basin-wide conditions, with impacts confined to the nearshore regions (RAMÍREZ and BRIONES, 2017). We also defined moderately warm (W) periods (i.e., 2008–2009 2012–2013, early 2014) marked by positive SST anomalies in Niño 1 + 2 (Fig. 7), although they never fully developed into classical El Niño conditions (SU et al., 2014), nor classified as El Niño events, these warm periods still appear to influence the isopycnal depth and likely contribute to increased subsurface eddy formation. Strong La Niña (Sx) events (1999–2000, 2007–2008, 2010–2011) lead to significant shoaling of the isopycnal (Fig. 7) and are associated with enhanced upwelling, cooler subsurface waters, and increased productivity along the coast. During these extremely cold periods, we observed a corresponding negative trend in subsurface eddy formation as described in section 4.5.

4.4. Interannual variability of EKE

We previously demonstrated that changes in the depth of the σ_θ= 26 isopycnal are synchronized with the onset of warm events. We now explore whether this relationship also appears in the eddy kinetic energy (EKE). The average EKE within the first 100 km from the coast (Fig. 8) showed pronounced meridional variability, with elevated values observed primarily in two latitudinal bands: from 5°S to 11°S, and from 14°S to 18°S, in both the surface and subsurface layers. Over time, changes in EKE correspond well to the deepening of the σ_θ= 26 isopycnal. At the surface, EKE notably intensifies during the two extreme El Niño events (Ex) 1997–1998 and 2015–2016. In Ex 1997–1998, enhanced EKE was widespread throughout the entire meridional range, while in Ex 2015–2016 the increases were pronounced over time but concentrated in the region north of 11°S. On the other hand, EP events showed moderate EKE confined to the northernmost region (2006–2007) or spread separately within the northernmost and southernmost regions (2002–2003). But for the subsur-

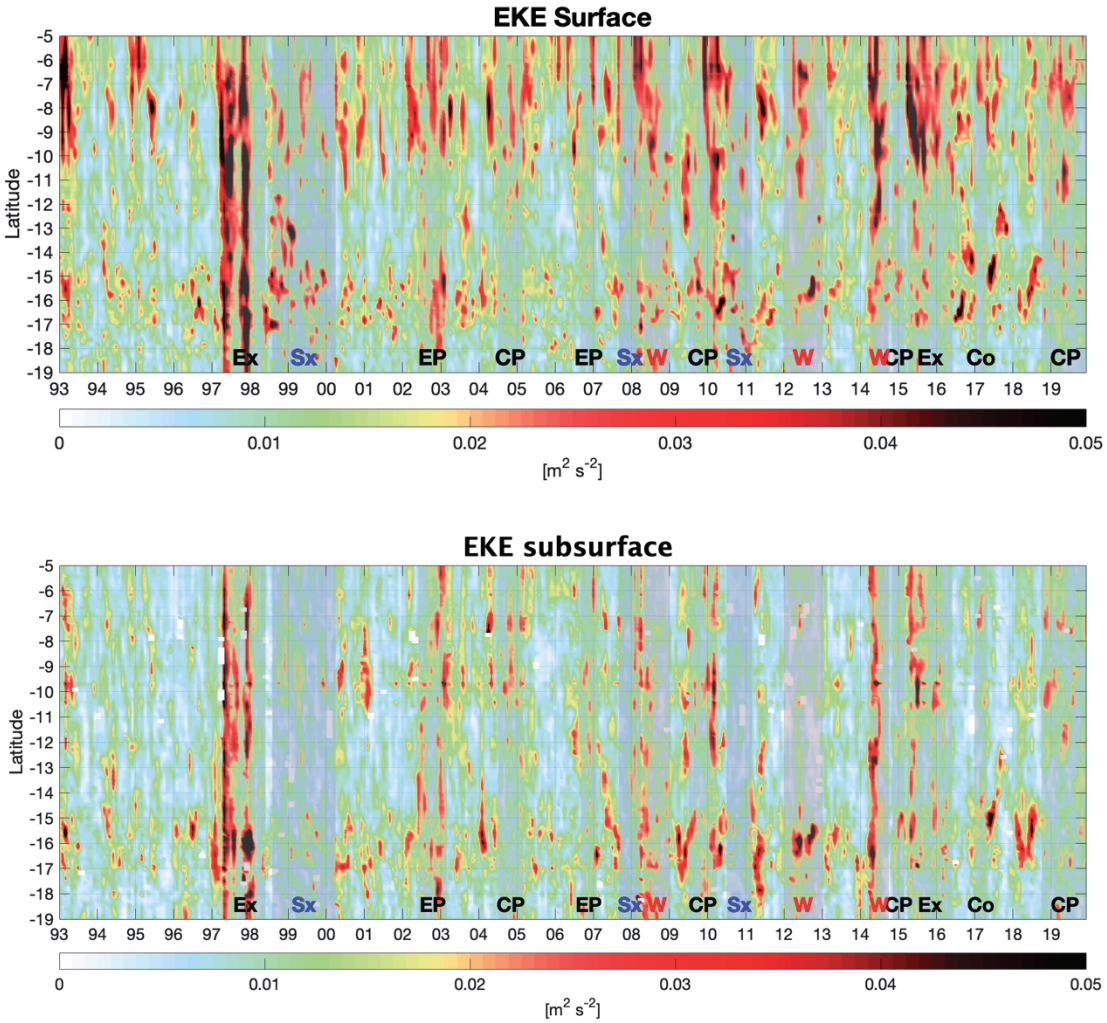

Fig. 8 Spatial-temporal variability of the monthly averaged eddy kinetic energy (EKE) [$m^2 s^{-2}$], for the surface (upper 50 m depth) and subsurface (within σ_θ= 26–26.5 isopycnal) layers within the first 100 km from the coast. EKE varies along latitudes from 5°S to 19°S, and years from 1993 to 2019. Shaded areas indicate ENSO phases as follow; Extreme El Niño (Ex), Eastern Pacific El Niño (EP), Central Pacific El Niño (CP), Coastal El Niño (Co), Strong La Niña (Sx), and moderately warm periods (W).

face layer, EP events exhibit much less EKE of 0.03 - 0.04 $m^2 s^{-2}$ than that in the surface layer. Even if the EKE increases, it is rather patchy and limited to the southernmost region, south of 14°S. EKE during Central Pacific El Niños (CP) were mainly enhanced in the surface layer and restricted to the northernmost region, while CP events did not show a clear enhanced EKE in the subsurface layer. We define moderately warm periods (W) in which temperature ranges ± 0.5℃, such as 2008–2009, 2012 and 2014, that were also characterized by elevated EKE restricted mostly to the northernmost region at the surface layer, and to the southernmost re-

gion at the subsurface layer (south of 14°S), expect for 2014 that showed continuous enhancement in EKE along the entire region from 5°S to 19°S. The 2017 Coastal El Niño (Co), showed similarly enhanced EKE in the surface and subsurface layers, which was, however, not as strong as the other warm events (i.e. Ex, EP and W events) and limited to the region between 5°S to 8°S for both layers. On the other hand, strong La Niña (Sx) events were marked by very low subsurface EKE, deviating from the patterns observed in the surface layer where EKE did not completely vanish. The EKE variations during strong La Niña (Sx) events are consistent with a negative trend in the number of subsurface eddies detected during the same events (as described in section 4.5).

These results imply that the formation of subsurface eddies is more vigorous during most types of the El Niño, and they are highly weakened during La Niña events, suggesting that ENSO-related variability is likely to exert a strong influence on subsurface eddy activities off Peru.

4.5. Interannual variability of the eddies detected off Peru

We have shown that the σ_θ = 26 isopycnal depth and subsurface EKE increased during warm events. Here, we examine whether this was reflected in the number of eddies detected in the subsurface layer and compare that to the surface counterpart (Fig 9). The surface and subsurface eddies detected and tracked off Peru exhibited substantial interannual variations that would be influenced by ENSO events. During Ex 1997–1998 and 2015–2016, numbers of tracked subsurface anticyclonic eddies, Puddies, showed marked increases with up to 6 eddies generated per month (Fig. 9b), while, for the latter Ex event, the number of subsurface cyclones were also increased as much as subsurface anticyclones. In the surface layer, the number of anticyclones were always lower than cyclones (Fig 9a). During EP 2002–2003 and 2006–2007 events, the number of subsurface eddies especially subsurface anticyclones showed a decreasing tendency, leading to more abundant subsurface cyclonic eddies than subsurface anticyclonic eddies. Differently, during CP events, the number of subsurface anticyclones was always higher than cyclones, except for CP 2009–2010 where the number of subsurface anticyclones showed a peak but with decreasing tendency. On the other hand, in the surface layer, cyclones surpassed anticyclones during all CP events. During Co 2017 event, subsurface eddies, both cyclones and anticyclones showed peaks of up to 7 eddies for a month, that are different from the surface eddies. Moderate warm periods (W) persistently showed elevated number of subsurface eddies, with the highest peak in 2008–2009 event in both layers. In the surface layer, W events exhibited higher number of eddies during 2008–2009 and 2014–2015 (Fig. 9a). During strong La Niña (Sx) events (1999–2000, 2007–2008, 2010–2011), the number of subsurface eddies exhibited a decreasing tendency compared to the previous year especially for subsurface anticyclones. Within Sx events, the tendency shows decreasing number of subsurface anticyclones followed by an increase near the end of the events with the highest increase happened during 2007–2008.

A scatter plot between averaged isopycnal depth at σ_θ = 26 from 10–19°S and numbers of subsurface eddies suggests that the abundance of subsurface eddies (both cyclones and anticyclones) showed weak statistically significant positive correlations with the isopycnal depth ($r = 0.17$, $r = 0.26$, respectively, p-value < 0.05, in Fig 10), while the correlations are statistically not-

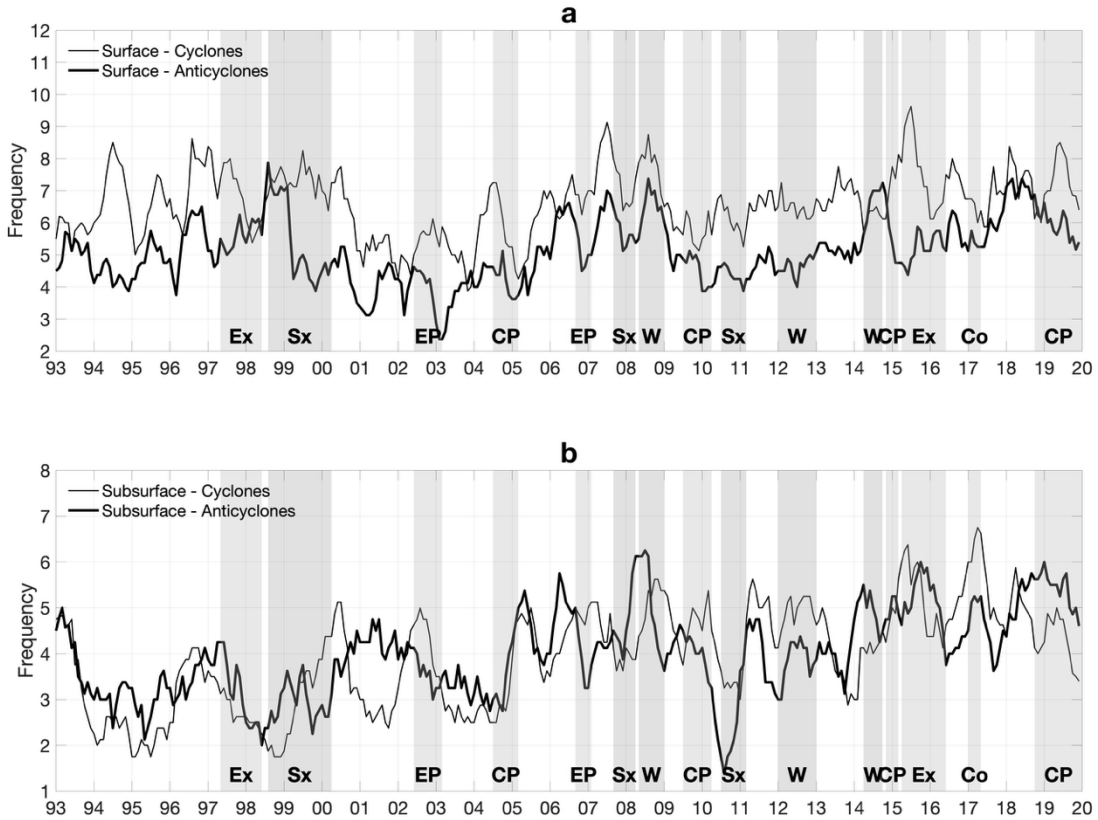

Fig. 9 Interannual variability of the number of eddies detected and tracked during 1993 to 2019 off Peru at both surface (a) and subsurface (b) layers. Shaded areas indicate ENSO phases as follows; Extreme El Niño (Ex), Eastern Pacific El Niño (EP), Central Pacific El Niño (CP), Coastal El Niño (Co), Strong La Niña (Sx), and moderately warm periods (W). Note that y-axis for the number of eddies differ for each layer. For both panels, "frequency" refers to the number of eddies born within a month, counting those eddies that lived at least 10 days (e.g. Eddy1 was born in day 1 and lived 30 days in total, then this eddy is count as "1" for this birth month).

significant for surface eddies. This indicates that when the isopycnal deepens, it appears to have influence on the formation of subsurface eddies.

In the surface layer, cyclones dominate almost constantly over anticyclones (Fig. 9a). However, the trend of number of cyclone and anticyclones does not always synchronize. During the EP of 2002–2003, cyclones exhibited a small peak, while anticyclones decreased, demonstrating an opposite trend. After these events, surface-layer cyclones and anticyclones generally showed similar tendencies over the years. Furthermore, in both the surface and subsurface layer, we identified a positive trend between 1993 and 2019 in the number of eddies detected, which could be due to global warming, as Conejero et al. (2020) suggested by using EKE in the surface layer. However, since this topic is beyond the scope of this study, we will leave it for future investigation.

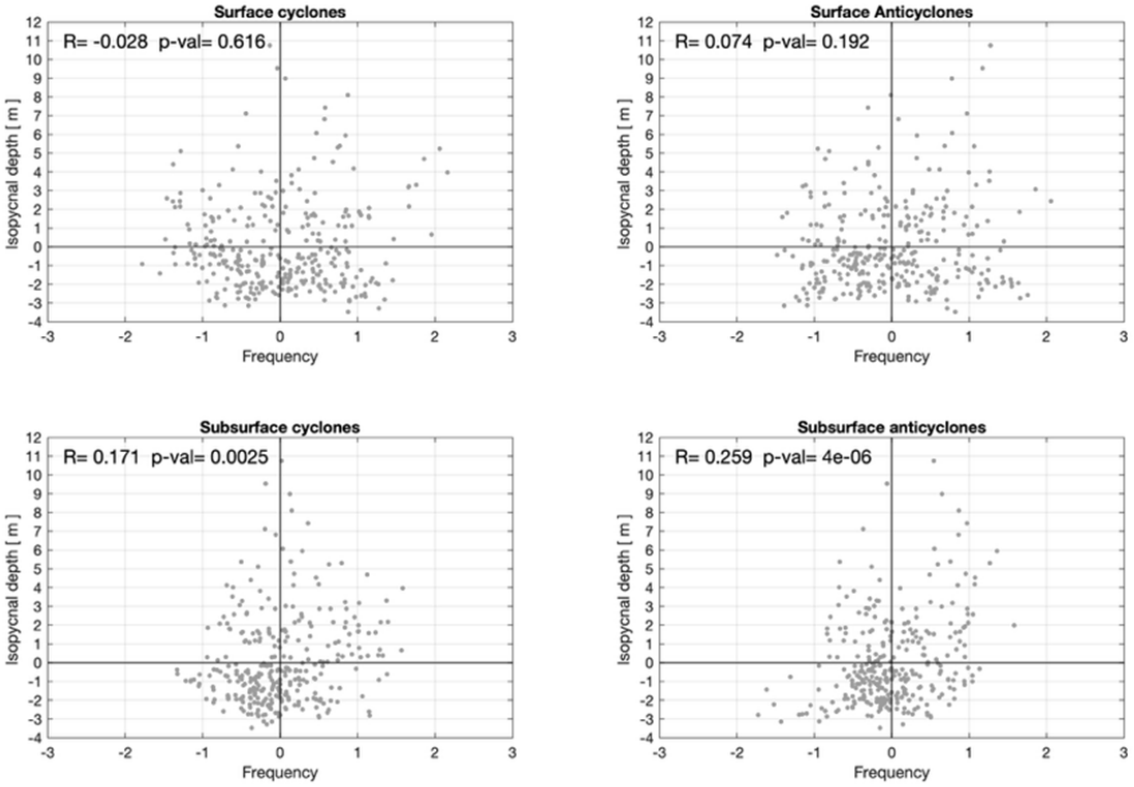

Fig. 10 Relationship between σ_θ= 26 - isopycnal depth［m］and eddy frequency（number of eddies born in a month）for surface and subsurface cyclones and anticyclones detected between from 1993 to 2019 within the southernmost region 10°S to 19°S are shown. A running-mean of 5 months was applied to both variables. Correlation coefficient（R）and significance（p-value）are also shown.

4.6. Coastal trapped wave propagation

Isopycnal depth along the Peruvian coast clearly responded to ENSO variability and other warm events. To further address these patterns, we investigate the possibilities of the poleward propagating coastal trapped waves by estimating the speed of the propagation, C_p in the study region using several methods. The C_p of the first baroclinic mode was estimated by solving the vertical mode equation (5) during El Niños events along the 450−m isobath (5°S-19°S) in Fig. 11. The results show distinct latitudinal variability in C_p, with notably slower propagation in the southernmost region, south of 16°S. During most of the El Niño events, C_p usually shows poleward phase speeds larger than 0.8 ms^{-1}, with a maximum C_p during Ex 1997−1998 event (1.7 ms^{-1} Fig. 11a). On average, C_p ranged between 0.6 to 1 ms^{-1} (0.95 ms^{-1} overall, Fig. 11b) along the coast, with a general decreasing trend towards higher latitudes. The eigenfunction solution as a function of latitude and σ_θ (Fig. 11c) showed maximum amplitude near σ_θ = 26 kgm^{-3}, suggesting that our choice of the isopycnal to detect the propagation was reasonable although the maximum amplitude shifts denser layer southward. The strong latitudinal dependence suggests significant regional differences in baroclinic wave dynamics during El Niño years. We compared these results with the estimates of C_p

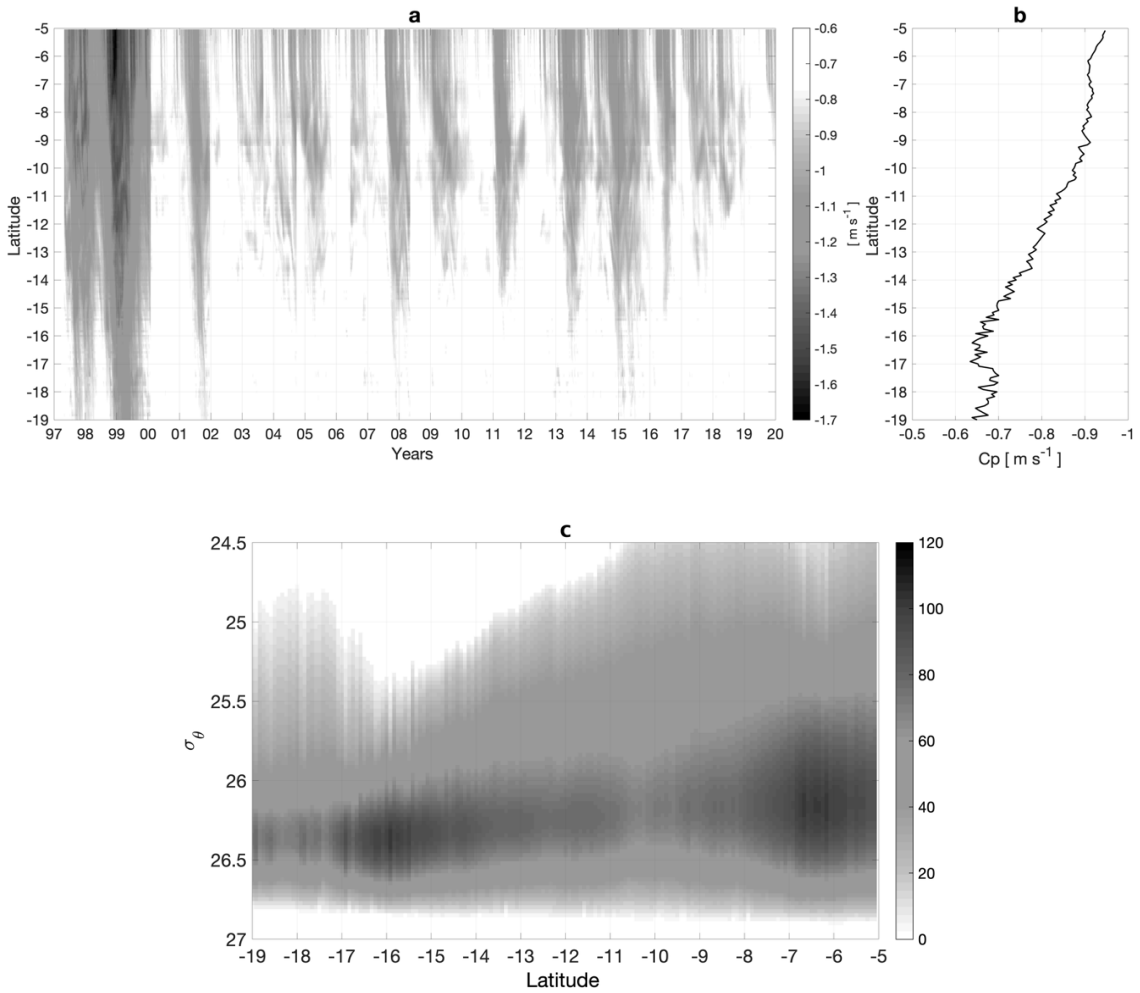

Fig. 11 (a) Phase speed (C_p) calculated from the first baroclinic mode between 1993 to 2019 and the (b) averaged C_p [ms^{-1}] across latitudes. (c) Eigenfunction of the first baroclinic mode for vertical velocity as function of density.

using the cross-correlation analysis and the 1st order polynomial least square fitting to the peaks in isopycnal deepening only during El Niño events. The obtained C_p are consistent values to the modal analysis also with the same decreasing trend for higher latitudes. Overall C_p calculated from cross-correlations resulted in 1.2 ms^{-1}, while C_p ranged between 0.5 ms^{-1} to 0.83 ms^{-1} (from south to north off Peru, Fig. 12 b) when using the 1st order polynomial least square fitting.

For observational data, coherence analysis of the band-passed anomalies of the 40–85 m-averaged σ_θ at Chicama (7.8°S) and Callao (12°S) during 2015 through 2020 in which relatively continuous data are available, revealed two distinct peaks in coherence square accompanied by positive phase lag (Fig. 13). The highest coherence peak corresponds to the fluctuation period

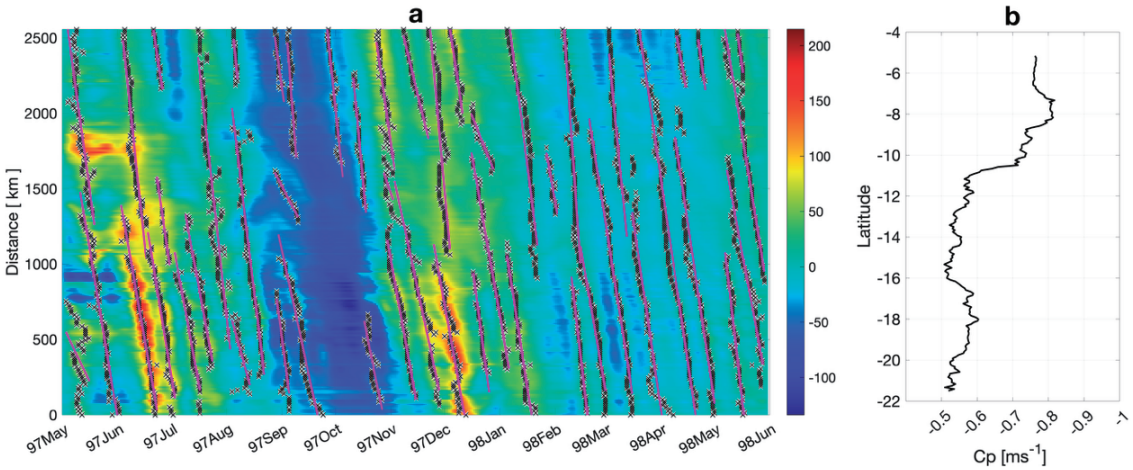

Fig. 12 Phase speed (C_p) calculated from alongshore transects for reanalysis data. (a) Point-by-point extracted data within the σ_θ= 26 isopycnal depth anomalies, for the Ex 1997–1998 event. (b) Averaged C_p [ms^{-1}] for all El Niño events (1997–1998, 2002–2003, 2008–2009, 2012–2013, 2014, 2015–2016, 2017, where Niño 1 + 2 >+ 0.5 anomaly)

of 50–56 days and the second highest peak to 30–32 days. The time lags for these two peaks were estimated as 1–5 days and 11–12 days respectively, that correspond to mean phase speeds at 1.85 and 0.53 ms^{-1}, respectively. Averaging phase speeds for those exceeds a coherence squire value 0.15, the mean phase speed is obtained as 0.87 ms^{-1}, which is consistent with the phase speeds estimated with many different methods for reanalysis data.

5. Discussions

Using a 27-year high-resolution reanalysis dataset, we detected and tracked eddies, including Puddies, in the Peru-Chile eastern boundary upwelling system. Previous studies have emphasized the dominant subsurface anticyclonic eddies over cyclones in the subsurface layer. The aim of this study is to document the main characteristics of surface and subsurface eddies, analyse their spatial temporal variability, and identify a possible link to the ENSO variability.

Eddy detection and tracking analysis revealed that subsurface-intensified anticyclonic eddies (54%) are more prevalent than cyclones, and that the former increase during warmer conditions and extreme warming events such as El Niño. We found a higher number of subsurface-intensified anticyclonic eddies (Puddies) compared to subsurface-intensified cyclones during extreme El Niño events in 1997–1998 and 2015–2016, as well as in other moderately warm years (2008, 2012 and 2014).

In contrast to the findings of Combes et al. (2015), who reported an inverse relationship between the volume of subsurface eddies and the 250-day-lagged Niño 3. 4 index for the entire Peru-Chile EBUS, our results suggest that subsurface anticyclonic eddies -Puddies- increase during El Niño and warm events. This discrepancy may reflect regional differences within the EBUS. Our conclusion is supported by the increase in EKE in the subsurface layer within the first 100 km from the coast during warm events. Similarly, Conejero et al. (2020) reported enhanced surface EKE off Peru during El Niño

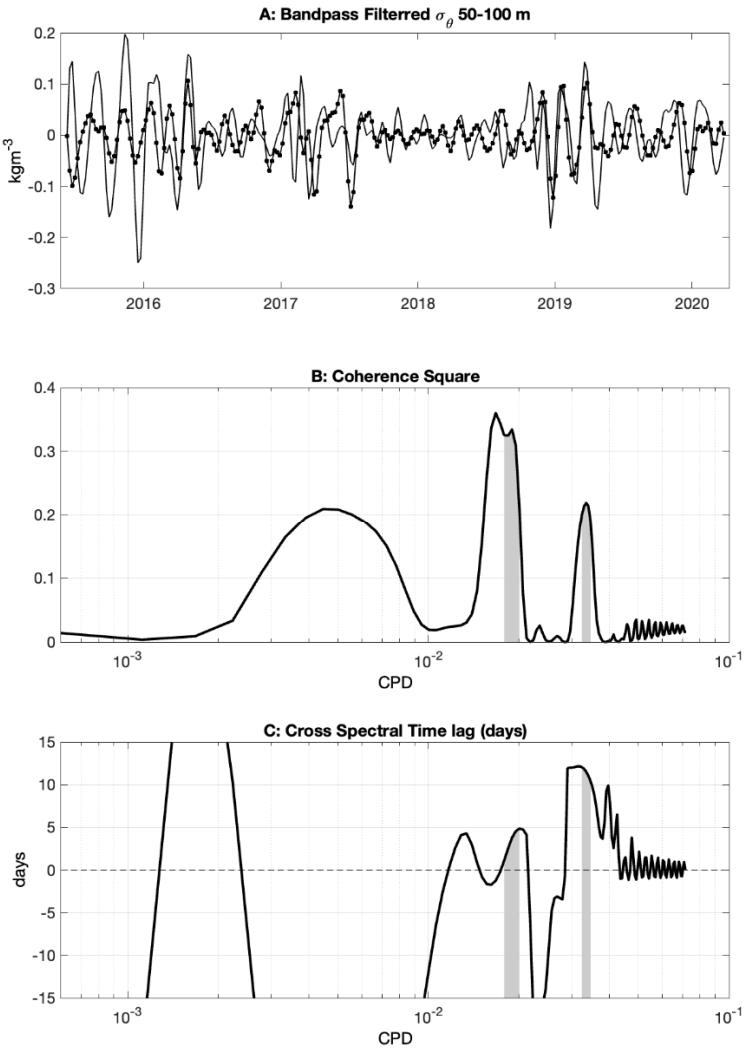

Fig. 13 Coherent analysis for observation at Chicama (7.8°S) and Callao (12°S). (a) Time series of bandpass filtered (20–120 days) 40–85 m-average σ_θ for (solid line) Chicama (7.8°S) and (dotted line) Callao (12°S) from 2015 through 2020. (b) Coherence square spectra of two time series shown in (a). (c) Spectrum of the time lag (days) with positive values indicating Chicama leads Callao. Grey shaded regions indicate the frequency bands that exceed a coherence squire value 0.15 in (b) and (c).

events. They also pointed out that EKE off Peru and Chile respond differently to El Niño, with EKE increasing off Peru and decreasing off Chile. This underscores the need to consider these regions separately when investigating ENSO-related variability. HORMAZABAL et al. (2004), using in-situ mooring data off the Chilean coast (30°S), found an inverse relationship be-

tween EKE and the Niño 3.4 index during 1997–1998, whereas CHAIGNEAU et al. (2008) reported enhanced EKE off Peru during the same period, consistent with CONEJERO et al. (2020) and our results.

However, it should be noted that the increase in the number of tracked subsurface anticyclonic eddies is not proportional to the amplitude of warm events, although the warm events tend to be associated with relatively large numbers of subsurface anticyclonic eddies. For example, the most extreme warming during 1997–1998 did not yield the greatest number of subsurface anticyclonic eddies. This reflects on the positive but low correlation found between the number of subsurface eddies and the isopycnal depth. Instead, we found strong correspondences between the Niño index, EKE, and isopycnal depth variations. One possible explanation is that, in addition to the ENSO variability, local wind curl modulates the PCUC and the formation of Puddies. Another factor could be a limitation in the eddy detection and tracking, which may not perfectly capture all the eddies. Additionally, the decay of the coastal trapped Kelvin wave may differ from one event to another, which may vary the eddy dynamics in complex ways (DEWITTE et al., 2012; HORMAZABAL et al., 2004; CZESCHEL et al., 2018).

Previous studies (CAMAYO and CAMPOS, 2006; BELMADANI et al., 2012) have shown that coastal trapped Kelvin waves in northern Peru propagate with periods of 80–120 days and that their periods can change as they interact with topographic features while traveling poleward. Some waves radiate Rossby waves, while others interact with the mesoscale eddies. Here, applying the coherence analysis for observation data from 2015 to 2020, we found that the subsurface density fluctuations with periods of 50–56 and 30–32 days translate poleward from Chicama through Callao with a speed C_p at 1.85 and 0.53 ms^{-1}, respectively. Averaging speeds for the data with coherence square higher than 0.15 and positive phases, the average phase speed is found to be 0.87 ms^{-1}. We also estimated C_p of the coastal trapped waves for the reanalysis data with a longer period (1993–2019) and higher spatial resolution. Using the cross-correlation analysis for isopycnal depth at σ_θ = 26 kgm^{-3} along 450 m isobath off Peru, the mean C_p is found to be 1.2 ms^{-1}, while C_p ranged from 0.5 ms^{-1} to 0.83 ms^{-1} with a poleward decreasing trend. These poleward phase speeds are in good agreement with the theoretical speeds for the first baroclinic mode internal Kelvin wave during El Niño events obtained by solving the vertical mode equation along 450 m isobath for their magnitude and a poleward decreasing trend (CAMAYO and CAMPOS, 2006; BELMADANI et al., 2012; ECHEVIN et al., 2014).

Our analyses performed separately for surface and subsurface eddies, revealed distinct differences in their spatiotemporal distribution and associated characteristics. Surface eddies were found to be predominantly cyclonic (56%), with anticyclonic eddies accounting for the remaining 44%. Both types exhibited pronounced seasonal variability, with their highest occurrence from middle austral autumn, winter and early spring, and a marked decline later in the biggening of austral summer. On the other hand, subsurface anticyclones (54%) were found to dominate over cyclones (46%), with a marked seasonal pattern, peaking in abundance during the austral autumn (April) followed by austral winter season, and reaching their lowest numbers in the spring. The observed seasonality in surface eddy abundance is likely driven by intensified upwelling associated with seasonally varying winds patterns, while subsurface eddies appear to form

primarily due to flow instabilities within the PCUC as it moves along the continental slope (THOMSEN et al., 2016; CONTRERAS et al., 2019).

Previous studies have demonstrated that surface eddies can be highly nonlinear, thus trapping and transporting water and its constituents. Our results indicate that surface cyclones tend to be more non-linear than anticyclones, consistent with earlier findings (e. g. CHELTON et al. 2007; NAGAI et al. 2015; CZESCHEL et al. 2018). Subsurface eddies also exhibit moderately strong non-linearity, suggesting that they can transport matter, albeit with somewhat leakier than surface eddies. On the other hand, subsurface anticyclones tend to live longer than their cyclonic counterparts or those at the surface. Given their longer lifetimes, subsurface anticyclones may exert a stronger influence on deeper layers. Most subsurface eddies have radii between 25 to 30 km, while about 66% of anticyclones have radii smaller than 35 km. Cyclones tend to be smaller, with 83% having radii less than 35 km.

Although our study marks a significant advance in understanding the characteristics of surface and subsurface eddies in the Peruvian EBUS region, we also acknowledge some limitations. We focused on data from the last 27 years and did not include earlier extreme events (e.g. Ex 1972–1973, Ex 1982–1983, EP 1986–1987, EP 1991–1992 events) that would have bolstered our conclusions. The eddy detection and tracking methods we used are not perfect to track the eddies from their generation to dissipation. The detection criterion based on the layer average parameters such as OW could become unsatisfied to determine it as an eddy, leading to interruption of the tracking. This would have introduced cases where Puddies formed away from the PCUC. In addition, the reanalysis data assimilate the observation data that most likely do not cover entire lifetime of each eddy. Thus, although reanalysis data are very useful to investigate the interannual variations of eddy field on average, it can be difficult to trace back the origin of each eddy by using the eddy detection and tracking techniques for the reanalysis data. The high-resolution numerical simulations covering equatorial and Eastern Pacific regions forced with realistic surface forcing are, therefore, ideal to achieve more accurate analyses especially on subsurface eddies and their interannual modulations.

Furthermore, we did not address the biological responses to mesoscale variability under ENSO and non-ENSO conditions. Future research should integrate longer datasets and high-resolution modelling for both physics and biogeochemistry to account for seasonal and interannual modulations of the PCUC. Such comprehensive approaches would provide a more holistic understanding of this complex upwelling system, which is strongly influenced by ENSO dynamics.

6. Conclusions

In this study, we investigated the spatial-temporal variability of surface and subsurface eddies in the Peruvian eastern boundary upwelling system (EBUS) by employing high-resolution reanalysis and observational data. The reanalysis data successfully reproduced the interannual variability observed in the region.

Although previous research has primarily focused on surface-intensified eddies, this work offers new insights into the less explored subsurface-intensified eddies. We characterized their fundamental properties, explored their temporal and spatial variability, and assessed their response to extreme climate events such as El Niño and La Niña. We summarize the results of the analyses as follows.

1. Prevalence and characteristics of subsurface eddies: subsurface anticyclones (Puddies) dominate the subsurface layer, accounting for ≈ 54% of all detected subsurface eddies. They show a pronounced seasonal cycle, with peak occurrences during austral autumn and early winter, corresponding to seasonal variability in eddy kinetic energy (EKE) and modulation of the Peru-Chile undercurrent (PCUC). Puddies are primarily concentrated in the central to southern regions of the study area. They tend to be highly nonlinear, exhibit larger radii (25–30 km) and possess longer lifetimes (up to 245 days) compared to their cyclonic counterparts.
2. Response to climatic extremes: Between 1993 and 2019, subsurface anticyclones (Puddies) exhibited significant variability in response to climate extremes. Their abundance was closely tied to periods of elevated EKE, particularly during El Niño events and moderately warm years. Conversely, their occurrence declined markedly during La Niña events, notably in 2007 and 2010.
3. Contrasting mechanisms for surface and subsurface eddies: Surface-intensified eddies are predominantly influenced by winds and surface currents, whereas subsurface eddies are more sensitive to changes in the PCUC and the thermocline structure, especially under ENSO conditions. During El Niño events, the arrival of the equatorial warm pool induces thermocline deepening and enhances the PCUC along the Peruvian slope. This deepening is associated with coastal trapped waves, which are generated following the arrival of equatorial Kelvin wave at the eastern boundary. Phase speeds derived from the vertical mode equation for the first baroclinic mode Kelvin wave along the 450–m isobath showed a range 0.8–1.7 ms^{-1} with a decreasing trend toward higher latitudes, consistent with the estimated phase speeds for the reanalysis data using the cross-correlations, C_p = 1.2 m s^{-1}, and 1st order polynomial fitting, C_p ranging between 0.5 m s^{-1} to 0.83 m s^{-1} during El Niño events. Furthermore, phase speed estimated from coherence analysis for the observational data indicated mean C_p = 0.87 ms^{-1} between Chicama (7.8°S) and Callao (12 °S), which is also in good agreement with that for the reanalysis data and the solution of the vertical mode equation.

These findings agree with prior studies and highlight a significant event-dependent variations between different El Niño types. Coastal trapped waves enhance subsurface eddy activity by modulating stratification and current strength, which might suggest that coastal trapped wave can act as critical intermediaries, linking large scale equatorial variability with local subsurface eddy dynamics in the Peruvian EBUS.

Acknowledgements. We are grateful to the Japanese Ministry of education, culture, sports, science and technology (MEXT) for the financial support provided during the doctoral course of GR. This research was funded by Japan Promotion of Science (JSPS), KAKENHI (23H04818, 23H01244, 24H02224) granted to TN. We thank the Peruvian Sea Institute (IMARPE) for providing in-situ observations used in this study, which are available by request.

References

Belmadani, A., Echevin, V., Dewitte, B., and Colas, F. (2012): Equatorially forced intraseasonal propagations along the Peru-Chile coast and their relation with the nearshore eddy activity in 1992–2000: A modeling study, Journal of Geophysical Research, 117, 4025, 360, https://doi.

org/10.1029/2011JC007848.

Bertrand, A., Lengaigne, M., Takahashi, K., Avadi', A., Florence, P., and Chris, H. (2020): El Niño Southern Oscillation (ENSO) effects on fisheries and aquaculture, FAO Fisheries and Aquaculture Technical Paper No. 660., Rome, ISBN 9789251323274,https://doi.org/10.4060/ca8348en.

Camayo, R. and Campos, E. J. (2006): Application of wavelet transform in the study of coastal trapped waves off the west coast of South America, Geophysical Research Letters, 33, 1–5, https://doi.org/10.1029/2006GL026395.

Chaigneau, A., Gizolme, A., and Grados, C. (2008): Mesoscale eddies off Peru in altimeter records: Identification algorithms and eddy spatio-temporal patterns, Progress in Oceanography, 79, 106–119, https://doi.org/10.1016/j.pocean.2008.10.013.

Chelton, D. B., Schlax, M. G., Samelson, R. M., and De Szoeke, R. A. (2007): Global observations of large oceanic eddies, Geophysical Research Letters, 34,https://doi.org/10.1029/2007GL030812.

Chelton, D. B., Schlax, M. G., and Samelson, R. M. (2011): Global observations of nonlinear mesoscale eddies, Progress in Oceanography, 91, 167–216, https://doi.org/10.1016/j.pocean.2011.01.002.

Colas, F., Mcwilliams, J. C., Capet, X., and Kurian, J. (2012): Heat balance and eddies in the Peru-Chile current system, Climate Dynamics, 39, 509–529, https://doi.org/10.1007/s00382-011-1170-6, 2012.

Combes, V., Hormazabal, S., and Lorenzo, E. D. (2015): Interannual variability of the subsurface eddy field in the Southeast Pacific, Journal of Geophysical Research: Oceans, 120, 4907–4924, https://doi.org/10.1002/2014JC010265.

Conejero, C., Dewitte, B., Garçon, V., Sudre, J., and Montes, I. (2020): ENSO diversity driving low-frequency change in mesoscale activity off Peru 375 and Chile, Scientific Reports, 10, https://doi.org/10.1038/s41598-020-74762-x.

Contreras, M., Pizarro, O., Dewitte, B., Sepulveda, H. H., and Renault, L. (2019): Subsurface mesoscale eddy generation in the ocean off central Chile, Journal of Geophysical Research: Oceans, 124, 5700–5722, https://doi.org/10.1029/2018JC014723.

Czeschel, R., Schütte, F., Weller, R. A., and Stramma, L. (2018): Transport, properties, and life cycles of mesoscale eddies in the eastern tropical South Pacific, Ocean Science, 14, 731–750, https://doi.org/10.5194/os-14-731-2018.

Dewitte, B., Vazquez-Cuervo, J., Goubanova, K., Illig, S., Takahashi, K., Cambon, G., Purca, S., Correa, D., Gutierrez, D., Sifeddine, A., and Ortlieb, L. (2012): Change in El Niño flavours over 1958–2008: Implications for the long-term trend of the upwelling off Peru, Deep-Sea Research Part II: Topical Studies in Oceanography, 77–80, 143–156, https://doi.org/10.1016/j.dsr2.2012.04.011.

Echevin V., Albert A., Lévy M., Graco M., Aumont O., Piétri A., and Garric G. (2014): Intraseasonal variability of nearshore productivity in the Northern Humboldt Current System: The role of coastal trapped waves, Continental Shelf Research, 73, 14–30, https://doi.org/10.1016/j.csr.2013.11.015.

Espinoza-Morriberón, D., Echevin, V., Colas, F., Tam, J., Ledesma, J., Vásquez, L., and Graco, M. (2017): Impacts of El Niño events on the Peruvian upwelling system productivity, Journal of Geophysical Research: Oceans, 122, 5423–5444, https://doi.org/10.1002/2016JC012439.

Espinoza-Morriberón, D., Echevin, V., Colas, F., Tam, J., Gutierrez, D., Graco, M., Ledesma, J., and Quispe-Ccalluari, C. (2019): Oxygen variability during ENSO in the Tropical South Eastern Pacific, Frontiers in Marine Science, 5, 1–20, https://doi.org/10.3389/fmars.2018.00526.

Flierl, G. R. (1981): Particle motions in large-amplitude wave fields. Geophysical & Astrophysical Fluid Dynamics, 18 (1–2), 39–74. https://doi.org/10.1080/03091928108208773.

Flores, R., Espino, M., luque, G., and Quispe, J. (2013): Patrones de variabilidad ambiental en el mar peruano, Revista Peruana de Biologia, 20, 21–28, http://www.scielo.org.pe/scielo.php?script=sci_arttext&pid=S1727-99332013000100004&nrm=iso.

Gruber, N., Lachkar, Z., Frenzel, H., Marchesiello,

P., MÜNNICH, M., MCWILLIAMS, J. C., NAGAI, T., and PLATTNER, G. K. (2011): Eddy-induced reduction of biological production in eastern boundary upwelling systems, Nature Geoscience, 4, 787–792, https://doi.org/10.1038/ngeo1273.

HORMAZABAL, S., SHAFFER, G., and LETH, O. (2004): Coastal transition zone off Chile, Journal of Geophysical Research: Oceans, 109, https://doi.org/10.1029/2003JC001956.

KAO, H.-Y. and YU, J.-Y. (2009): Contrasting Eastern-Pacific and Central-Pacific types of ENSO, Journal of Climate, 22, 615 - 632, https://doi.org/10.1175/2008JCLI2309.1.

KESSLER, W. S., MCPHADEN, M. J., and WEICKMANN, K. M. (1995): Forcing of intraseasonal Kelvin waves in the equatorial Pacific, Journal of Geophysical Research, 100, https://doi.org/10.1029/95JC00382.

LELLOUCHE, J.-M., GREINER, E., LE GALLOUDEC, O., GARRIC, G., REGNIER, C., DREVILLON, M., BENKIRAN, M., TESTUT, C.-E., BOURDALLE-BADIE, R., GASPARIN, F., HERNANDEZ, O., LEVIER, B., DRILLET, Y., REMY, E., and LE TRAON, P.-Y. (2018): Recent updates to the Copernicus Marine Service global ocean monitoring and forecasting real-time 1/12° high-resolution system, Ocean Science, 14, 1093–1126, https://doi.org/10.5194/os-14-1093-2018.

LUKAS, R. and FIRING, E.: (1984) The geostrophic balance of the Pacific Equatorial Undercurrent, Deep-Sea Research Part A, Oceanographic Research 405 Papers, 31, 61–66, https://doi.org/10.1016/0198-0149 (84) 90072-4.

MOLEMAKER, M. J., MCWILLIAMS, J. C., and DEWAR, W. K. (2015): Submesoscale instability and generation of mesoscale anticyclones near a separation of the California Undercurrent, Journal of Physical Oceanography, 45, 613–629, https://doi.org/10.1175/JPO-D-13-0225.1.

MONTES, I., COLAS, F., CAPET, X., and SCHNEIDER, W. (2010): On the pathways of the equatorial subsurface currents in the eastern equatorial Pacific and their contributions to the Peru-Chile Undercurrent, Journal of Geophysical Research: Oceans, 115, 1–16, 410, https://doi.org/10.1029/2009JC005710.

NAGAI, T., GRUBER, N., FRENZEL, H., LACHKAR, Z., MCWILLIAMS, J. C., and PLATTNER, G. K. (2015): Dominant role of eddies and filaments in the offshore transport of carbon and nutrients in the California Current System, Journal of Geophysical Research: Oceans, pp. 5318–5341, https://doi.org/10.1002/2015JC010889.

OKUBO, A. (1970): Horizontal dispersion of floatable particles in the vicinity of velocity singularities such as convergences, Deep-Sea Research, 17, 454–454.

POLI, L., ARTANA, C., and PROVOST, C. (2022): Topographically Trapped waves around South America with periods between 40 and 130 days in a global ocean reanalysis, Journal of Geophysical Research: Oceans, 127, https: //doi. org/10.1029/2021JC018067.

RAMÍREZ, I. J. and BRIONES, F. (2017): Understanding the El Niño Costero of 2017: The definition problem and challenges of climate forecasting and disaster responses, International Journal of Disaster Risk Science, 8, 489–492, https://doi.org/10.1007/s13753-017-0151-8.

ROSALES QUINTANA, G. M., MARSH, R., and ICOCHEA SALAS, L. A. (2021): Interannual variability in contributions of the Equatorial Undercurrent (EUC) to Peruvian upwelling source water, Ocean Science, 17, 1385–1402, https://doi.org/10.5194/os-17-1385-2021.

SANTOSO, A., MCPHADEN, M. J., and CAI, W. (2017): The defining characteristics of ENSO extremes and the strong 2015/2016 El Niño, Reviews of Geophysics, 55, 1079–1129, https://doi.org/10.1002/2017RG000560.

SU, J., XIANG, B., WANG, B., and LI, T. (2014): Abrupt termination of the 2012 Pacific warming and its implication on ENSO prediction, Geophysical Research Letters, 41, 9058–9064, https://doi.org/10.1002/2014GL062380.

TAKAHASHI, K. and DEWITTE, B. (2016): Strong and moderate nonlinear El Niño regimes, Climate Dynamics, 46, 1627–1645, https://doi.org/10.1007/s00382-015-2665-3.

THOMSEN, S., KANZOW, T., KRAHMANN, G., GREATBATCH, R. J., DENGLER, M., and LAVIK, G. (2016):

The formation of a subsurface anticyclonic eddy in the Peru-Chile Undercurrent and its impact on the near-coastal salinity, oxygen, and nutrient distributions, Journal of Geophysical Research: Oceans, 121, 476–501, https://doi.org/10.1002/2015JC010878.

Toggweiler, J. R., Dixon, K., and Broecker, W. S. (1991): The Peru upwelling and the ventilation of the south Pacific thermocline, Journal of Geophysical Research, 96, 20467, https://doi.org/10.1029/91JC02063.

Toniazzo, T. (2010): Climate variability in the southeastern tropical Pacific and its relation with ENSO: A GCM study, Climate Dynamics, 34, 435 1093–1114, https://doi.org/10.1007/s00382-009-0602-z.

Vergara, O., Dewitte, B., Montes, I., Garçon, V., Ramos, M., and Pizarro, O. (2016): Seasonal variability of the oxygen minimum zone off Peru in a high-resolution regional coupled model, Biogeosciences, 13, 4389–4410, https://doi.org/10.5194/bg-13-4389-2016.

Weiss, J. (1991): The dynamics of enstrophy transfer in two-dimensional hydrodynamics, Physica D: Nonlinear Phenomena, 48, 273–294, https://doi.org/10.1016/0167–2789 (91) 90088–Q.

Received: December 23, 2024
Accepted: July 11, 2025

La mer 63 : 123–139, 2025, https://doi.org/10.32211/lamer.63.3-4_123
Société franco-japonaise d'Océanographie, Tokyo

過去 22 年間の葛西海浜公園西なぎさ（東京都）における魚類相

小川悠介[1)]・宮﨑寧子[1)]・市川啓介[1)]・河野 博[2)]・丸山啓太[3)]*

Ichthyofauna of an artificial tidal flat in Kasai Marine Park, located in the inner Tokyo Bay, over the past 22 years

Yusuke Ogawa[1)], Yasuko Miyazaki[1)], Keisuke Ichikawa[1)], Hiroshi Kohno[2)] and Keita Maruyama[3)]

Abstract: Nishi-nagisa in Kasai Marine Park, located in the inner Tokyo Bay, is an artificial tidal flat developed in 1988 in Edogawa-ku, Tokyo, Japan. The tidal flat consists of about 15 ha of tideland and 23 ha of sea area, and faces south to Tokyo Bay. Annual samplings of fishes using a small seine net and physical environment surveys were carried out in the tidal flat from April 1999 to December 2020. A total of 299,609 individuals of over 70 species belonging to 35 families were collected. Marine fishes dominated in the number of species, and estuarine fishes dominated in the number of individuals for 22 years. Cluster analysis and NMDS showed that the community structure was divided into three groups（around 2000, mid to late 2000s, and after 2010）, with correlated species in each group. Diversity index has shown a slight upward trend in recent years, with higher than other closed artificial tidal flats in the inner Tokyo Bay. The tidal flat provides suitable habitat for *Gymnogobius macrognathos*（endangered species）. Our study suggests that the tidal flat is changing the ichthyofauna while being influenced by the species that occur in Tokyo Bay, providing habitat for a variety of fish species, including endangered species.

Keywords: artificial tideland, fish fauna, juvenile, endangered species

1）〒 134–8587 東京都江戸川区臨海町 6–2–3 公益財団法人東京動物園協会 葛西臨海水族園 Tokyo Sea Life Park, 6–2–3 Rinkai-cho, Edogawa-ku, Tokyo 134–8587, Japan
2）〒 130–0021 東京都墨田区緑 4–20–9 公益財団法人長尾自然環境財団 Nagao Natural Environment Foundation, 4–20–9 Midori, Sumida-ku, Tokyo 130–0021, Japan
3）〒 108–8477 東京都港区港南 4–5–7 国立大学法人東京海洋大学学術研究院海洋環境科学部門 Department of Ocean Sciences, Tokyo University of Marine Science and Technology（TUMSAT）, 4–5–7 Konan, Minato-ku, Tokyo 108–8477, Japan
＊連絡先（Corresponding author）住所：〒 108–8477 東京都港区港南 4–5–7 国立大学法人東京海洋大学学術研究院海洋環境科学部門 Department of Ocean Sciences, Tokyo University of Marine Science and Technology（TUMSAT）, 4–5–7 Konan, Minato-ku, Tokyo 108–8477, Japan
電話番号：080–6553–7373
アドレス：bokuwamoku@gmail.com

1. 背景と目的

東京湾は，日本列島の本州において，太平洋側の最も突き出た場所にある大きな内湾で，千葉県の房総半島と神奈川県の三浦半島に東西を囲まれ，最奥部で東京都に接する縦長の形状をもつ。厳密には房総半島の洲崎と三浦半島の剱崎を結んだ線より北の海域として定義されるが，便宜的に東京湾内湾（千葉県の富津岬と神奈川県の観音崎を結んだ線より北の海域）と東京湾外湾（その線より南の海域）に区別される（河野，2011）。明治時代後期までは，東京湾内湾の沿岸域には連続的な干潟や浅場が存在しており，有用な漁場になっていた（国土交通省港湾局・環境省自然環境局，2004）。しかし，1950 年代に入ると内湾への汚染負荷が増え始めて水質問題が深刻化し，さらに 1960 年代より多くの干潟や浅場が埋め立てられることにより，魚介類の減少が見られるようになった（清水，1990）。とくに埋め立てによる干潟と浅場の減少は著しく，戦前の干潟の総面積は 136 km^2とされていたが，1973 年には 10 km^2にまで減少した（鎌谷, 1993）。このような状況の中で，1970 年代より積極的に干潟や浅場を造成しようとする動きが見られるようになり（中瀬，2008），1997 年における干潟の面積は 16.4 km^2と増加している（環境庁自然保護局，1997）。その後も，2007 年には 12,000 m^2の人工海浜，10,000 m^2の人工干潟および 46,000 m^2 の浅場を有する大森ふるさとの浜辺公園（東京都大田区）の開園や，2020 年には港区の運河上に約 400 m^2の人工干潟が造成されるなど，干潟の面積は少しずつ増加している。

失われた干潟やそれに続く浅場などのごく浅い海域は，魚類にとって重要な成育・生息場として知られ，現在の東京湾内湾では多摩川河口の干潟や小櫃川河口の干潟など，数少ない干潟がその機能を担っている（加納ほか，2000；Hermosilla *et al.*, 2012）。また，埋め立てによって造成された護岸に土砂が堆積するような形でできた半自然的な干潟における調査（那須ほか，1996；茂木ほか，2009；村瀬ほか，2014）や，人工干潟における調査（桑原ほか，2003；山根ほか，2004；河野ほか，2008；村井ほか，2016；宍戸ほか，2019；丸山ほか，2021；中野ほか，2023）も進み，自然干潟ではない干潟も魚類に重要な成育・生息場を提供している可能性が示されている。一方で，造成された干潟における調査は 1 年などの短期的なものが多い。東京都大田区の京浜島の干潟で魚類相を調査した茂木ほか（2009）は，人工物造成後の仔稚魚への影響を知るためには 1 年といった短期間ではなく，長期間のモニタリングが必要であるとしている。長期的な調査としては，多摩川河口周辺の 3 つの干潟における 6 年間の調査（村瀬ほか，2014）や，東京都大田区の大森ふるさとの浜辺公園内の人工干潟における 5 年間の調査（丸山ほか，2021）が実施されてきた。ただし，千葉県市川市の行徳鳥獣保護区内の干潟において，1990 年代から 2010 年代までの魚類相を 10 年ごとに比較した中野ほか（2023）は，優占種や多様度が 10 年という期間で大きく変化し，より長期的な視野で人工干潟について考えていく必要性を明らかにしている。しかし，そういった長期的な調査から人工干潟を評価した事例は極めて少ない。

そこで本研究では，人工干潟である葛西海浜公園の「西なぎさ」において，1999 年から 2020 年まで小型地曳網を用いた魚類相調査を行うことで，約 20 年間の魚類相の変遷を把握し，出現する魚種や多様度から人工干潟の長期的な評価を行った。また，それらの結果を東京湾内湾に位置する他の干潟と比較することで，葛西海浜公園「西なぎさ」の魚類相の特徴を明らかにした。

2. 調査地点の概要

調査は，東京湾の最奥に位置する東京都江戸川区の葛西海浜公園内の人工干潟「西なぎさ」で行った（Fig. 1 の Nishi-nagisa）。本公園は，「西なぎさ」と「東なぎさ（Fig. 1 の Higashi-nagisa）」の 2 つのなぎさとその周囲の水域で構成される。「西なぎさ」は一般に公開され，水遊びなどができる憩いの場として利用されている。「東なぎさ」は，原則立ち入り禁止の自然保護区である。両なぎさは，隣接する葛西臨海公園とともに「葛西沖開発土地区画整理事業」において，埋め立て造成され

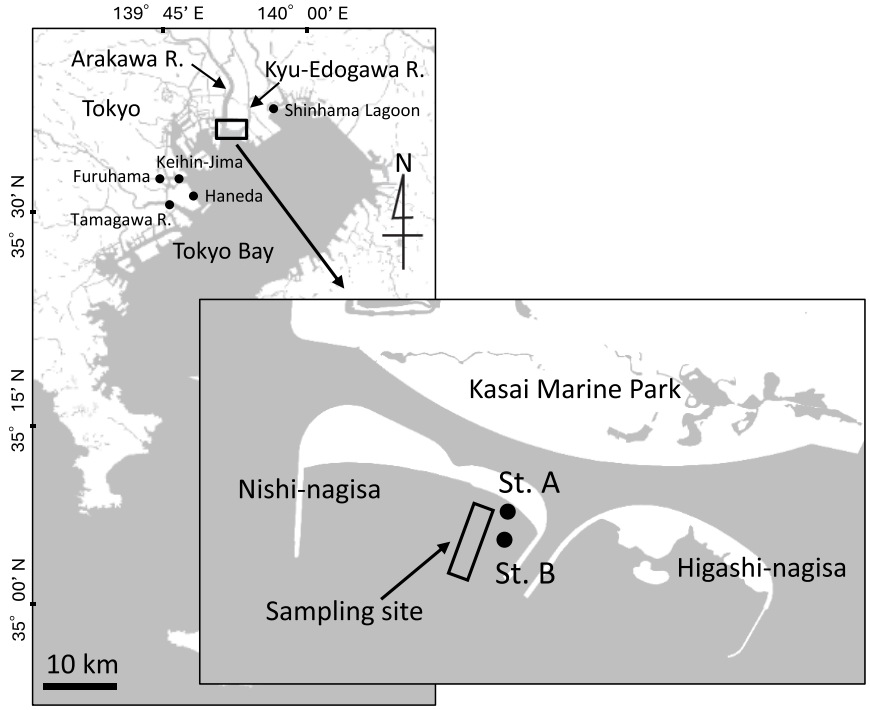

Fig. 1 Map showing the sampling site at Kasai Marine Park and 5 comparative sampling sites in Tokyo Bay. Sts. A and B indicate particle size ratios and median particle sizes of bottom sediment survey sites. The maps are taken from the Geospatial Map Vector published by the Geospatial Information Authority of Japan（http://maps.gsi.go.jp/）.

た区画で，自然環境の回復やレクリエーションなどを目的に，埋め立てられた自然海岸の代替として計画された（岡，2021）。1972 年から造成がはじまり，1978 年には導流堤建設に着手，1983 年には土砂投入に至り「東なぎさ」の造成は完了した。その後，「西なぎさ」は 1988 年に完成している。投入した砂泥は，「東なぎさ」は浚渫砂泥を用い，「西なぎさ」は親水公園であるので自然の山砂が用いられた。両なぎさともに，造成した干潟からの土砂流出を抑えるために，東西から中央に向かい逆 U 字型の導流堤が造成されている。両なぎさの干潟の建設時の面積は，「西なぎさ」は 15,000 m^2ほど（水域を含めると 38,000 m^2ほど），「東なぎさ」は 10,000 m^2ほど（水域を含めると 30,000 m^2ほど）である。両なぎさや周辺海域では，造成後も適時浚渫などの順応的管理が行われている。

3. 材料と方法

3. 1 現地調査

採集は 1999 年 4 月から 2020 年 12 月の期間の偶数月に行った（ただし，2000 年 4 月，2004 年 10 月，2010 年 4 月，2011 年 4 月および 2012 年 2 月は調査を行っていない）。採集は小型地曳網（1999 年 4 月から 2010 年 3 月の期間：袖網部の長さ 450 cm，胴網部の長さ 210 cm，袋網部の長さ 150 cm，袋網部の目合い 18 メッシュ 1.2 mm；2010 年 4 月から 2020 年 12 月の期間：袖網部の長さ 380 cm，胴網部の長さ 240 cm，袋網部の長さ 140 cm，袋網部の目合い 24 メッシュ: 0.8 mm）を用い，水深 1 m 付近を汀線に対して垂直に 30 m を 2 回曳網した。この際，潮汐は考慮せず午前 10:00～12:00 に調査を行った。網口の幅は約 5 m になるように曳網することで，一回の曳網で 150 m^2あ

たりの魚類を採集した。採集物は現場で直ちに10 %ホルマリンで固定し，葛西臨海水族園へ持ち帰った。

調査地点の物理環境の年変動を把握することを目的として，設置型のロガー（U22 ウォーターテンププロ v2，HOBO U26 溶存酸素ロガー：Onset 社）を用いて，水温，塩分および溶存酸素量（以下，DO）を測定した。測定期間は，2021 年 6 月 19 日から 2022 年 6 月 16 日までの約 1 年間とし，30 分間隔でデータを記録し，各日の日中 12:00 のデータを抽出した（ただし，2021 年 12 月 13 日は，午前中にロガーの整備を実施したため，午前 9:00 のデータを抽出した）。加えて，調査地点の粒度分布を把握することを目的として，底質の分析を行った。調査地点は，小型地曳網を曳網した地点から東に約 150 m の距離に定点を設けた（Fig. 1 の St. A と St. B）。なお，本調査地点は砂質の中にスポット的に泥質干潟が存在しているため，そのような底質の差を把握することを目的とし，粒度の粗い地点と細かい地点の 2 地点を選定した。調査日は 2021 年 6 月 9 日，9 月 6 日，11 月 4 日および 2022 年 3 月 3 日とし，シャベルを用いて直径 5.0 cm ×深さ 5.0 cm の底土を，各調査地点につき 2 か所で採泥した。採泥したサンプルは水族園に持ち帰った後に乾燥させ，粒度組成を 74 μm 以下，74〜149 μm，149〜250 μm，250〜840 μm，840 μm 以上の 5 つに区分し，中央粒径値を算出した。

3. 2 種の同定

採集した魚類は，一週間ほどホルマリンで固定した後に，種の同定および個体数の計数を行った。種の同定は，中坊（編）(1993)，中坊（編）(2000)，中坊（編）(2013)，沖山（編）(1988) および沖山（編）(2014) に従った。科の配列と学名，和名は主に中坊（編）(2013) に従った。また，これら採集された魚類は主に加納ほか (2000) および大森ほか (2018) に従い，生活史型を 6 つ［河口魚：河口域もしくは河口域と海域の境界で産卵を行い河口域で全生活史のほぼ全てを完結する種（仔魚期に海域へ分散することもある），海水魚：海域で産卵を行う種で，基本的には河川淡水域では成長しない，遡河回遊魚：産卵のために河川を遡り，淡水域で産卵を行う種，降河回遊魚：産卵のために河川を降り，海域で産卵を行う種，両側回遊魚：産卵を河川淡水域で行い，仔魚は流下して海域で少し成長した後に河川へ戻り，河川で成長・成熟する種，淡水魚：河川淡水域で産卵を行い，生活史を淡水域で完結させる種］に区分した。生活史の区分は，科もしくは属レベルまでしか同定できなかった個体については行っていない（ただし，ミミズハゼ属の一種は河口魚として扱った）。なお，2012 年 4 月以降に採集した魚類については，体長の測定を行った。2016 年 4 月以降のサンプルは，水族園にて 10 %ホルマリン液浸標本で収蔵している。

3. 3 群集解析

採集された魚類の群集組成について，年変動を明らかにするために，各年の各種の個体数に基づき類似度を求め，クラスター分析を行った。年間の類似度指数には Bray-Curtis 指数を，クラスター連結には群平均法を用い，類似度 25 以上でグループ分けを行った。また，認められたグループごとの指標種を明らかにするために，統計的な有意水準を 0.05 とし，指標種分析（IndVal 法：Dufrene and Legendre, 1997）を行った。これらの解析には，統計解析ソフト R（R Development Core Team, 2025）を用い，クラスター分析では vegan パッケージの hclust 関数を，IndVal 法では labdsv パッケージの indval 関数を使用した。

その後，上記と同様の類似度指数を用いて非計量多次元尺度構成法（non-metric multidimensional scaling，以下 NMDS）解析を行った。その際，得られた NMDS のストレス値が適切な範囲［Stress ＜ 0.2，（大垣，1999）］であることを確認したうえで二次元平面状にプロットした。次に，出現種と年ごとの関係を視覚化するために NMDS の結果と各種の個体数との相関を調べ，有意に相関する種を NMDS 上にベクトルとして表示した（ベクター解析）。ベクター解析の統計的な有意水準は 0.05 としたが，視認性を考慮し，

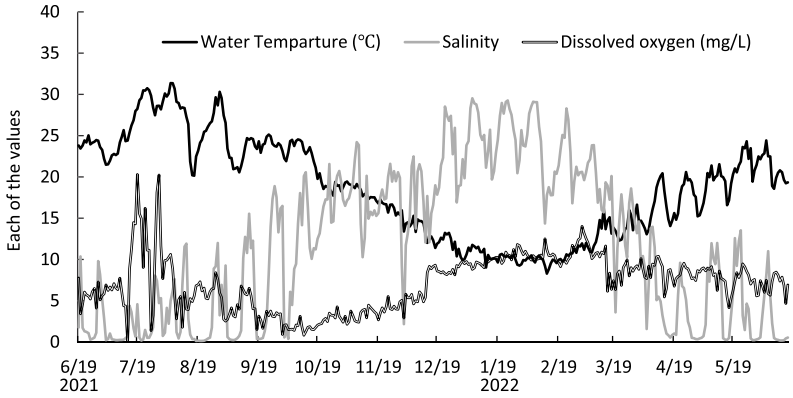

Fig. 2 Fixed intervals（1-day）changes of water temperature, salinity and dissolved oxygen（DO）at Kasai Marine Park in Tokyo Bay from June 19, 2021 to June 16, 2022.

有意水準 0.01 の種のみをベクトル表示した。ベクトルの長さは各調査地点の座標との相関の高さを表す。最後に，グループごとに群集組成が有意に異なるかを明らかにするために，有意水準 0.05 とし，pairwisePERMANOVA（PERmutational Multivariate ANalysis Of VAriance）を実施した。これらの解析には R を用い，NMDS は vegan パッケージの metaMDS 関数を，ベクター解析は vegan パッケージの envfit 関数を，pairwise-PERMANOVA には pairwiseAdonis パッケージの pairwise.adonis 関数を使用した。

また，群集組成の比較を行うために，木元（1993）に従い年ごとの Shannon-Wiener の多様度 *H'* を求めた。多様度 *H'* については，東京湾内湾他地点の干潟と比較することを目的とし，2014 年から 2019 年の間の大森ふるさとの浜辺公園の人工干潟（丸山ほか，2021），2007 年と 2013 年の多摩川河口の自然干潟（村瀬ほか，2014），2007 年と 2013 年の埋め立て地である京浜島に土砂が自然に堆積してできた干潟（茂木ほか，2009；梅田・河野，2017），2007 年と 2013 年の羽田空港の北東の小規模な人工前浜干潟（村瀬ほか，2014）および 2004 年と 2018 年の人工潟湖である新浜湖内の干潟（河野ほか，2008；中野ほか，2023）の結果も算出した。ただし比較に用いたデータは，大森ふるさとの浜辺公園は各年の偶数月のデータを抽出したが，他の干潟については毎月一度の通年の調査（計 12 回）の結果である。

4. 結果

4. 1 物理環境

水温は，季節に合った一般的な年変動を示した（Fig. 2）。7 月から 8 月にかけての水温は特に高く，2021 年 8 月 5 日と 8 月 6 日は最も高い 31.4℃を記録した。9 月以降の水温は徐々に下がっていき，2 月には 8.3℃まで低下した。塩分はおおむね春季から夏季に低く冬季に高くなる傾向を示したが，変動が大きかった。塩分の年間の平均 ± SD は，11.7 ± 9.2 であった。DO は，6 月から 8 月にかけては変動が大きく，9 月から 10 月にかけては年間の中でも低い値をとり，12 月から 3 月にかけては高い値であった。9 月や 10 月にかけての DO は，3.0 mg/L 以下まで低下することも確認された。DO の年間の平均 ± SD は 7.1 ± 3.3 mg/L であった。

底質は 2 定点で違いがみられ，年間を通して汀線に近い St. A の方が粗かった（Fig. 3）。高い割合を示した粒径階は，St. A では 150〜249 μm（46.5〜61.8%），St. B では 75〜149 μm（39.0〜45.0%）と 150〜249 μm（23.6〜34.1%）であった。74 μm 以下の粒径の割合は，St. A では 2.0〜3.0 % と低かったが，St. B では 13.0〜29.0% であった。

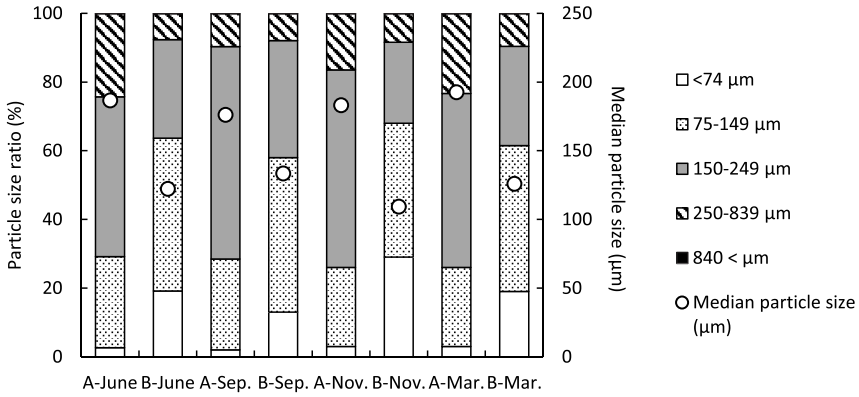

Fig. 3 Particle size ratios (bars) and median particle sizes (open circles) of bottom sediment at Kasai Marine Park in Tokyo Bay from 2021 to 2022.

840 μm 以上の粒径の割合は，両地点ともに 1.0% 以下であった。中央粒径値は，St. A で 176.1～192.5 μm，St. B で 109.3～133.5 μm であった。

4. 2 採集された魚類の概要

採集された魚類は，合計で 35 科 58 属 70 種以上 299,609 個体であった（Table 1）。科別の割合ではハゼ科が最も多く，18 種（採集された総種数の 25.6%）241,576 個体（採集された総個体数の 80.6%）であった。優占した上位 5 種は，マハゼ *Acanthogobius flavimanus*（採集された個体数は 70,980 個体で，総個体数の 23.7%），エドハゼ *Gymnogobius macrognathos*（64,849 個体, 21.6%），ビリンゴ *Gymnogobius breunigii*（34,669 個体, 11.6 %），コノシロ *Konosirus punctatus*（32,136 個体，10.7%），スズキ *Lateolabrax japonicus*（9,169 個体，3.1%）であり，これら 5 種で採集された総個体数の 70.7% を占めた。アカエイ *Dasyatis akajei* やカライワシ *Elops hawaiensis* をはじめとした 35 種以上（採集された総種数のうち 50 %以上）は，全期間を通して採集個体数が 10 個体以下であった。

4. 3 種数と個体数の経年変化

過去約 20 年間における 1 年間の平均種数は 24.2 種であり，最も少ない年は 2006 年の 16 種，最も多い年は 2020 年の 36 種であった（Fig. 4）。過去約 20 年間で特徴的な傾向は確認できなかったが，近年は少し種数が多い傾向であった。過去約 20 年間における 1 年間の平均個体数は 13,619 個体であり，最も少ない年は 2000 年の 863 個体，最も多い年は 2003 年の 47,579 個体であった（Fig. 4）。採集された個体数は年ごとに変動が大きかった。

4. 4 生活史型別の出現と割合の経年変化

生活史型別の種数では，全ての年で海水魚がもっとも多く，8～20 種であった（Fig. 5）。各年の総種数に対する海水魚の種数の割合は 47.7～69.6% であった（Fig. 6）。海水魚の次に多く出現した生活史型は河口魚であり，その種数は 5～10 種であった。各年の総種数に対する河口魚の種数の割合は 20.8～43.8% であった。両側回遊魚は毎年 1～3 種が出現し，総種数に対する割合は 4.0～11.5% であった。遡河回遊魚は 1 種が不定期に出現し，総種数に対する割合は 5.6% 以下であった。淡水魚は 5 か年のみ出現し，出現種数は各年 2 種以下で，総種数に対する割合は 9.5% 以下であった。

生活史型別の個体数では，22 年間のうち 17 か年において河口魚が最も多く採集された（Fig. 7）。2000 年，2002 年，2011 年および 2020 年の 4 か年は海水魚が最も多く採集され，1999 年の 1 か年のみ両側回遊魚が最も多く採集された。優占し

Table 1. Fishes collected at Kasai Marine Park in Tokyo Bay from April 1999 to December 2020

Family	Species	Individual numbers	%	SL (mm)	Year	Life-cycle category
Dasyatidae	*Dasyatis akajei*	2		106–121	'19	M
Elopidae	*Elops hawaiensis*	7		35–138	'06, '11, '15, '18	M
Clupeidae	*Konosirus punctatus*	32136	10.7	7–83	'99–'05, '07–'20	M
	Sardinella zunasi	4882	1.6	8–80	'99–'04, '06–'20	M
Engraulidae	*Engraulis japonica*	34		49–61	'99, '01, '03, '05, '06, '08, '17, '19	M
Cyprinidae	*Candidia temminckii*	1		22	'14	F
	Carassius sp.	1		-	'05	F
	Cyprinus carpio	1		-	'05	F
	Hypophthalmichthys molitrix	1		17	'18	F
	Opsariichthys platypus	1		-	'99	F
	Opsariichthys uncirostris uncirostris	1		61	'14	F
	Tribolodon brandtii	187	0.1	21–92	'00, '01, '07, '12–'14, '17–'20	An
	Tribolodon spp.	10		-	99, '03, '06, '09, '10	-
Osmeridae	*Hypomesus nipponensis*	1		-	'99	An
Plecoglossidae	*Plecoglossus altivelis altivelis*	3381	1.1	7–66	'99–'20	Am
Salangidae	*Salangichthys ishikawae*	187	0.1	26–43	'99, '00, '02, '03, '07, '08, '10, '17–'20	M
Syngnathidae	*Syngnathus schlegeli*	6		40–72	'13–'17	M
	Urocampus nanus	1		45	'15	M
Mugilidae	*Chelon affinis*	1		-	'03	M
	Chelon haematocheilus	4		-	'00, '03, '05	M
	Chelon spp.	88		12–31	'00, '01, '03–'07, '10, '13, '16–'18, '20	M
	Moolgarda perusii	8		-	'99, '20	M
	Mugil cephalus cephalus	1564	0.5	20–94	'99–'09, '11, '13–'20	M
	Mugilidae spp.	6		-	'00, '01	M
Atherinidae	*Hypoatherina valenciennei*	65		8–23	'06, '07, '10, '13, '16, '17, '19	M
Poeciliidae	*Gambusia affinis*	1		30	'19	F
Hemiramphidae	*Hyporhamphus intermedius*	9		95–142	'14, '15, '19	M
	Hyporhamphus sajori	13		26–42	'19	M
	Hyporhamphus sp.	1		8	'19	M
Exocoetidae	Exocoetidae sp.	1		12	'13	M
Belonidae	*Strongylura anastomella*	2		103–174	'17	M
Sebastidae	*Sebastes pachycephalus pachycephalus*	3		6	'03, '14	M
	Sebastes sp.	2		-	'03	M
Platycephalidae	*Platycephalus* sp.2	364	0.1	6–134	'99, '00, '02–'04, '07–'20	M
Lateolabracidae	*Lateolabrax japonicus*	9169	3.1	11–134	'99–'20	M
Leiognathidae	*Nuchequula nuchalis*	1898	0.6	5–26	'19–'03, '05, '08, '10–'15, '17–'20	M
	Leiognathidae sp.	1		7	'18	M
Gerreidae	*Gerres equulus*	4		10–43	'13, '14	M
Haemulidae	*Plectorhinchus cinctus*	25		7–43	'99, '02, '08, '09, '11, '13–'15, '17, '19, '20	M
Sparidae	*Acanthopagrus latus*	23		13–20	'12, '16, '17, '19	M
	Acanthopagrus schlegelii	847	0.3	8–48	'00, '07, '09, '10, '13–'20	M
Sciaenidae	*Nibea mitsukurii*	6		6–17	'02, '11, '14, '20	M
	Pennahia argentata	454	0.2	12–36	'07, '08, '10, '14, '15, '18	M
Sillaginidae	*Sillago japonica*	182	0.1	6–48	'00, '02, '04, '05, '07, '08, '10, '11, '13, '14, '16, '18	M
Teraponidae	*Rhyncopelates oxyrhynchus*	6		-	'99, '02	M
	Terapon jarbua	126		60	'99, '00, '03, '05, '07, '08, '13	M
Girellidae	*Girella punctata*	1		32	'18	M
Stichaeidae	Stichaeidae sp.	1		-	'08	M
Pholidae	*Pholis crassispina*	3		-	'08	M
	Pholis nebulosa	13		-	'99–'01, '09	M
	Pholis sp.	4		-	'03	M
Blenniidae	*Omobranchus elegans*	1		-	'03	M
	Omobranchus punctatus	4		20–63	'18, '19	M
	Omobranchus spp.	52		7–13	'99–'02, '04, '06, '07, '09, '14, '16, '18, '20	M
Callionymidae	*Repomucenus valenciennei*	2		25	'03, '14	M
Gobiidae	*Acanthogobius flavimanus*	70980	23.7	9–152	'99–'20	E
	Acanthogobius lactipes	4873	1.6	10–56	'99–'09, '11–'20	E
	Acentrogobius sp.2	1		23	'19	E
	Chaenogobius gulosus	1		-	'02	M
	Eutaeniichthys gilli	795	0.3	4–36	'01–'20	E

	Favonigobius gymnauchen	804	0.3	8–57	'99–'20	M
	Gymnogobius breunigii	34669	11.6	7–48	'99–'20	E
	Gymnogobius heptacanthus	73		16–38	'01, '04–'08, '10, '14–'16, '18–'20	E
	Gymnogobius macrognathos	64849	21.6	9–40	'99–'20	E
	Gymnogobius petschiliensis	389	0.1	15–31	'13–'16, '18, '20	Am
	Gymnogobius uchidai	201	0.1	16–28	'06–'10, '12, '15–'17, '19, '20	E
	Gymnogobius urotaenia	116		15–28	'99, '01, '02, '04, '12–'14, '20	Am
	Gymnogobius spp.	5525	1.8	8–30	'03–'09, '11, '13–'17, '19, '20	-
	Luciogobius spp.	82		7–15	'03–'05, '07, '08, '11–'14, '16–'18, '20	E
	Mugilogobius abei	48		-	'99, '00, '02	E
	Pseudogobius masago	2		-	'99	E
	Rhinogobius spp.	4		-	'99	-
	Tridentiger bifasciatus	140		14–60	'02, '04, '09, '13, '14, '16–'20	E
	Tridentiger obscurus	3		15–27	'19	E
	Tridentiger spp.	7228	2.4	9–22	'99–'20	-
	Gobiidae spp.	50793	17.0	5–17	'03–'20	-
Pleuronectidae	*Kareius bicoloratus*	186	0.1	10–61	'99, '00, '02, '04–'08, '12–'18	M
	Pleuronectes yokohamae	16		-	'03	M
	Pleuronectidae sp.	1		-	'09	-
Cynoglossidae	*Paraplagusia japonica*	6		-	'05, '07	M
Triacanthidae	*Triacanthus biaculeatus*	1789	0.6	3–38	'00–'02, '04, '07–'11, '13, '14, '16, '17, '20	M
Tetraodontidae	*Takifugu rubripes*	154	0.1	14–36	'14, '16, '17, '19	M
	Takifugu niphobles	22		13–41	'00, '02, '12, '18–'20	M
	Tetraodontidae spp.	65		4–19	'07, '09, '11, '13, '15, '18	-

Life-cycle categories: Am, amphidromos fishes; An, anadromous fishes; E, estuarine fishes; F, freshwater fishes; M, marine fishes

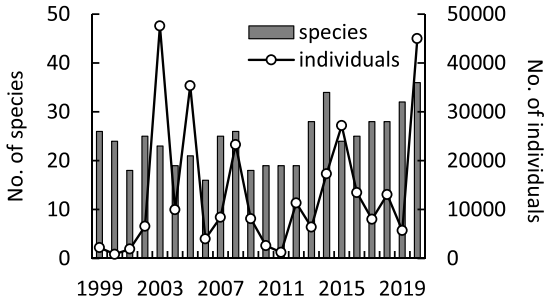

Fig. 4 Annual changes of the numbers of species (solid bars) and individuals (open circles) at Kasai Marine Park in Tokyo Bay from 1999 to 2020.

た回数の多かった河口魚は，各年に 145～31,302 個体が採集され，各年に採集された総個体数のうち，19.7～96.3% を占めた（Fig. 8）。とくに，総個体数のうち河口魚が占める割合が 70% を超えた年は，合計で 16 か年であった。海水魚は，207～25,120 個体が採集され，総個体数に対する割合は 3.0～72.0% であった。両側回遊魚は年間 3～953 個体が出現し，総個体数に対する割合は 1.0% 以下～60.4% であった。遡河回遊魚は 100 個体以下である場合が多く，2014 年は 108 個体が採集され，総個体数に対する割合も各年で 1% 程度かそれ以下であった。淡水魚は 1～2 個体が出現する年が 5 か年のみ確認された。

4. 5 群集解析と多様度

クラスター分析の結果では，類似度 25 で 3 つのグループ（グループ 1: 1999～2002 年，2006 年，2011 年; グループ 2: 2004，2005，2008，2009，2012 年; グループ 3: 2003，2007，2010，2013～2020 年）に分けられ，おおまかに 2000 年前後，2000 年代半ばから後半，2010 年以降で魚類群集がまとまる傾向が認められた（Fig. 9）。それぞれのグループの指標種は，グループ 1 はアユ *Plecoglossus altivelis altivelis*（IndVal = 0.72，$p < 0.01$），アベハゼ *Mugilogobius abei*（IndVal = 0.50，$p < 0.05$）およびギンポ *Pholis nebulosa*（IndVal = 0.41，$p < 0.05$），グループ 2 はマハゼ *Acanthogobius flavimanus*（IndVal = 0.92，$p < 0.01$），グループ 3 はコノシロ *Konosirus punctatu*s（IndVal = 0.97，$p < 0.01$），クロダイ *Acanthopagrus schlegelii*（IndVal = 0.89，$p < 0.01$），エドハゼ *Gymnogobius macrognathos*（IndVal = 0.97，$p < 0.01$），シモフリシマハゼ *Tridentiger bifasciatus*（IndVal = 0.59，$p < 0.05$），スミウキゴリ *Gym-*

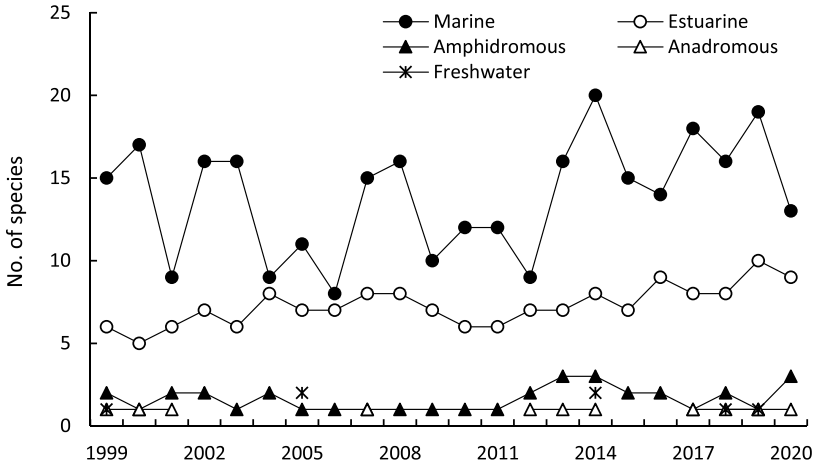

Fig. 5 Annual changes of the numbers of species by life-cycle categories at Kasai Marine Park in Tokyo Bay from 1999 to 2020.

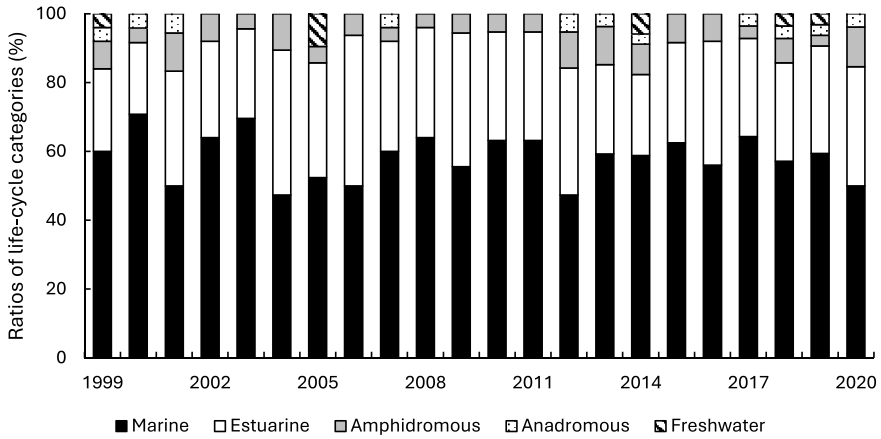

Fig. 6 Annual changes of ratio of numbers of species by life-cycle categories at Kasai Marine Park in Tokyo Bay from 1999 to 2020.

nogobius petschiliensis（IndVal = 0.55, $p < 0.05$）およびヨウジウオ *Syngnathus schlegeli*（IndVal = 0.45, $p < 0.05$）であった。

NMDS の結果では，3 つのグループに属する各年は近い位置に配置された（Fig. 10）。ストレス値は 0.10 であった。ベクター解析の結果，有意に相関がある種として，グループ 1 にはアユ（$r^2 = 0.42$, $p < 0.01$），ナンヨウボラ *Moolgarda perusii*（$r^2 = 0.27$, $p = 0.01$），コトヒキ *Terapon jarbua*（$r^2 = 0.39$, $p < 0.01$）およびギンポ（$r^2 = 0.46$, $p < 0.01$）が，グループ 2 にはマハゼ（$r^2 = 0.60$, $p < 0.01$）およびアシシロハゼ *Acanthogobius lactipes*（$r^2 = 0.27$, $p < 0.05$）が，グループ 3 にはコノシロ（$r^2 = 0.33$, $p < 0.01$），クロダイ（$r^2 = 0.31$, $p < 0.01$），エドハゼ（$r^2 = 0.66$, $p < 0.01$），スミウキゴリ（$r^2 = 0.30$, $p < 0.05$）およびミミズハゼ属複数種 *Luciogobius* spp.（$r^2 = 0.42$, $p < 0.01$）が，グループ 2 と 3 の中間方向にはスズキ *Lateolabrax japonicus*（$r^2 = 0.30$, $p < 0.05$）とビリンゴ *Gymnogobius breunigii*（$r^2 = 0.35$, $p <$

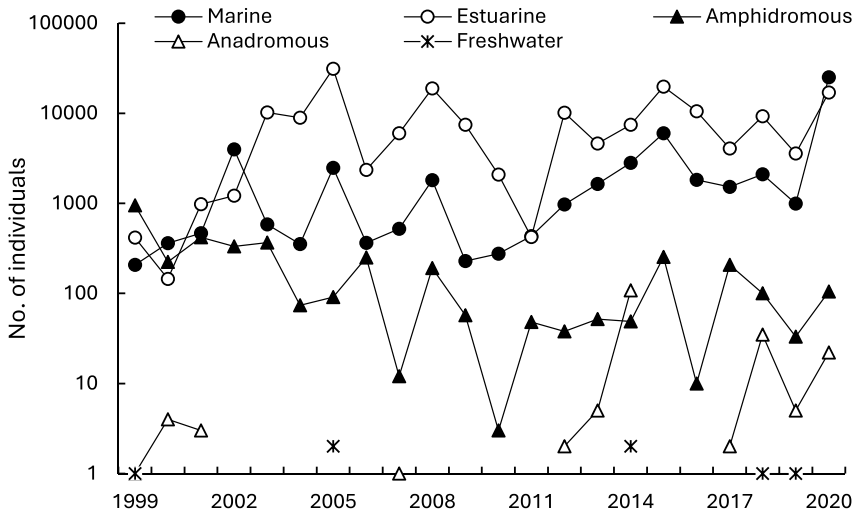

Fig. 7 Annual changes of the numbers of individuals by life-cycle categories at Kasai Marine Park in Tokyo Bay from 1999 to 2020.

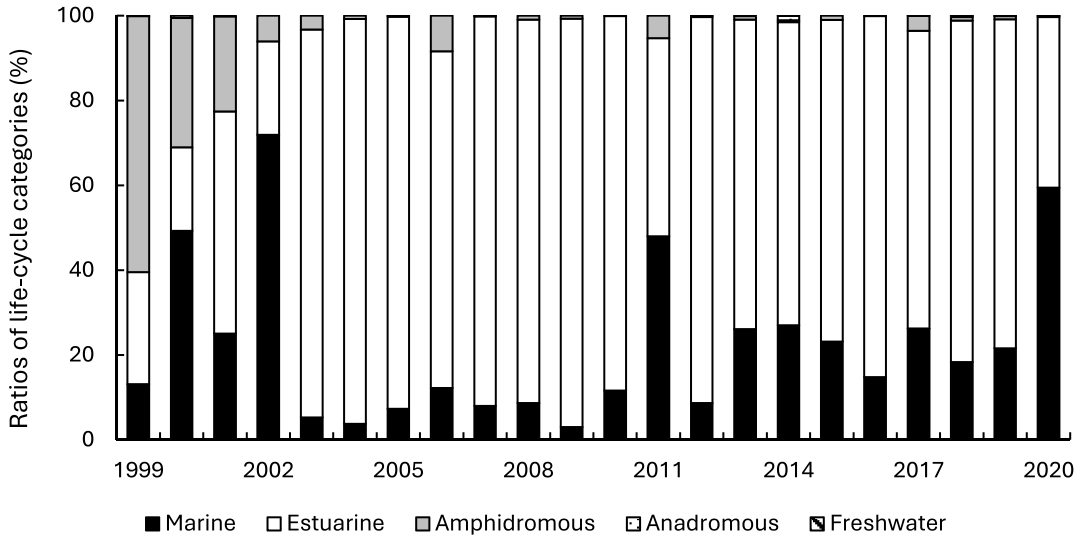

Fig. 8 Annual changes of ratio of numbers of individuals by life-cycle categories at Kasai Marine Park in Tokyo Bay from 1999 to 2020.

0.05）が表示された。pairwisePERMANOVA の結果，全てのグループ間において有意な差が確認された（グループ 1 とグループ 2：$r^2 = 0.48$, p.value< 0.01，p.adjusted < 0.05；グループ 1 とグループ 3：$r^2 = 0.32$，p.value < 0.01，p.adjusted < 0.01；グループ 2 とグループ 3：$r^2 = 0.36$, p.value< 0.01，p.adjusted < 0.01）。

Shannon-Wiener の多様度 H は，2000 年前後は 1.5～2.3 程度と高く，2000 年代半ばから後半は 1.5 以下の値が多かったが，2010 年以降は 1.5 以上になることが多くなった（Fig. 11）。最も高い多様度 H は 2000 年の 2.3，最も低い多様度 H は

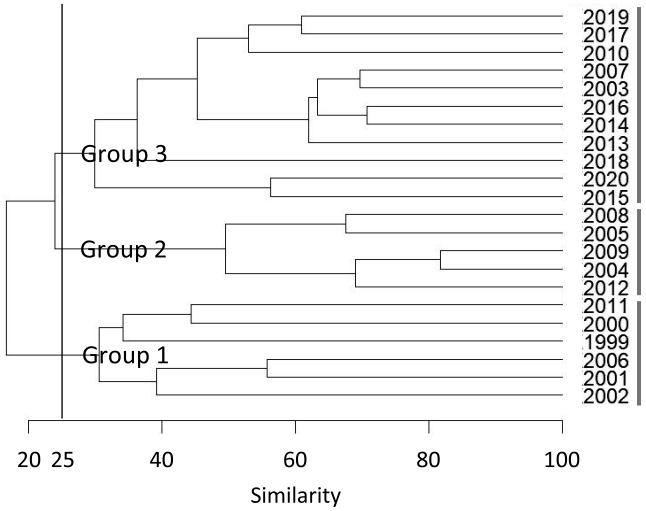

Fig. 9 Dendrogram of sampling years from the similarity index (Bray-Curtis index) based on number of individuals at Kasai Marine Park in Tokyo Bay from 1999 to 2020.

2012 年の 0.7 であり，全期間における平均値は 1.4 であった。多様度 *H*′が 2.0 を超えたのは 1 か年，1.5～2.0 の間は 8 か年，1.0～1.5 の間は 10 か年，1.0 以下は 3 か年であった。大森ふるさとの浜辺公園の干潟の多様度は，0.9～1.6 の間で変動した。多摩川河口干潟の値は，2007 年が 1.0 であったが 2013 年は 1.3 と少し上昇した。京浜島と羽田の干潟の値も 2007 年から 2013 年にかけてそれぞれ 1.7 から 2.0 へ，2.2 から 2.4 へ上昇した。新浜湖の干潟の値も 2004 年の 1.3 から 2018 年の 1.6 へあがった。

4. 6 優占した河口魚 3 種の体長組成

マハゼ *Acanthogobius flavimanus* は体長 10.0～19.9 mm の個体が多く採集され，それより少し成長した個体も比較的多かった（Fig. 12）。体長が 90.0 mm を超える大型のマハゼの割合は，1.3% であった。ビリンゴ *Gymnogobius breunigii* は体長 15.0～19.9 mm の個体が多く，その前後の体長 10.0～14.9 mm や，20.0~24.9 mm の個体も比較的多く採集された。また，体長 5.0～9.9 mm の小型個体や，40.0～44.9 mm の大型個体も採集された。エドハゼ *Gymnogobius macrognatho*s は体長 15.0～34.9 mm の個体が大きな偏りなく採集された。また，体長 5.0～9.9 mm の小型個体や，40.0～44.9 mm の大型個体も採集された。

5. 考察

5. 1 過去 22 年間の葛西海浜公園「西なぎさ」の魚類相

本調査地点の水温や DO の年変動は東京湾内湾と同様の傾向，すなわち水温は夏季に上昇，冬季に降下，DO は冬季から春季に上昇，夏季から秋季に降下する傾向を示した（例えば，東京湾岸自治体環境保全会議，2022）。塩分は 1 以下から 30 近くまで大きく変動するという特徴を示し，この傾向は 1980 年代後半の造成当時より確認されている（木村ほか，2002）。これは，主に本調査地点の東西に位置する荒川と旧江戸川の河川流入水の影響であると考えられる。本研究の底質（2021 年度の調査）は中央粒径値が 109.3～192.5 μm であったが，2000~2001 年の調査では 210 μm と報告されている（姜ほか，2002）。また，2011 年 12 月の調査では，底質の粒径別の割合は 63 μm が 0.2～14.6%，63～200 μm が 85.4～99.8% であったことから（橋本・中西，2014），本調査地点は長期

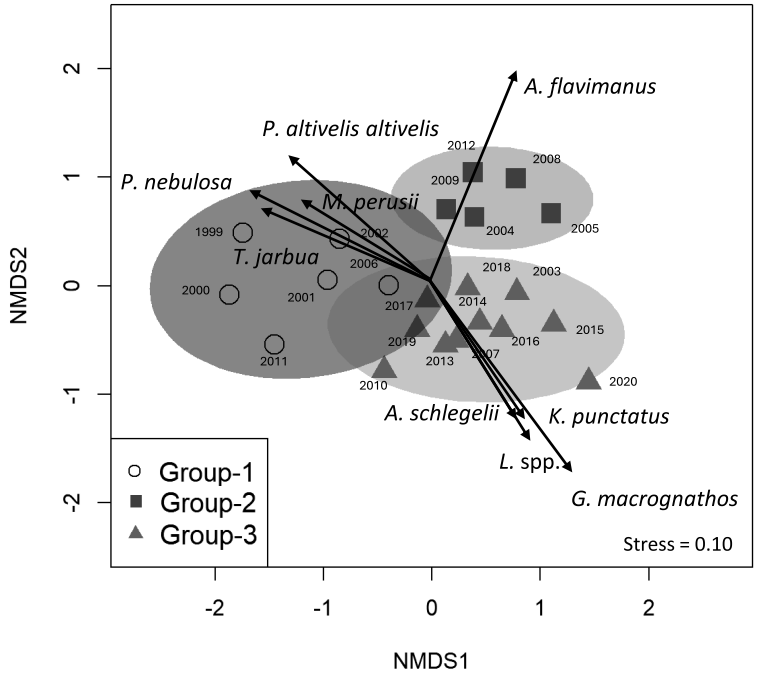

Fig. 10 NMDS（non-metric multidimensional scaling）of sampling years from the similarity index（Bray-Curtis index）based on number of individuals at Kasai Marine Park in Tokyo Bay from 1999 to 2020. The arrows indicate the direction of increase in the individuals of each species and the height of the correlation.（Stress = 0.10, *K. punctatus*: r^2 = 0.33, $p < 0.01$, *P. altivelis altivelis*: r^2 = 0.42, $p < 0.01$, *M. perusii*: r^2 = 0.27, p = 0.01, *A. schlegelii*: r^2 = 0.31, $p < 0.01$, *T. jarbua*: r^2 = 0.39, $p < 0.01$, *P. nebulosa*: r^2 = 0.46, $p < 0.01$, *A. flavimanus*: r^2 = 0.60, $p < 0.01$, *G. macrognathos*: r^2 = 0.66, $p < 0.01$, *L.* spp.: r^2 = 0.42, $p < 0.01$）

にわたって一定の砂泥質を維持していると判断できた。東京湾内湾の干潟域では，近年，魚類相の変化を促すカキ礁の発生が確認されているが（中野ほか，2023），本調査地点ではそのようなことは認められず，過去約 20 年にわたり劇的な物理環境の変化は確認できなかった。本調査地点は適時養浜や浚渫が行われていることや（東京都港湾局，2021），導流堤によって土砂の流出が抑えられていることで，ある程度安定した環境が続いていると考えられる。

本調査地点では，過去約 20 年間にわたり種数では海水魚が優占する傾向が続いていた。干潟域に出現する魚類の種数における海水魚の優占は，東京湾内でもよく確認されている（Helmosilla *et al.*, 2012；村瀬ほか，2014）。個体数に関しては，22 か年の調査のうち，17 か年で河口魚（全てハゼ科）が優占し，4 か年で海水魚が，1 か年で両側回遊魚が優占した。干潟域の仔稚魚群集におけるハゼ科魚類の優占は，東京湾に加え（加納ほか，2000；河野ほか，2008；村瀬ほか，2014），国内外の内湾や河口域で共通して確認でき（Neira *et al.*, 1992；França *et al.*, 2009；Yokoo *et al.*, 2012），そのような特徴を本調査地点も長年維持していることが明らかになった。

クラスター分析と NMDS の結果からは，魚類群集が 2000 年前後（グループ 1），2000 年代半ば

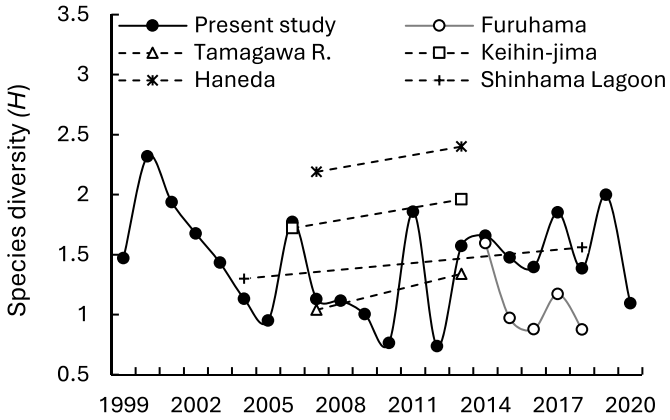

Fig. 11 Shannon-Wienner's index of species diversity *H'* for fishes collected at each sampling site in Tokyo Bay, shown by sampling years.

から後半（グループ 2）および 2010 年以降（グループ 3）の大きく 3 グループに分かれることが明らかになった。2010 年以降のグループ 3 では，コノシロ *Konosirus punctatus*，クロダイ *Acanthopagrus schlegelii* およびエドハゼ *Gymnogobius macrognathos* などと相関が高かった。このうち，コノシロやクロダイは近年東京湾で増加が指摘されている種である。コノシロは 1980 年代には，東京湾の最奥部に位置する新浜湖で成魚が集まり産卵が行われていた記録があるが，その後 2011 年ごろまではそのような大規模な産卵は認められていなかった（河野・今井，2006）。2000 年代以降，コノシロの主な産卵場は東京湾の湾口部付近とされていたが（Kong *et al.*, 2004），近年は成魚が湾奥部の沿岸域で採集されていることに加え（澤井ほか，2022），荒川河口沖などの表層域で卵や仔魚が多数見つかり，湾奥で産卵している可能性が示唆されている（Angmalisang *et al.*, 2020；丸山ほか，2024）。またクロダイについても，近年は海水温の上昇により冬季においても活発に活動でき，2010 年以降生息数を増やしているとされ，ノリの食害などが問題視されている（国土交通省国土技術政策総合研究所，2023）。エドハゼは，マハゼ *Acanthogobius flavimanus* やビリンゴ *Gymnogobius breunigii* とともに 2000 年代前半から本調査地点で優占することが確認されている（桑原ほか，2003；山根ほか，2004）。ビリンゴについては，グループ 3 によったベクトルを示したが，マハゼは 2000 年代のグループ 2 と高い相関を示した。これらのハゼ科河口魚 3 種については，生息場の重複から競合が起き，その個体数を経年的に変化させ，群集構造に影響を与えていることが予想される。今後は，この 3 種の出現様式や食性についても理解を深める必要がある。

2000 年前後のグループ 1 では，アユ *Plecoglossus altivelis altivelis* やナンヨウボラ *Moolgarda perusii* が指標種であった。アユについては 2010 年以降でも，多摩川河口周辺（村瀬ほか，2014）やお台場海浜公園（東京都環境局，2023a）などで一定量が採捕されている。また，多摩川における遡上数は，2000 年代はほぼ横ばいであったが，その後は増加傾向であることから（東京都島しょ農林水産総合センター，2023），本研究の結果は東京湾内湾の資源量の変動と必ずしも一致しない。アユは河川で孵化した後に仔魚が海域に流下するが，その後成長し遊泳力を獲得すると，上げ潮に乗って干潟に来遊することが知られている（東，2005；Kanou *et al.*, 2005；丸山・河野，2020）。本研究では潮汐を考慮せずに採集を行っているため，アユについては潮汐に合わせたサンプリング

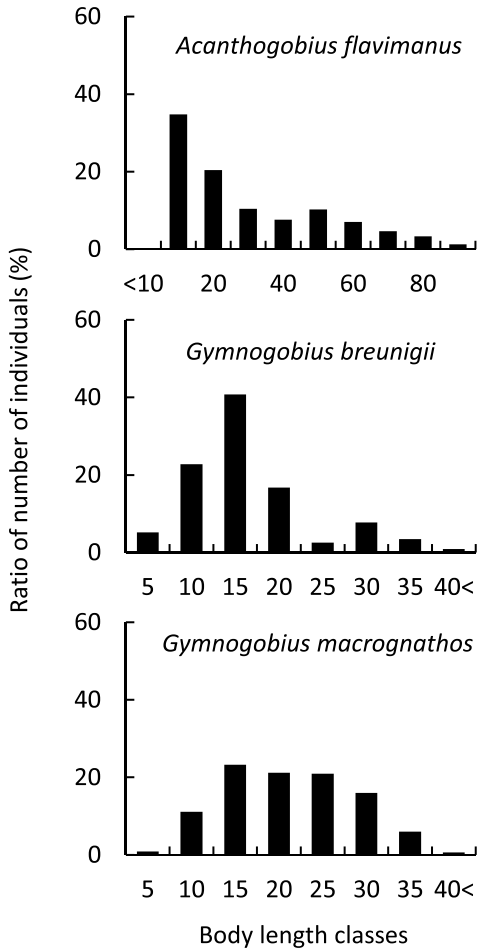

Fig. 12 Body length classes of 3 dominant estuarine species (*A. flavimanus*, *G. breunigii*, *G. macrognathos*) at Kasai Marine Park in Tokyo Bay from 1999 to 2020.

を行うことで，人工干潟の重要度を詳細に明らかにできると考えている。ナンヨウボラは東京都の調査によると，1988～2001 年まではほぼ毎年確認されていたが（東京都環境局，2023a），その後全く確認されなくなった魚種である。このことについては 2006 年に京浜島で調査を行った茂木ほか (2009) も「メナダとナンヨウボラは，逆に近年になって記録がほとんどなくなった種で，本研究でも採集されなかった」と触れている。採集されなくなった理由は定かではないが，ナンヨウボラの成魚は南方種（中坊，2013）であることから，東京湾に定住している可能性は低い。

多様度の経年変化は，近年にかけて若干の上昇傾向を示した。比較を行った東京湾内湾の他の干潟でも，2000 年代から 2010 年代にかけて多様度の上昇が認められた。多様度の上昇については様々な要因が複合的に関係していると考えられるが，例えば東京湾内湾の COD（Chemical Oxygen Demand: 化学的酸素要求量）の値は 1999 年から 2020 年にかけて横ばいの傾向が続いており（河野，2022），水質の改善が多様度の上昇に直接影響している可能性は低いと判断できる。澤井ほか (2022) は，東京湾内湾に位置する人工潟湖（新浜湖）において，1970 年代と 2010 年代で小型定置網を用いて採集された魚種の比較を行い，近年では様々な暖海域の魚類が東京湾内湾に出現し，その影響が干潟域にも出ていると報告している。この報告では東京湾内の水温上昇によって出現する魚種が変化していると結論付けられており，例えば本研究でも 2014 年以降は連続的に暖海性のトラフグ *Takifugu rubripes* が採集されている。このように出現する魚類の増加は，少なからず多様度に影響を与えている可能性がある。

また，本調査地点の多様度は，人工干潟である大森ふるさとの浜辺公園の干潟や新浜湖の干潟と同等かそれ以上の値であった。上記の 2 つの干潟は，運河域の奥や潟湖内に位置しており，閉鎖的な干潟である。本調査地点は東京湾に向かい開放的な立地をしていることから，様々な魚類が自由に来遊することができ，多様度が高くなった可能性がある。記録された種数については，調査期間の長さによる累積があるものの，本研究が 35 科 58 属 70 種以上であったことに対し，大森ふるさとの浜辺公園では 2014 年から 2019 年の 5 年間で 19 科 31 属 40 種類（丸山ほか，2021），新浜湖では 3 か年（1999 年 4 月から 2000 年 3 月，2004 年 4 月から 2005 年 3 月，2018 年 4 月から 2019 年 3 月）で 20 科 34 属 48 種類以上（加納ほか，2000；河野ほか，2008；中野ほか，2023），羽田，京浜島および多摩川河口の 3 地点では，2007 年～2012 年の 5 年間で合わせて 29 科 46 属 56 種（村瀬ほ

か，2014）である。

5. 2 優占するハゼ科魚類

本調査地点では約 20 年間，ハゼ科の河口魚が優占して出現していた。ハゼ科河口魚は 13 種が出現したが，その中でもマハゼ *Acanthogobius flavimanus*，ビリンゴ *Gymnogobius breunigii* およびエドハゼ *Gymnogobius macrognathos* の個体数は多く，これら 3 種で河口魚の総個体数のうち 96.5% を占めた。また，これらの 3 種は仔魚～成魚が本研究で出現していることから，生活史を通して本調査地点を利用していることが明らかになった。干潟域においてマハゼやビリンゴが優占して出現し，生活史を通して利用している事例は，1990 年代から現在まで，多摩川河口周辺の自然干潟や人工干潟，お台場海浜公園，荒川河口干潟，小櫃川河口干潟など様々な干潟で確認されており（加納ほか，2000；Hermosilla *et al.*, 2012；村瀬ほか, 2014；村井ほか, 2016；東京都環境局, 2023a），東京湾内湾の干潟がもつ魚類群集の特徴である。一方で，エドハゼが最も優占して出現する例は近年では珍しく，1990 年代後半から 2000 年代前半に，多摩川河口干潟や千葉県市川市に位置する人工潟湖（新浜湖）内の干潟で確認された程度であり（加納ほか，2000；河野ほか，2008），そのうち新浜湖では 2018 年から 2019 年の調査では採集個体数が激減している。エドハゼは，河口付近の砂泥質の干潟域を生息場として選択するが（河野，2011），河川の開発や干潟の埋め立ての影響を受け，環境省のレッドリストでは絶滅危惧 II 類（VU）に，東京都レッドデータブックでは準絶滅危惧（NT）に分類されている（環境省自然環境局，2020；東京都環境局，2023b）。産卵場は干潟に生息するニホンスナモグリ *Neotrypaea japonica* などの十脚類の巣穴であることから（Henmi *et al.*, 2018），そのような十脚類とエドハゼの両種が生息できるような良好な干潟を保護・保全することが重要視される。実際にエドハゼが産卵に用いた十脚類の巣穴の底質は，粒径< 62.5 μm 以下の割合は 7.19%，中央粒径値は 211 μm であった（Koyama *et al.*, 2017；Henmi *et al.*, 2018）。本調査地点の底質は，粒径 74 μm 以下の割合は 2.0～29.0%，中央粒径値は 109.3～192.5 μm であり，実際に産卵場として選択される底質環境に比較的近い。したがって，本調査地点の砂泥質環境は，エドハゼの成育や産卵に好適である可能性が高く，生息場のみならず，産卵場を提供できている可能性が高い。マハゼやビリンゴに加え，エドハゼに好適な産卵・成育場を長期にわたり提供できていることは本調査地点の特徴であり，人工干潟の可能性を示す一例として評価することができると考えられる。

謝辞

本研究の遂行にあたり，2008 年までの調査結果をまとめ，当時の調査方法について情報提供をいただいた池田正人氏をはじめ，長年調査に携わってきた葛西臨海水族園の地曳網調査歴代担当者の皆様に，感謝いたします。

引用文献

Angmalisang, D. E., H. Imai and H. Kohno (2020): Habitat shifts of larval and juvenile Konoshiro gizzard shad, *Konosirus punctatus*, in relation to the functional development in Tokyo Bay, central Japan. Journal of the Tokyo University of Marine Science and Technology, **16**, 39–52.

東健作（2005）: アユの海洋生活期における分布生態. 高知大学海洋生物教育研究センター研究報告, **23**, 59–112.

Dufrene, M. and P. Legendre (1997): Species assemblages and indicator species: the need for a flexible asymmetrical approach. Ecological Monographs, **67**, 345–366.

França, S., M. J. Costa and H. N. Cabral (2009): Assessing habitat specific fish assemblages in estuaries along the Portuguese coast. Estuarine, Coastal and Shelf Science, **83**, 1–12.

橋本慎治，中西悠（2014）: 葛西海浜公園西なぎさにおけるカワゴカイ属およびイトゴカイ科の分布と底質との関係. 帝京科学大学紀要, **10**, 153–158.

Henmi, Y., K. Eguchi, R. Inui, J. Nakajima, N. Onikura and G. Itani (2018): Field survey and resin casting of *Gymnogobius macrognathos* spawn-

ing nests in the Tatara River, Fukuoka Prefecture, Japan. Ichthyol. Res., **65**, 168–171.

Hermosilla, J.J., Y. Tamura, M. Moteki and H. Kohno (2012): Distribution and community structure of fish in Obitsu-gawa River Estuary of inner Tokyo Bay, central Japan. AACL Bioflux, **5** (4), 197–222.

鎌谷明善 (1993): 海岸線の変貌．東京湾－ 100 年の環境変遷（小倉紀雄編），恒星社厚生閣，東京，p. 20–27.

姜閏求，高橋重雄，黒田豊和，奥平敦彦 (2002): 前浜干潟の地形・地盤の特徴と干潟のタイプ分け－人工干潟の耐波安定性に関する研究－，海洋開発論集，**18**，13–18.

環境庁自然保護局 (1997): 日本の干潟，藻場，サンゴ礁の現状．海中公園センター，東京，291 pp.

環境省自然環境局 (2020): 環境省レッドリスト 2020 の公表について．URL: https://www.env.go.jp/press/107905.html (2025–1–20 参照)

加納光樹，小池哲，河野博 (2000): 東京湾内湾の干潟域の魚類相と多様性．魚類学雑誌，**47**，115–129.

Kanou, K., M. Sano and H. Kohno (2005): Larval and juvenile fishes occurring with flood tides on an intertidal mudflat in the Tama River estuary, central Japan. Ichthyol. Res., **52**, 158–164.

木元新作 (1993): 集団生物学概説．共立出版，東京，188 pp.

木村賢史，西村修，太田祐司，三嶋義人，柴田規夫，稲森悠平，須藤隆一 (2002): 人工海浜造成後の魚類，鳥類，水辺植生の遷移に関する研究．土木学会論文，**720**，15–25.

国土交通省港湾局・環境省自然環境局 (2004): 干潟ネットワークの再生に向けて．国立印刷局，119 pp.

国土交通省国土技術政策総合研究所 (2023): 第 22 回東京湾シンポジウム報告書．URL: https://www.ysk.nilim.go.jp/kakubu/engan/kaiyou/kenkyu/tokyo230413/01.tokyo22th_report.pdf (2024–1–20 参照)

Kong, L., M. Kawasaki, K. Kuroda, H. Kohno and K. Fujita (2004): Spawning characteristics of the konoshiro gizzard shad in Tokyo and Sagami Bays, central Japan. Fish. Sci., **70**, 116–122.

河野博 (2011): 東京湾の魚類．平凡社，東京，374 pp.

河野博 (2022): 江戸前の海の物語．原書房，東京，288 pp.

河野博，今井仁 (2006): 第 4 章 東京湾の魚のおもしろ生活史 1 江戸前ずしの代表．東京湾魚の自然誌（河野博監修），平凡社，東京，132–140.

河野博，横尾俊博，茂木正人，加納光樹 (2008): 東京湾岸に位置する人工潟湖（新浜湖）の魚類相．日本生物地理学会会報，**63**，133–142.

Koyama A., R. Inui, K. Umemura, M. Wakabayashi, K. Kanno and Norio Onikura (2017): The first record of the spawning nest of *Gymnogobius cylindricus* and *Gymnogobius macrognathos*. Ichthyol. Res., **64**, 261–263.

桑原悠字，土田奈々，元山崇，河野博，加納光樹，島田裕至，三森亮介 (2003): 葛西人工渚（東京湾湾奥部）の魚類相．La mer，**41**，28–36.

丸山啓太，河野博 (2020): 東京湾奥部の運河域に造成された人工海浜（大森ふるさとの浜辺公園）におけるアユ仔稚魚の出現．La mer，**58**，51–57.

丸山啓太，河野 博，竹山佳奈，中瀬浩太 (2021): 東京湾内湾に造成された砂浜海岸と泥質干潟の魚類相と多様性．東京海洋大学研究報告，**17**，1–17.

丸山啓太，森竜也，中島俊平，片野俊也，河野 博 (2024): 東京湾内湾の表層域における仔稚魚相－コノシロとカタクチイワシの産卵の可能性－．東京海洋大学研究報告，**20**，27–36.

茂木正人，安田健吾，山本佳子，横尾俊博，河野博，諸星一信，鈴木信昭，松坂省一，有路隆一 (2009): 東京湾京浜島の魚類相の季節変化と長期モニタリングの必要性．La mer，**46**，123–134.

村井俊太，村瀬敦宣，河野博，竹山佳奈，中瀬浩太，岩上貴弘 (2016): 東京湾の湾奥に再生された干潟と人工海浜 (大森ふるさとの浜辺公園) の魚類相．La mer，**54**，11–27.

村瀬敦宣，角張ちひろ，加瀬喜弘，齊藤有希，河野博 (2014): 羽田空港滑走路の建設は多摩川河口干潟域を利用する魚類にどのように影響するか？ 日本生物地理学会会報，**69**，57–75.

中坊徹次 (1993): 日本産魚類検索 全種の同定．東海大学出版会，神奈川県秦野市.

中坊徹次 (2000): 日本産魚類検索 全種の同定 第二版．東海大学出版会，神奈川県秦野市.

中坊徹次 (2013): 日本産魚類検索 全種の同定 第三版．東海大学出版会，神奈川県秦野市.

中野航平，丸山啓太，澤井伶，風呂田利夫，野長瀬雅樹，河野 博 (2023): 東京湾内湾に位置する人工

潟湖（新浜湖）の仔稚魚相とその変遷．東京海洋大学研究報告，**19**，1–14.

中瀬浩太（2008）: 人工干潟の施工およびモニタリング．建設の施工企画，**8**，42–47.

那須賢二，甲原道子，渋川浩一，河野博（1996）: 東京湾湾奥部京浜島の干潟に出現する魚類．東京水産大学研究報告，**82**，125–133.

Neira, E. J., I. C. Potter and J. S. Bradley（1992）: Seasonal and spatial changes in the larval fish fauna with in a large temperate Australian estuary. Marine Biology, 112, 1–16.

岡加奈子（2021）: 東京都初のラムサール条約湿地 葛西海浜公園．湿地研究 Wetland Research，**11**，89–92.

沖山宗雄（1988）: 日本産稚魚図鑑．東海大学出版会，神奈川県秦野市.

沖山宗雄（2014）: 日本産稚魚図鑑 第二版．東海大学出版会，神奈川県秦野市.

大垣俊一（1999）: 群集組成の多変量解析．Argonauta，**1**，15–26.

大森健策，加納光樹，碓井星二，増子勝男，篠原現人，都築隆禎，横井謙一（2018）: 過去 50 年間の北浦における魚類相の変遷．魚類学雑誌，**65**（2），165–179.

R Development Core Team（2025）: R: A language and environment for statistical computing. R Foundation for Statistical Computing, Vienna, Austria. URL: http://www.R-project.org

澤井伶，中野航平，丸山啓太，河野博，風呂田利夫，野長瀬雅樹（2022）: 東京湾内湾に位置する人工潟湖（新浜湖）の魚類相の長期的変遷．神奈川自然誌資料，**43**，25–37.

清水誠（1990）: 東京湾の魚介類（6）昭和 60 年代の生物相．海洋と生物 68 号，株式会社生物研究社，東京，p. 183–189.

穴戸太郎，青木茂，金子誠也，佐野光彦（2019）: 東京湾内湾に造成された人工砂浜海岸における魚類群集の構造．La mer，**57**，1–23.

東京都環境局（2023a）: 令和 3 年度水生生物調査結果報告書（東京都内湾）．東京都環境局自然環境部水環境課，東京，174 pp.

東京都環境局（2023b）: 7．淡水魚編．東京都レッドデータブック（本土部）（東京都環境局自然環境部編），株式会社恒和プロダクト，東京，p. 527–549.

東京都港湾局（2021）: 葛西海浜公園保全活用計画本文．URL: https://www.kouwan.metro.tokyo.lg.jp/kanko/kasaikaihinkouen_sakutei_honbun.pdf（2025–1–20 参照）

東京都島しょ農林水産総合センター（2023）: 推定 208 万尾のアユが多摩川を遡上～昨年同様 200 万尾超～．URL: https://www.ifarc.metro.tokyo.lg.jp/topics/uploads/9f87074f2ded7917358df271b124eaa7_1.pdf（2025–1–20 参照）

東京湾岸自治体環境保全会議（2022）: 東京湾水質調査報告書（令和 2 年度）．URL: http://www.tokyowangan.jp/database/pdf/r02hokoku_v2.pdfl（2025–1–20 参照）

梅田新也，河野 博（2017）: 新滑走路の建設によって京浜島の魚類相は変化しているのか？ − 2014 年京浜島でのサンプリングから −．東京海洋大学研究報告，**13**，36–44.

山根武士，岸田宗範，原口泉，阿部礼，大藤三矢子，河野博，加納光樹（2004）: 東京湾内湾 2 地点（葛西臨海公園と八景島海の公園）の仔稚魚相．La mer，**42**，35–42.

Yokoo T., K. Kanou, M. Moteki, H. Kohno, P. Tongnunui and H. Kurokura（2012）: Assemblage structures and spatial distributions of small gobioid fishes in a mangrove estuary, southern Thailand. Fish Sci., 78. 237–247.

Received: February 15, 2025
Accepted: August 12, 2025